SAFER AND MORE EFFICIENT REACTOR DESIGN AND OPERATION FOR N-

OXIDATION OF ALKYLPYRIDINES – FROM A PERSPECTIVE OF REACTOR

MODELING AND SYSTEM ANALYSIS

A Dissertation

by

XIAOHONG CUI

Submitted to the Office of Graduate and Professional Studies of
Texas A&M University
in partial fulfillment of the requirements for the degree of

DOCTOR OF PHILOSOPHY

Chair of Committee,	Benjamin A. Wilhite
Co-Chair of Committee,	M. Sam Mannan
Committee Members,	Mahmoud El-Halwagi
	Andrea Strzelec
Head of Department,	M. Nazmul Karim

December 2017

Major Subject: Chemical Engineering

ABSTRACT

This work aims to promote continuous manufacturing of fine chemicals and pharmaceuticals by proper reactor design and operation. These synthetically important yet potentially hazardous chemistries are conventionally carried out in batch/semi-batch mode, which is subject to challenges including cumbersome scale-up (*e.g.*, mixing and heat transfer limitation), safety concerns (large reaction volume and chemical inventories), and product quality variation from batch to batch. Continuous processing could potentially address these issues by (i) reducing reactor volume without compromising overall throughput, (ii) enhancing mixing and heat transfer, and (iii) enabling better product quality control via steady-state operation.

For illustration, two continuous reactor configurations for a model chemistry, i.e. N-oxidation of alkylpyridines, whose products are key intermediates for drug syntheses and agricultural compounds, are studied based upon kinetics and reactive hazards information obtained from calorimetry studies in order to perform the chemistry in a more scalable and inherently safer fashion.

The first reactor studied is a conventional stirred-tank reactor which could facilitate control and instrumentation owing to ideally homogeneous distribution and lower capital costs for changeover from batch to continuous. Classical reaction engineering/system fundamentals (*e.g.*, first-principles reactor modeling, system dynamics and stability) are applied to analyze reactor steady-state multiplicity and oscillation phenomena that may bring about serious incidents. Reactor design and

operation conditions as well as start-up strategies and worst-case scenarios are systematically investigated to address process safety concerns and balance reactor efficiency.

The second reactor analyzed is a novel tube-in-tube membrane reactor, which facilitates controlled radial slip of hydrogen peroxide into co-current alkylpyridine flow driven by an applied trans-membrane pressure difference across the inner porous ceramic tube. Design rules in terms of relative permeation and reaction rates are established in terms of desired outlet alkylpyridine conversion and peroxide residue using a single isothermal tube-in-tube unit. Multi-unit module design is then investigated to optimize productivity and module dimensions while balancing heat transfer capability to maintain isothermal operation in practice and preventing mass transfer across the unit boundary to ensure isolation.

DEDICATION

To my family

ACKNOWLEDGEMENTS

CONTRIBUTORS AND FUNDING SOURCES

TABLE OF CONTENTS

LIST OF FIGURES

LIST OF TABLES

CHAPTER I

INTRODUCTION

Pharmaceuticals are playing an increasingly critical role in the healthcare system due to drug coverage expansion and preventive care promotion as well as aging population/lengthening life expectancies.[1,2] As such, the pharmaceutical industry must confront the challenge of ensuring availability of safe, effective, and affordable medicines, including both conventional blockbuster drugs and innovative and/or genetically-tailored therapies with smaller intended patient populations and lower peak demand that field unmet medical needs of patients with serious diseases. When combined with other factors such as costs for R&D and production, price controls, and patent challenges,[3] this not only requires consistent compliance with regulations enforced by the U.S. Food and Drug Administration (FDA) for assuring safety and efficacy of drug products, but also necessitates employment of state-of-the-art technologies and innovative approaches along with risk management methodology throughout the life cycle of products.

Actually, in 2002, FDA launched an initiative entitled "Pharmaceutical CGMPs for the 21st Century: A Risk-Based Approach"[4] to overcome tepidity for innovating manufacturing practices traditionally prevailing in the pharmaceutical industry. This initiative underscores an integrated systems approach that relies on scientific and engineering principles, and depicts desired characteristics of pharmaceutical manufacturing, including built-in product quality via appropriate process design and

fundamental understanding of the dependence of product quality on formulation and process factors, continuous real-time process monitoring, regulatory policies in accordance with the latest scientific knowledge, and risk-based regulatory approaches recognizing risk reduction capability. To concrete the tenets of the initiative, FDA, together with other agencies such as the Center for Biologics Evaluation and Research (CBER) and the Office of Regulatory Affairs (ORA), subsequently developed and introduced the Process Analytical Technology (PAT)[5] in 2004. Specifically, PAT details recommendations for tools and principles (chemical, physical, microbiological, mathematical, and risk analysis) in order to ensure final product quality via integrated design, analysis, and control of manufacturing processes, where process understanding throughout the life cycle of a product, which identifies and explains the multi-factorial relationships between potential variability (*e.g.*, materials, process parameters, environmental factors, and supply chain, etc.) and drug attributes (chemical, physical, and biopharmaceutical), plays a fundamental and key role. To facilitate such understanding for raw and in-process materials, PAT outlines suggested tools which would stimulate and enable innovation of pharmaceutical development, manufacturing, and quality assurance via, for instance, reducing production cycle times, strengthening automation to improve safety and reduce human errors, and *facilitating continuous processing to improve efficiency and manage variability*.

1.1 Flow Chemistry and Continuous Processing

1.1.1. General description and advantages

Pharmaceutical manufacturing remains one of the last industry sectors dominated by time-consuming batch-wise processing. Starting from raw materials obtained from different suppliers, the complex synthetic route (Figure 1.1) typically consists of multiple unit operations for reaction, workup, and isolation, which conventionally take place in a small number of large vessels for assembling active pharmaceutical ingredients (APIs), followed by sequences to formulate final drug products from the APIs. Specifically, among the workup and isolation operations, crystallization or precipitation (reactive crystallization) is the major step for obtaining pure target molecules in solid state via control of temperature, supersaturation, nucleation, and crystal growth, while other steps such as distillation, extraction, adsorption, and filtration are employed for preparing the solution for crystallization.

The resulting long production duration and large amounts of intermediate inventories, which can be hazardous, along with other limitations of batch processing (*e.g.*, quality variations and supplier changes) have driven notable interests among the organic synthesis community in steering discovery, screening, and manufacturing of pharmaceuticals towards a flow chemistry and continuous processing manner over the last decade. Table 1.1 summarizes the most declared merits of streamlining and integrating pharmaceutical production,[6-14] which essentially echo the goal of PAT and hence perfectly exemplify application of the aforementioned tools and principles the PAT framework proposes.

3
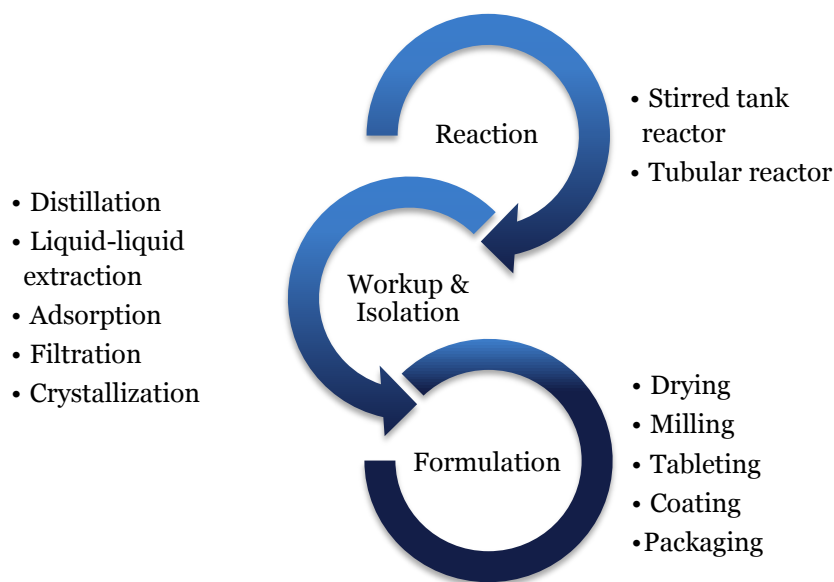
Figure 1.1. Typical sequences and unit operations for API syntheses and final drug formulation.

Notwithstanding these benefits, which are process specific in practice, widespread adoption of continuous processes has not prevailed in the pharmaceutical industry with challenges primarily stemming from complexity and diversity of the molecules as well as their processing conditions and steps. While some of the steps in Figure 1.1 are inherently continuous or routinely operated in continuous mode, for example, distillation, (spray) drying, tableting, and packaging, pressing needs are yet to be addressed for running other steps in flow and for robust integration of these steps in a single end-to-end process.[9,15,16]

Table 1.1. Merits of switching to continuous processing for pharmaceuticals

Merits	Interpretation
Safety	• Downsized reactor volume • Minimized inventories of hazardous materials • Enabled steady-state operation • Alleviated operation risks
Quality	• Ensured consistency owing to reproducible operation conditions • Reduced impurities
Process development	• Automated Design of Experiments (DOEs) • Accelerated campaign, prototyping, and technology transfer
Process intensification	• Enhanced mass and heat transfer • Extended reaction conditions (*e.g.*, elevated temperature and/or pressure) • Improved yield and selectivity
Economics	• Added capacity • Deferred capital and operation costs • Promoted manufacturing flexibility
Green chemistry	• Lessened waste generation • Decreased solvent consumption

Broadly speaking, pharmaceutical development pipeline is phased into three stages, namely molecule discovery, clinical trial, and manufacturing, where different approaches are usually adopted to perform the chemistry (i.e. the reaction step shown in Figure 1.1). In the early stage, it is desired to obtain a myriad of compounds as quickly as possible and therefore costs and/or use of hazardous materials are not often considered. In addition, engineering and optimization of processes are deemed trivial

since only very small quantities of each compound are needed. Contrarily, as development progresses, issues including safety, ease of separation, scaling difficulty, and reagents costs must be taken account of, which may be likely to result in a new synthetic route compared to the one employed in the discovery stage. In this regard, Baxendale et al.[9] estimate that it would be beneficial to switch to flow for approximately 40% of the overall reaction classes which are originally batch-derived. The authors further point out that this figure would readily rise if continuous processing comes into play earlier or, in other words, flow is more inherently built into the life cycle of new compounds, which is actually gaining popularity owing to wide availability of stand-alone components (for flow delivery, reaction, mixing, quenching, and real-time analyzing/monitoring/control, etc.) of in-house assembled platforms[6,17,18] (see Figure 1.2) that would greatly facilitate several-order-of-magnitude scale-up via applying classical reaction engineering principles.

1.1.2. Reactions and reactors

Primary reaction classifications apt to render remarkable benefits via running in flow are reactions with intrinsic safety concerns (*e.g.*, high thermal risks, explosive or toxic reagents) and/or fast kinetics.[9,15] Continuous reactors that are most commonly adopted so far in various academic and industrial applications for housing these reactions include microreactors, continuous stirred tank reactors (CSTR), and tubular reactors, as presented in Table 1.2. Selection among these reactors is project specific, which requires in-depth understanding of associated hazards, physical states, kinetics, transport, and the last but not the least, development objectives.[11,14,15]

6
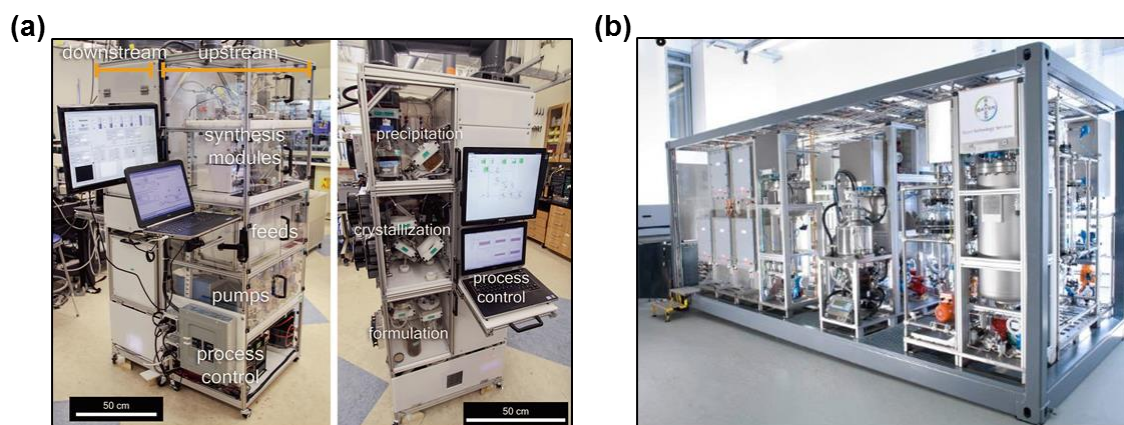
Figure 1.2. Self-assembled platforms for continuous innovative chemistry discovery and manufacturing process development (a) Multistep synthesis, purification, workup, and formation platform with a size of 1.0 m (W) × 0.7 m (L) × 1.8 m (H) for producing diphenhydramine hydrochloride, lidocaine hydrochloride, diazepam, and fluoxetine hydrochloride. Reprinted with permission from The American Association for the Advancement of Science (Adamo et al.[6]) (b) Portable mini factory. Reprinted with permission from Beilstein Journal of Organic Chemistry (Baumann and Baxendale[17])

Microreactors have been predominantly leveraged for rapid screening and optimization of synthetic routes and revealing reaction mechanisms and kinetics.[19-28] Owing to the small scale of the systems and therefore the small quantities of materials present, microreactors offer tremendous heat/mass transport and risk mitigation capabilities. Challenges to be overcome for evolution of microchemical technologies and consequently for promoting their application in continuous pharmaceutical processing include effective clogging mitigation[29,30] and well-engineered process integration of microreactors with other unit operations as well as reliable scale-up strategies.

Table 1.2. Typical continuous reactors exploited in literature for enabling flow chemistry and continuous syntheses

	Microreactor	CSTR	Tubular reactor
Materials of construction	• Silicon • Stainless steel • Ceramic • Polymer	• Stainless steel • Glass	• Metal: *e.g.*, stainless steel, copper, hastelloy • Polymer: *e.g.*, PTFE, PFA, PEEK
Major advantages	• Permit high temperature and pressure • Minimize presence of hazardous materials	• Handle solids in flow • Handle immiscible liquid phases	Enhance gas-liquid / gas-liquid-solid mass transport
Major limitations	Scale-up	Selectivity	Clogging and plugging due to solid formation
Configurations	• Packed-bed • Capillary • Spiral	• CSTRs in series • Intermittent-flow (Cole et al.[33]; Tsukanov et al.[34]; White et al.[35])	• PFRs (piped or coiled) in series • Packed-bed • Tube-in-tube • Segmented flow
Application examples	• Kinetics (Moore et al.[25]; Zaborenko et al.[27]) • Screening and optimization (McMullen et al.[31]) • Scale-up (Zhang et al.[32])	• Grignard reaction (Wong et al.[36]) • Cyclization (White et al.[35]) • Suzuki coupling (Cole et al.[33])	• Hydrogenation (Johnson et al.[37]; Zaborenko et al.[38]) • Cyclization (May et al.[39]) • Hydroformylation (Abrams et al.[40]; Johnson et al.[41]) • Amination (Johnson et al.[42])

While the novel microchemical technologies have received extensive research in academia over the past decade, larger and/or more conventional reactor paradigms such as CSTRs[33-36,43] and PFRs[37-42] are still popular within the pharmaceutical industry for campaigns to promote the continuous processing concept whose ultimate objective is to streamline production-scale processes. And, as a matter of fact, publications from pharmaceutical companies have shed much light on how the "simplest" of reactors could evoke wonder. For instance, Wong et al.[36] explored the CSTR operation strategy in terms of magnesium (Mg) recharge frequency, geometry and positioning of settling pipe for Mg sequestration, and reaction monitoring of temperature for a Grignard reaction step within the commercial route for Edivoxetine·HCl that involves Mg activation and high reaction exotherm. The strategy was proposed via CFD modeling and was verified through lab-scale tests at two scales (2 and 30 L CSTRs), which effectively lent references for commercial site operation. A pilot-scale Hastelloy trickle-bed reactor with a total volume of 3.21 L was developed by Zaborenko et al.[38] for hydrogenolysis of a C-N and an N-O bond, and was successfully demonstrated across three process scales (substrate throughputs 9 − 550 g/h and catalyst loading 20 − 1500 g) for minimizing hydrogen presence in the system, improving impurity control and catalyst (5% Pd/C, type S4366) utilization, and reducing reactor size compared to batch counterpart of same throughput. Johnson et al.[37] developed a pilot-scale full continuous process for an intermediate synthesis, which highlighted a high pressure (70 bar H_2) coiled stainless steel PFR of 73 L for housing the rhodium-catalyzed asymmetric hydrogenation of ketone as well as workup and isolation steps including liquid-liquid extraction and

9

crystallization. The process was demonstrated to be capable of delivering the same weekly throughout as traditional batch processing while the resulting reaction volume was four-fold less than the batch one.

In addition to the conventional operation modes, some engineering could be also "tweaked" to the processes so as to readily cater to the needs of specific chemistry. For instance, Tuscanov et al.[34] proposed and implemented a 250 mL automated intermittent-flow CSTR with catalyst recycle to accommodate a stereoselective aza-Henry reaction in order to achieve controlled addition of the highly energetic arylnitromethane compound, which would otherwise be realized by introducing multiple injection points along axial length if PFR were employed. Besides the additional time and capital costs required, the PFR scheme was vetoed due to the superiority of CSTR over PFR in handling heterogeneous reactions with solids. Abrams et al.[40] demonstrated favorable benefits of a vertical pipes-in-series PFR for asymmetric hydroformylation of 2-vinyl-6-methoxynaphthalene catalyzed by Rh(BDP), a high pressure reaction involving flammable H_2 and CO reagents. Enhanced gas-liquid mass transport and improved selectivity were achieved on the research-scale setup where the vertical pipes operating in bubble flow regime have a dimension of 8 mm (ID) and 7.3 mm (H) while the connecting tubes, operating in segmented flow regime, a dimension of 0.56 mm (ID) and 3.7 m (L). A commercial-scale of the design, which has a total volume of 380 L with a pipe length of more than 6 m and a diameter of more than 5 cm, could be found elsewhere.[17]

1.2   Chemical Reactivity and Reactor Safety

As suggested by those examples in the previous section, one of the compelling reasons for switching to flow is safety advantages compared to batch processing. Indeed, numerous synthetic reactions in the pharmaceutical industry pose serious reactive hazards. For instance, reactions such as Grignard, alkylation, and free-radical are fast and highly exothermic. And multiphase reactions like nitration and direct fluorination are subject to local heat accumulation and hot spot formation. Moreover, versatile but highly energetic and/or toxic reagents are extensively used, including azides, diazonium intermediates, nitroalkanes, epoxides, hydrogen, and ozone, just to name a few. Therefore it is crucial to promote sufficient awareness and enforce effective management of these hazards throughout the entire life cycle of a drug product, which is also recommended by the U.S. Chemical Safety and Hazard Investigation Board (CSB) based upon its analysis and report[44] of 167 serious accidents in U.S. involving reactive chemicals.

1.2.1. Identification of reactive hazards

1.2.1.1.   Preliminary screening

Crowl and Louvar[45] provide a flowchart (Figure 1.3) for preliminary screening of reactive hazards prior to detailed characterization. Since multiple unit operations such as mixing, drying, distillation, and adsorption, etc. are typically present in the synthetic route for an API or drug product, it is important to examine the effect of potential reaction and/or heat generation taking place during each of these operations which may be unintended by design. The authors also detail lists of violent reaction classifications

and highly reactive functional groups which are indicative of specific reaction hazards. Other useful resources that could be referred to for preliminary screening include Material Safety Data Sheet (MSDS), Chemical Thermodynamics and Energy Release Evaluation (CHETAH), and Chemical Reactivity Worksheet (CRW). CHETAH is a handy computer program capable of predicting reactive hazards of pure chemicals, mixtures, and reactions in addition to their thermochemical properties with merely molecular structure required as input, while CRW is primarily used to provide chemical compatibility information of dual chemicals of interest.
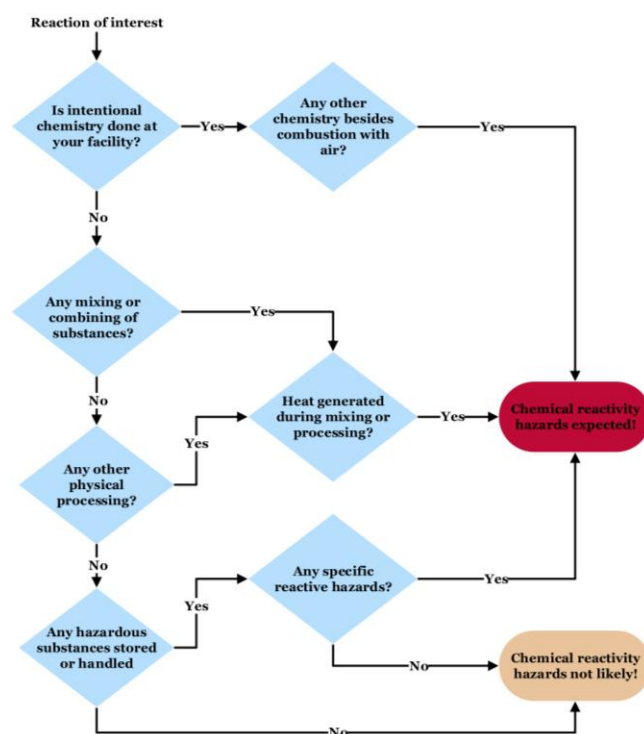
Figure 1.3. Flowchart for preliminary screening of reactive hazards[45]

Table 1.3. Typical calorimeters used in the pharmaceutical and other industries (adapted from Crowl and Louvar[45])

	Type	Typical volume of test vessel	Nominal ϕ factor	Comments
DSC	• Open to atmosphere • Adiabatic	< 1 mL	N/A	• Initial screening • Does not provide pressure information (or, very limited pressure information if sealed test cell is used)
RSST	• Open to a larger containment vessel • Adiabatic	10 mL	1.05 (thin-walled)	Initial screening
ARC	• Closed • Adiabatic	10 mL	1.5 (thick-walled)	• Most applicable to reactions with low self-heating rates • Temperature related results need to account for ϕ factor
VSP2	• Closed • Adiabatic	100 mL	1.05 (thin-walled)	Useful for reactions with very high self-heating rates
RC1e	• Open/closed • Isothermal	• 2 L for ambient pressure vessels • 1 L for medium pressure vessels • 5 L for high pressure vessels	1.5 (thick-walled)	• Usually equipped with in-line analyzer such as Fourier transform infrared spectroscopy (FTIR) • Reaction mechanism and kinetics

13

1.2.1.2.   Characterization by calorimetry

Once reactive hazards are identified via the above preliminary screening, more insight into their mechanism and severity could be gained by calorimetry techniques and methodology. Specifically, calorimeters allow mimicking both desired and undesired scenarios potentially encountered in large-scale reactors by using small amounts of materials in lab. Two modes that calorimeters typically operate in are adiabatic and isothermal. The former is intended to study material thermal stability and obtain critical parameters, including adiabatic temperature rise (ΔT_{ad}), onset temperature for phase change or secondary reaction (T_{onset}), self-heating rate (dT/dt), maximum self-heating rate (dT/dt_{max}), pressure rise rate (dP/dt), and maximum pressure rise rate (dP/dt_{max}), for adiabatic scenarios resulting from, say, cooling failure, unintended external heating source like fire, or insufficient heat transfer within large reactors. The isothermal mode enables reliable measurement of reaction heat and provides data that could be further fitted to propose reaction pathway and kinetics owing to in-line analyzer kit allowing real-time monitoring of reaction progress.

Calorimeter testing is extremely essential in drug process development, especially during scale-up, for screening reactive hazards, determining operation conditions, designing relief systems, and proposing precautions and alternative routes (*e.g.*, Allian et al.[46]; González-Bobes et al.[47]; Likhite et al.[48]; Tuscanov et al.[34]; Wang et al.[49-51]; Zaborenko et al.[38]). Table 1.3 presents calorimeters widely used in the pharmaceutical and other industries. And as shown in the above examples, projects typically start with fast preliminary testing using DSC and RSST for detecting exotherm

and proving hypotheses, and move to more capable calorimeters depending on the initial results. The ϕ factor in Table 1.3, representing the thermal capacity ratio of test vessel to reaction mixture, should be calculated and considered on a case-by-case basis when interpreting temperature related results, as the solid vessel essentially acts as a thermal buffer and hence may render the results dangerously deviating given the small volume of reaction mixture used.

1.2.2. Managing reactive hazards

As mentioned by Bollinger and Crowl[52] and Hendershot[53], strategies for process risk management could be categorized as follows:

- *Inherent*: Completely eliminate hazards by employing nonhazardous materials and process conditions

- *Passive*: Reduce the likelihood or impact of hazards by well-designed process and equipment rather than the active functioning of add-on devices or procedures

- *Active*: Detect potentially hazardous process deviations and take corrective action accordingly by using active systems of control, interlock, emergency shutdown, and mitigation

- *Procedural*: Prevent incidents or minimize their impact by following management approaches such as operating procedures, administrative checks, and emergency response

Controlling reactive hazards could fit into the risk reduction framework by pursuing measures representative of these strategies, some of which could be found in

Crowl and Louvar[45]. Particularly, inherent and passive methods are more reliable and robust and therefore preferred over the other two for they rely on well-engineered system design rather than timely and appropriate intervention of people and devices.

1.2.3. Inherently safer design for reactors

As the ultimate strategy for managing reactive hazards, the concepts of inherent safety and inherently safer design were first put forth by Trevor Kletz back to the 1980s, who also continued to promote awareness and advancement of the concepts thereafter (Kletz[54-56]). According to the literature dedicated to the topic (*e.g.*, Bollinger and Crowl[52]; Hendershot[53]; Khan and Amyotte[57]), inherent safety entails the following four principles:

- *Minimize*: Reduce quantities of hazardous materials

- *Substitute*: Replace hazardous materials with less hazardous counterparts

- *Moderate*: Probe less hazardous operation conditions, physical states of materials, and routes that minimize consequences of accidental release of hazardous materials and energy

- *Simplify*: Reduce processing steps and associated pieces of equipment

In fact, remarkable inherently safer designs using these principles have been proliferating in the pharmaceutical industry even without switching to continuous syntheses. For example, Wang et al.[51] investigated safer scale-up strategies for pharmaceutical syntheses when complete elimination of dimethyl sulfoxide (DMSO), a widely used solvent subject to decomposition near its normal boiling point, is impossible due to either being used as both solvent and reactant or being produced as byproduct

16

while serving as solvent. For the former case, illustrated by the example of Pfitzner-Moffatt oxidation, substantial reduction in the amount of DMSO used and severity of accidental decomposition was achieved by adding N,N-dimethylacetamide (DMAc) as co-solvent, while for the latter, as exemplified by Corey-Chaykovsky reaction, significantly raised onset temperature of the reaction mixture was made available by replacing DMSO with N,N-dimethylformamide (DMF). Likewise, Likhite et al.[48] explored scalable synthesis of an oxadiazole-containing compound utilized as antiplatelet agent and imaging agent for Alzheimer's disease, whose synthetic route during preclinical studies involved an aza-rich intermediate that was shock sensitive and had low onset temperature and large heat release during thermal decomposition. To achieve safe scale-up to multi-kilo scale, the authors adopted Boc and Cbz (Bissantz et al.[58]) protecting groups in parallel, which led to much more thermally stable intermediates while maintaining the target yield.

As backed by Table 1.1 and 1.2 summarized from increasingly extensive research and application of continuous processing for pharmaceuticals, it is justifiable to conclude that continuous processing perfectly falls into the scope of inherently safer design and that it would generate beneficial overlap among the inherent safety principles mentioned above owing to process intensification and ease of control.

17

1.3 N-oxidation of Alkylpyridines

1.3.1. Significance and current production practice

Pyridine compounds are a commercially important class of organic species for pharmaceutical applications, owing to high bioactivity and versatility as synthetic precursors.[59,60] Alkylpyridine N-oxides are particularly valuable as intermediates in the syntheses of antiulcer, analgesic, and anti-inflammatory drugs. They contain an N-O functional group (Scheme 1.1) providing an effective means for pyridine ring activation which is more facile than direct syntheses from alkylpyridine precursors that are stable heterocyclic aromatic compounds having relatively low reactivity.[61] Figure 1.4 shows some of these synthetically important precursors that the current industrial practice uses for producing corresponding alkylpyridine N-oxides following Scheme 1.1. In these syntheses, hydrogen peroxide is used as the oxidizer, which theoretically only generates water as byproduct and has been successfully utilized as a clean, economical, and atomically-efficient oxidative candidate in many other applications (*e.g.*, Liu and Jensen[28,62]). Phosphotungstic acid (Figure 1.5), a Keggin-type heteropolyacid of formula $H_3PW_{12}O_{40} \cdot nH_2O$, is adopted as the catalyst owing to the excellent reaction selectivity towards the desired product (Misono[63,64]), i.e. alkylpyridine N-oxide.

Currently, industrial production of alkylpyridine N-oxides via Scheme 1.1 involves semi-batch operation in reactors venting to the atmosphere and running isothermally close to the boiling point of the reaction mixture (~100 °C).[65-67] Operation procedures normally start with charging the reactor with premixed alkylpyridine and catalyst. After the reactor is heated up to the target reaction temperature, an excess (30%

– 50%) of hydrogen peroxide (aq) is dosed at specific rate for a certain amount of time. When dosing is complete, the reaction is left towards completion and residual hydrogen peroxide in the end can be neutralized by appropriate chemicals.[68]
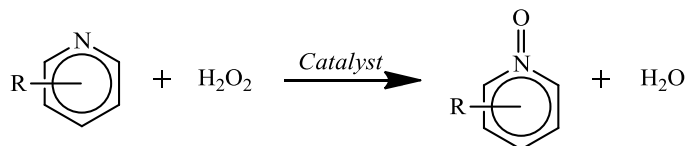
Scheme 1.1. Exothermic, liquid phase, homogeneous catalytic N-oxidation of alkylpyridines using phosphotungstic acid as the catalyst and hydrogen peroxide the oxidizing agent
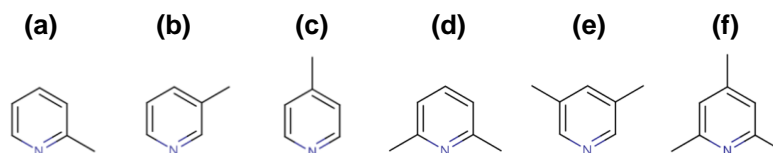
Figure 1.4. Synthetically important alkylpyridine precursors (a) 2-picoline (b) 3-picoline (c) 4-picoline (d) 2,6-lutidine (e) 3,5-lutidine (f) 2,4,6-collidine
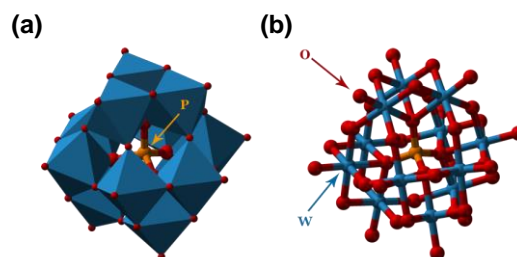
Figure 1.5. Structure of the phosphotungstate anion $H_3PW_{12}O_{40}$ showing (a) a tetrahedron PO_4 in the center and (b) twelve octahedra WO_6 surrounding it.
Modified from Wikipedia, https://en.wikipedia.org/wiki/Phosphotungstic_acid (accessed July 27, 2016)

1.3.2. Hazard analysis

The conventional semi-batch operation practice along with the properties of the chemicals involved and the reaction chemistry described in the previous section poses serious hazards endangering safety and productivity as illustrated below.

1.3.2.1. Chemical hazards

Major hazards of concern for the chemicals involved in Scheme 1.1 are listed in Table 1.4. For alkylpyridines, they are deemed flammable due to relatively low flash points. For example, the flash points for 2-picoline, 3-picoline, 2,6-lutidine, and 3,5-lutidine, are 27 °C, 38 °C, 37 °C, and 53°C respectively. In addition, although picolines are generally miscible with water, phase separation is quite evident when higher order alklypyridines (lutidines and collidines) take part in the reaction forming an organic phase and an aqueous phase, under which circumstance the phosphotungstic acid catalyst would almost exclusively remain in the aqueous phase[69,70] with hydrogen peroxide also present there. As a consequence, the parallel oxygen- and heat- generating hydrogen peroxide decomposition promoted by the catalyst, which is also highly sensitive to impurities (*e.g.*, Fe, Zn, Ni, Cr, and Mg) and conditions like temperature and pH, not only substantially challenges safety but also greatly jeopardizes productivity. Meanwhile, thermal stability of the product, i.e. alkylpyridine N-oxide, degrades as temperature rises, and decomposition is triggered beyond some threshold temperature (*e.g.*, ~200 °C for 2-picoline N-oxide and ~230 °C for 3-picoline N-oxide[68,71]), which induces release of both heat and non-condensable gases.

Table 1.4. Summary of hazards for chemicals involved in the catalytic alkylpyridine N-oxidation

Chemical	CAS No.	NFPA chemical hazard label	Major hazards
3-picoline	108-99-6	(3 / 3 / 0)	• Flammable • Corrosive (irritation to skin, can cause serious eye damage) • Acute toxicity through oral, inhalation, and dermal
Hydrogen peroxide (30 wt% aq)	7722-84-1	(0 / 3 / 1 / OX)	• Unstable and decomposes very easily under the presence of some impurities • Strong oxidizer • Corrosive (irritation to skin, can cause serious eye damage) • Acute toxicity through oral
Phosphotungstic acid	12501-23-4	(0 / 2 / 0)	Corrosive (irritation to skin, can cause serious eye damage)
3-picoline N-oxide	1003-73-2	(1 / 2 / 0)	Irritation to skin and eye

1.3.2.2.   *Operation hazards*

Stoessel[72] introduces the criticality index method, shown in Figure 1.6, to identify potential reaction runaway scenarios by reaction categories in terms of the relative magnitude of four types of temperature, namely nominal process temperature (T_p), boiling point of solvent (T_b), the maximum temperature rise of synthesis reaction

(MTSR), and the temperature when the maximum adiabatic self-heating rate in 24 h is reached (T_{D24}). The method concludes that reaction runaway risks are in ascending order from class 1 to class 5 and that reactions of class 1 – 3 are not likely to reach the onset temperature for secondary reactions through self-heating.
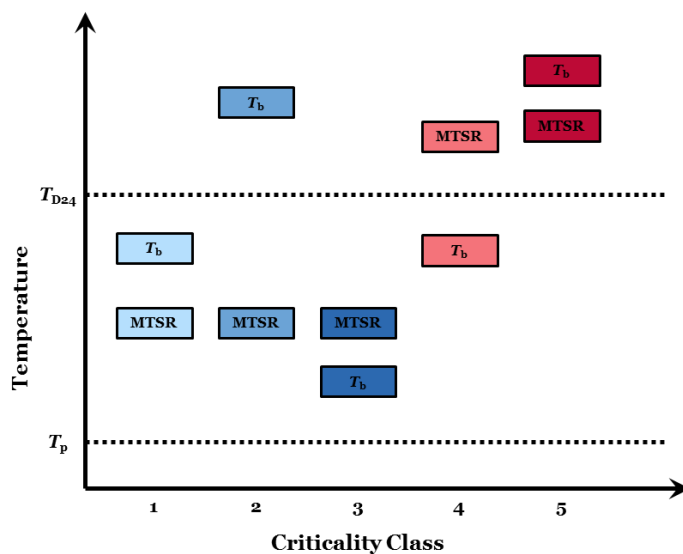
Figure 1.6. Criticality classification of reaction runaway potential

Inspection of the calorimetric testing results of the four critical temperatures for N-oxidation of some alkylpyridines studied by Saenz-Noval[71] and Pineda-Solano[68] reveals that Scheme 1.1 generally belongs to class 4, which means should a reaction runaway occur the reaction temperature could ramp up via self-heating to the onset temperature of secondary alkylpyridine N-oxide decomposition, which, as mentioned in the previous section, generates both heat and non-condensable gases that would

challenge the thermal and mechanical integrity of the reactor. Therefore it is critical to prevent runaway scenarios, which may be induced by cooling failure, vigorous decomposition of hydrogen peroxide (resulting from $30 - 50\%$ excess use currently employed, accumulation at the end of dosing, phase separation for higher order alkylpyridines, impurities, or accidental external heating), and insufficient mixing. In the meantime, the oxygen-enriched vapors along with the high flammability of alkylpyridines pose a severe hazard of fire and explosion. Additionally, the large inventories of reactants dictated by batch-wise operation is by no means less disturbing, which again garners and justifies efforts for transition to flow.

1.3.3. Previous research

Previous research to address the above challenges may be divided into two areas of emphasis, (i) hazard identification and quantitative assessment via investigation of reaction pathway and kinetic measurements by calorimetry,[65-67] and (ii) development of alternative practices, mainly focusing on either optimizing operation conditions or improving reactor design by following the inherently safer design principles.[54-56]

1.3.3.1. Reaction kinetics

The research was intended to explore reaction pathways for Scheme 1.1 and develop a fit-for-use kinetics model as well as measuring associated kinetic parameters applicable to different alkylpyridines given in Figure 1.4. By running the reaction in an open semi-batch reactor using 2-picoline as the starting material, Sempere et al.[66] and Papadaki et al.[67] first proposed a kinetic model based upon the Langmuir-Hinshelwood mechanism and estimated kinetic parameters, including activation energies, frequency

factors, and chemical equilibrium constants, based upon power profiles collected from calorimeters. This model was subsequently adapted by Papadaki and Gao[65] in order to establish a more generic one that would be also applicable to other compounds in the alkylpyridine family such as 3-picoline, 4-picoline, lutidines, and collidines.

As shown by Pineda-Solano et al.[73] for industrially relevant operating window of 110 – 125 °C and 2 – 4 bar, the parallel undesired decomposition of hydrogen peroxide is not appreciable, while the dominant elementary steps for Scheme 1.1 are cited here in Eqs. (1.1) and (1.2). In these equations, A, B, N, W, Z, and BZ denote relevant chemical species, namely alkylpyridine, hydrogen peroxide, alkylpyridine N-oxide, water, catalyst, and some intermediate compound respectively (note that a quasi-equilibrium adsorption of hydrogen peroxide on free catalyst site forming the intermediate BZ is assumed[65-67] as presented by Eq. (1.3)). The resulting overall rate expression, given by Eq. (1.4) with square brackets indicating species concentrations, is the sum of the reaction rates for the two dominant steps (1a and 1b). Kinetics and thermodynamic parameters associated with Eq. (1.4) are detailed in Table 1.5.

Step 1a: $A + BZ \rightarrow N + W + Z$ (1.1)

Step 1b: $A + B \rightarrow N + W$ (1.2)

Quasi-equilibrium adsorption of hydrogen peroxide on free catalyst site: $B + Z \leftrightarrow BZ$

(1.3)
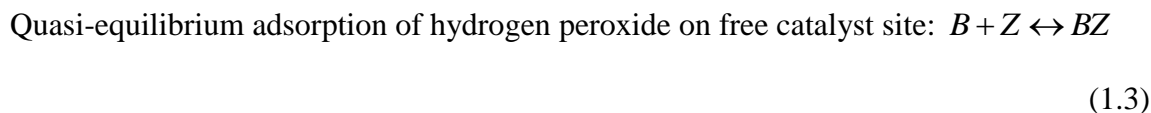
$$r = r_{1a} + r_{1b} = \frac{k_{1a} K_b [A][B][Z]}{1 + K_b [B]} + k_{1b} [A][B]$$ (1.4)

Table 1.5. Kinetic parameters and chemical equilibrium constant in the overall rate expression given by Eq. (1.4)

Variables	Units	Pre-exponential frequency factors	$\frac{E}{R}$ and $\frac{\Delta H}{R}$ (K)
$k_{1a} = A_{1a}\exp(-\frac{E_{1a}}{RT})$	$L \cdot mol^{-1} \cdot s^{-1}$	$\exp(8.08)^{\dagger}$	$3952.3^{\dagger}$
$k_{1b} = A_{1b}\exp(-\frac{E_{1b}}{RT})$	$L \cdot mol^{-1} \cdot s^{-1}$	$\exp(28.14)^{\dagger}$	$12989^{\dagger}$
$K_b = A_b\exp(-\frac{\Delta H_b}{RT})$	$L \cdot mol^{-1}$	$\exp(25.12)^{\dagger}$	$7927^{\dagger}$

†Values cited from Ref. (66)

1.3.3.2. *Hazard characterization and alternative operation conditions*

Besides the generic kinetic model given by Eqs. (1.1) − (1.4), Papadaki and Gao[65] also provided preliminary evidence that higher operation temperature would favor selectivity, depress peroxide decomposition, and promote phase homogeneity of reaction mixture when higher order alkylpyridines are used as starting materials. Therefore extensive research, also leveraging reaction calorimetry, has been carried out at the Mary Kay O'Connor Process Safety Center, Texas A&M University in order to perform hazard evaluation of the reacting system and to extend operation space.

Saenz-Noval et al.[71,74,75] revealed that catalyst presence would expedite the secondary decomposition of 2-picoline N-oxide once its onset temperature is reached and that the decomposition generates both heat and non-condensable gases, based upon which the authors argued that it was of great importance to prevent initial rapid temperature rise primarily through minimizing or eliminating decomposition of

hydrogen peroxide. Consequently, the authors proved that running the reaction for 2-picoline in closed reactors and at elevated temperature could effectively suppress the decomposition and that adding a third component, say, acetic acid, to the mixture of 2,6-lutidine and water could help diminish phase separation.

Subsequently, Saenz-Noval[71] and Pineda-Solano et al.[73,76] extended the above studies of product decomposition and the effect of alternative conditions on reaction performance to other alkylpyridines, including 3-picoline, 2,6-lutidine, 3,5-lutidine, and 2,4,6-collidine. Specifically, for 3-picoline, 2,6-lutidine, 3,5-lutidine, and 2,4,6-collidine, the authors identified the threshold temperatures for onset of the decomposition of their corresponding N-oxide and confirmed non-condensable gas generation. Furthermore, they authors also explored the mechanism for 3-picoline N-oxide decomposition, which was complex with oxygen detachment and non-condensable gas generation being the dominant steps while other minor steps like polymerization also being likely. Meanwhile, the decomposition was shown to be much more sensitive to temperature than catalyst concentration. To optimize operation conditions, the authors found out that higher temperature in the range of 110 – 125 °C helped promote conversion and greatly depress the competitive decomposition of hydrogen peroxide for the cases of 3-picoline and 3,5-lutidine. And besides temperature as Saenz-Noval discovered,[71] the authors also studied the influence of the amount of catalyst and the dosing rate, and concluded that a relatively high value for the former combined with a relatively low value for the latter was favored in terms of safety and efficiency. However, these results did not hold true for the cases of 2,6-lutidine and 2,4,6-collidine as phase separation was dominant.

In addition, Pineda-Solano[68] also exploited in-line FTIR for process monitoring, which essentially reflected the recommendation by PAT[5] for real-time process analyzers as mentioned earlier in this dissertation. As preliminary study, the author focused upon investigating calibration protocols such as reaction-specific selection of wavenumbers, temperatures, and mixture compositions.

1.4 Dissertation Overview

This dissertation aims to overcome inherent challenges with synthetically important but potentially hazardous chemistry by proper continuous reactor design based upon reaction engineering principles, systems fundamentals, and process safety concepts. For illustration, the liquid phase, homogeneous catalytic exothermic N-oxidation of alkylpyridines (Scheme 1.1), whose substantial safety concerns render scale-up of capacity cumbersome for current semi-batch practice, is investigated. By exploiting kinetics (Eqs. (1.1) – (1.4) and Table 1.5) and reactive hazards information previously obtained from calorimetry studies by the Mary Kay O'Connor Process Safety Center at Texas A&M University, attempts were made to explore both a jacketed continuous-stirred tank reactor (CSTR) design and a segregated-feed membrane reactor design for the reaction, which will be presented in detail in Chapter II and Chapter III respectively. Chapter IV summarizes the work accomplished in this dissertation along with recommendations for future work.

CHAPTER II

CSTR DESIGN AND OPERATION[*]

2.1   Introduction

In this chapter, a continuous stirred tank reactor (CSTR) is selected for analysis. Among all flow reactors, both conventional ones (*e.g.*, continuous stirred tank reactors and plug flow reactors) and novel ones (*e.g.*, membrane reactors and microchannel reactors), CSTRs are favored for highly exothermic reactions owing to spatially uniform concentration and temperature profiles which facilitate controllability and are thus easier to implement. Insight obtained from CSTR analysis provides a fundamental basis for subsequent analysis of more complex configurations such as tubular reactors or membrane reactors.

Systematic mathematical approaches have long served chemical reactor design and operation purposes.[77] Bilous and Amundson's landmark paper[78] in 1955 treated CSTR as a dynamic system and employed Lyapunov's first method of linearization to yield a pair of algebraic conditions for local stability of steady states. It triggered subsequent boom of research with respect to CSTR steady-state multiplicity or dynamics, or both in some cases.[79] On the steady-state branch, Van Den Bosch and Luss[80] presented very strong necessary and sufficient criteria for unique or multiple steady states of an adiabatic CSTR accommodating an nth-order ($n \geq 0$) reaction while

28

Refs. (81) and (82) established the corresponding exact necessary and sufficient criteria with Ref. (82) being also applicable to nonadiabatic cases. Based upon singularity theory, which was developed and tentatively applied to CSTRs,[82,83] Balakotaiah and Luss[85-87] exhibited complex multiplicity features of CSTRs, the steady states of which could be described by a single algebraic equation, by dividing reactor parameter space into different regions corresponding to different numbers of steady states and predicting all possible types of bifurcation diagrams, which depict the dependence of the steady state of a state variable (*e.g.*, concentration, temperature, and conversion, etc.) on a slowly varying design or operation variable (*e.g.*, Damköhler number, residence time, etc.). On the dynamic branch, except from a series of papers by Amundson and his co-workers (*e.g.*, Aris and Amundson[88-90]) which studied transient behaviors of a CSTR and the effect control systems had on altering the dynamics, a classical paper by Uppal, Ray, and Poore[91] performed an exhaustive study of the dynamic behavior of a CSTR with a single first-order, irreversible, exothermic reaction, the result of which was the demarcation of the reactor design and operation parameter plane based upon steady-state and dynamic characteristics. It was later complemented by Williams and Calo[92] and Kwong and Tsotsis[93] which established finer structure of the parameter plane as well as corresponding new bifurcation diagrams and phase plots. It should be noted that similar spirits could be followed to study multiplicity and stability problems of other chemical reacting systems, say, catalytic pellets and tubular reactors. Razón and Schmitz[94] and Morbidelli et al.[95] provided a convenient review for such studies.

Inspired by all these seminal works with Uppal et al.[91] and its subsequent complements[92,93] in particular, the CSTR design and operation parameter plane for Scheme 1.1 will be demarcated according to multiplicity and stability characteristics. In combination with productivity specifications, the demarcation will be used to identify conditions that facilitate safer and more efficient production of alkylpyridine N-oxides. Furthermore, the importance of careful selection of initial conditions and their effect on start-up time will be illustrated by a case study. Though similar techniques have been applied to several continuous polymerization processes[96] as practical applications of classical theories, they have, to our knowledge, not been reported yet in the literature for exploring continuous processing of fine chemicals and pharmaceuticals which often features complex reaction kinetics and therefore renders analytical demarcation expressions that were derived exclusively for a pseudo first-order irreversible reaction under certain assumptions in those pioneering works[91-93] unwieldy.

The rest of this chapter is organized as follows. The next section presents the CSTR model used in this work. It also gives a brief description of relevant theory to determine the reactor steady-state and dynamic characteristics with detailed criteria and derivation steps shown in Appendix B. The key results are presented and discussed in Section 2.3. Conclusions form the last part of this chapter.

2.2 Theoretical

2.2.1. Reactor model equations

A continuous stirred tank reactor (CSTR) model is employed, assuming constant inlet and outlet volumetric flow rate, liquid phase reaction volume, coolant temperature, heat transfer area and coefficient. Likewise, the heat of reaction and reaction mixture physicochemical properties such as average heat capacity and density are assumed to be insensitive to temperature and therefore constant. Lastly, since no significant crystallization involving reactants, catalyst, or product is reported in those previous experimental studies[65-67,73] regarding the chemistry considered here, the catalyst is assumed to be completely dissolved in the alkylpyridine feed flow and its concentration be constant within the reactor and equal to the feed condition. The resulting species A (alkylpyridine) and B (hydrogen peroxide) mass balance and the overall liquid phase energy balance for the well-mixed nonadiabatic CSTR are established as shown in Eqs. (2.1) – (2.3).

$$V\frac{d[A]}{dt'} = -Vr_{ox} + q\left([A]_f - [A]\right) \tag{2.1}$$

$$V\frac{d[B]}{dt'} = -Vr_{ox} + q\left([B]_f - [B]\right) \tag{2.2}$$

$$\overline{\rho C_p}V(1+\varepsilon)\frac{dT}{dt'} = V(-\Delta H_{ox})r_{ox} + q\overline{\rho C_p}\left(T_f - T\right) + Ua(T_c - T) \tag{2.3}$$

The above system of coupled differential equations may be recast in terms of alkylpyridine conversion to reduce the number of dependent variables, recognizing that the concentration of hydrogen peroxide is related to alkylpyridine conversion via

31

reaction and feed stoichiometries. The resulting CSTR model describing alkylpyridine conversion and reactor temperature changing in time is presented in Eqs. (2.4) and (2.5).

$$\frac{dx}{dt'} = \left[\frac{k_{1a}K_b[Z]}{1+K_b(\alpha-x)[A]_f} + k_{1b}\right](1-x)(\alpha-x)[A]_f - \frac{q}{V}x \tag{2.4}$$

$$(1+\varepsilon)\frac{dT}{dt'} = \frac{(-\Delta H_{ox})}{\rho C_p}\left[\frac{k_{1a}K_b[Z]}{1+K_b(\alpha-x)[A]_f} + k_{1b}\right](1-x)(\alpha-x)[A]_f^2 + \frac{q}{V}(T_f - T) + \frac{Ua}{\rho C_p V}(T_c - T) \tag{2.5}$$

Table 2.1. Constants in Eqs. (2.4) and (2.5)

Variables	Units	Values
α	dimensionless	1.05
V	L	1
ε	dimensionless	0
ΔH_{ox}	kJ $\cdot$ mol^{-1}	-160
$[Z]$	mol $\cdot$ L^{-1}	0.0021
T_f	K	323.15
T_c	K	298.15

Table 2.2. Heat of reaction for N-oxidation of different alkylpyridines[68] (kJ $\cdot$ mol^{-1})

	3-picoline	3,5-lutidine	2,6-lutidine	2,4,6-collidine
$(-\Delta H_{ox})$	120 – 190	150 – 170	150 – 170	140 – 180

Values for design parameters in the above dynamic CSTR model are summarized in Table 2.1. The feed concentration ratio of hydrogen peroxide to alkylpyridine in the overall feed flow, α, is chosen as 1.05 to minimize the accumulation of hydrogen peroxide in the reactor as well as in the outflow for the sake of safety, efficiency and economics. For illustrative purpose as well as ease of future lab-scale experimental validation, reaction volume V is assumed to be 1 L. Catalyst concentration, $[Z]$, is chosen as $0.0021 \, \text{mol} \cdot \text{L}^{-1}$ since Pineda-Solano et al.[73] reported that for semi-batch-wise operation the influence of the amount of catalyst used was trivial in the range of 2 g to 6 g (or equivalently, $0.0017 \, \text{mol} \cdot \text{L}^{-1}$ to $0.0052 \, \text{mol} \cdot \text{L}^{-1}$ at the end of dosing) when the reaction was carried out at elevated temperature (110 °C – 125 °C). Inlet flows are preheated to 50 °C (T_f) before entering the reactor while cooling temperature T_c is equal to room temperature (25 °C). ε, defined in the Nomenclature section, represents the thermal capacity ratio of solid equipment parts such as reactor wall, bottom plate, stirrer and impeller to reaction mixture. As can be seen from Eq. (2.5), it does not affect reactor steady state but rather dynamic behaviors. Chang and Schmitz[97] investigated the effect of ε for a 1.01 L CSTR made of type 304 stainless steel where the exothermic liquid phase reaction between sodium thiosulfate and hydrogen peroxide took place. Their experimental results of reactor temperature oscillation amplitudes fell between the amplitudes predicted from simulation with $\varepsilon = 0$ and $\varepsilon = 0.02$, and were located closer to the theoretical curve for $\varepsilon = 0$. They also found out that simulation with $\varepsilon = 0.02$ resulted in milder oscillation behaviors than the case of $\varepsilon = 0$ because larger ε would provide more thermal buffer. Since our target experimental setup, in terms of dimensions

and material, is very similar to that used in Chang and Schmitz,[97] and the heat capacity of current reaction content is of the same order of magnitude as that for the mixture in Chang and Schmitz,[97] ε is assumed to be zero in this study. Based upon heats of reaction for the N-oxidation of various alkylpyridines, obtained experimentally by Pineda-Solano[68] and summarized in Table 2.2, a constant heat of reaction of $160\,\mathrm{kJ\cdot mol^{-1}}$ is employed in the present study. Fluid-phase density and heat capacity are assumed to be equal to feed conditions and therefore depend upon the weight fraction of hydrogen peroxide aqueous solution. Inlet hydrogen peroxide weight fraction also determines the overall feed concentration of alkylpyridine, $[A]_f$, given physicochemical properties of a specific alkylpyridine and the feed stoichiometry (α), as detailed in Appendix A.

To this end, the first-principles reactor model equations are complete and recast in a form that is ready to serve reactor steady state and dynamics analysis purposes with β and δ as well as Da being parameters of interest.

2.2.2. System analysis

The steady-state and dynamic behaviors of the resulting CSTR model as a function of the dimensionless cooling number δ, or the Westerterp number as named in Westerterp et al.,[98] and the dimensionless adiabatic temperature rise β may be obtained using bifurcation theory. Steady-state multiplicity depends on existence of saddle-node bifurcation while the stability characteristics of limit cycles can be determined from the sign of a function which was derived in Poore[99,100] and evaluated at the critical point where oscillation ensues. A brief synopsis of criteria to determine the existence of multiple steady states and limit cycles as well as their stability is given in Appendix B.

Resulting CSTR behavior is demarcated within the two-dimensional parameter space following the previous analyses of Kwong and Tsotsis,[93] Uppal et al.,[91] and Williams and Calo,[92] delineating relationships between steady-state conversion of alkylpyridine x and reactor temperature T to Damköhler number Da, with each unique region corresponding to a characteristic phase plot (x vs. T) describing the dynamic trajectories from initial conditions towards the final steady state or limit cycle.

2.3   Results and Discussion

2.3.1. Parameter space demarcation

To divide the parameter space into regions characterized by different steady-state and/or dynamic behaviors, Uppal et al.[91] derived analytical expressions for region boundaries for a dummy first-order irreversible reaction under assumptions such as large activation energy, equal feed and coolant temperatures, etc. For this work, however, such analytical expressions are intractable mainly due to the relatively complex kinetic model. Therefore a grid search method is adopted to obtain the region boundaries as follows. First, a subset of randomly generated points within the parameter space is categorized in terms of system behavior using the criteria and calculation steps detailed in Appendix B. These resulting qualitatively distinct groups are set as a *priori* and a considerable number of points in the parameter space are iteratively tested against the criteria and incorporated into the corresponding a *priori* categories. If it happens that a point gives rise to behaviors that are not shared by any of the existing categories, a new category will be added. Fifteen types of behaviors are observed for the current system, as shown

in Figure 2.1. In keeping with previous similar studies,[91-93] the fifteen unique types of behaviors are grouped into six regions according to their steady-state multiplicity patterns and existence and location of limit cycles, which are summarized in Table 2.3. It can be seen from Table 2.3 that region III, IV, V and VI could be further divided into several sub-regions, as suggested by the different types of typical bifurcation diagrams that could be expected within the region. Moreover, each region features some typical types of phase plots, as also reported in Table 2.3, which show how trajectories starting from arbitrary initial conditions reach the final steady state or limit cycle. These phase plots are displayed in Figure 2.2.

After an exhaustive grid search, region information for a large amount of points (55264 points in total; the range for δ is from 0 to 4 and is unevenly discretized at a maximum interval of 0.05 and a minimum of 0.005, while the range for β is from 0 to 68.8 with a maximum interval of 0.49 and a minimum of 0.012) in the parameter space is fitted to obtain approximate region boundaries as shown in Figure 2.3(a) – (c), where solid lines represent boundaries among I-VI and dashed lines sub-region boundaries. Figure 2.3(c) – (d) suggest that the difference in the value of β between IVc-IVd and IVd-IVa boundaries at the same δ is very small, ranging from 0 to 0.12.
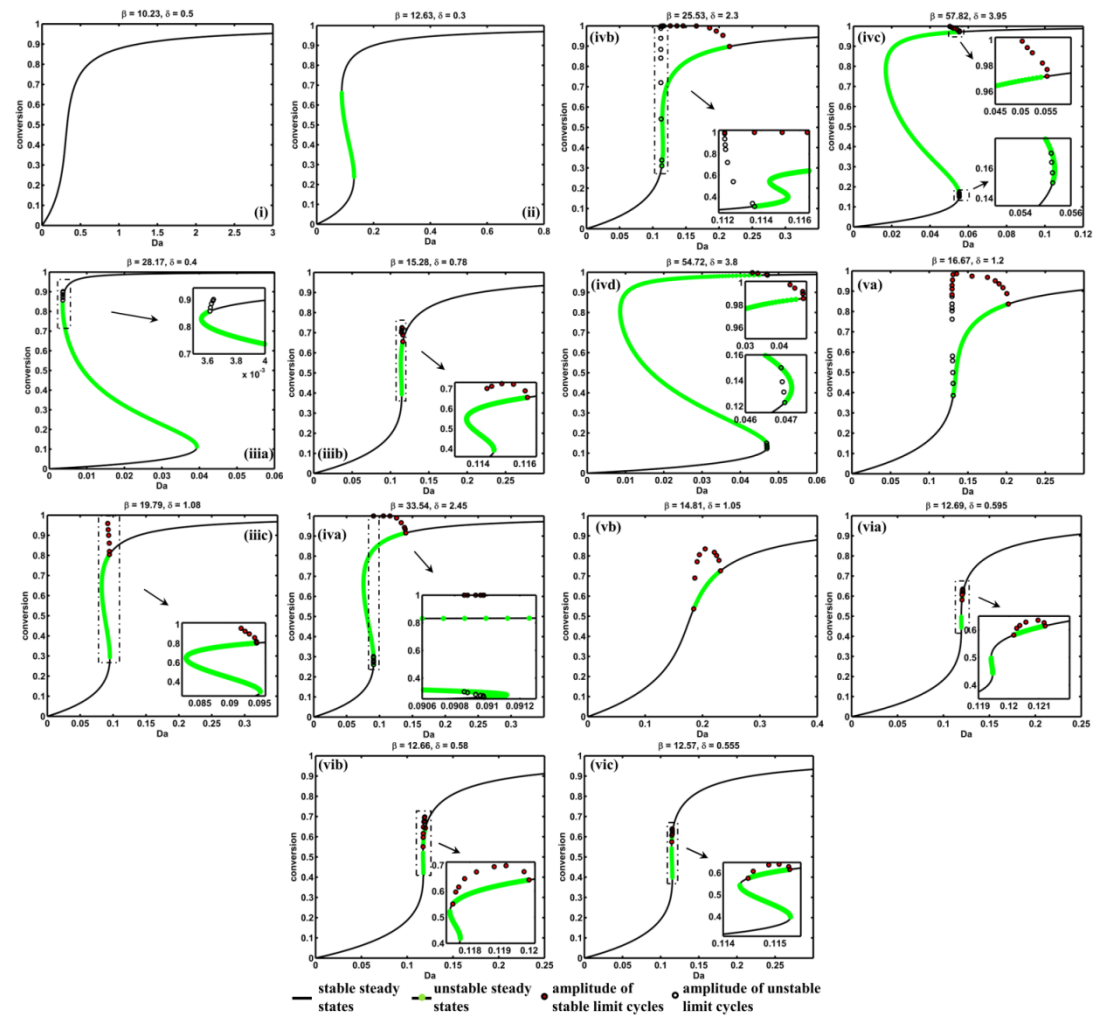
Figure 2.1. Typical bifurcation diagrams (i) – (vic)
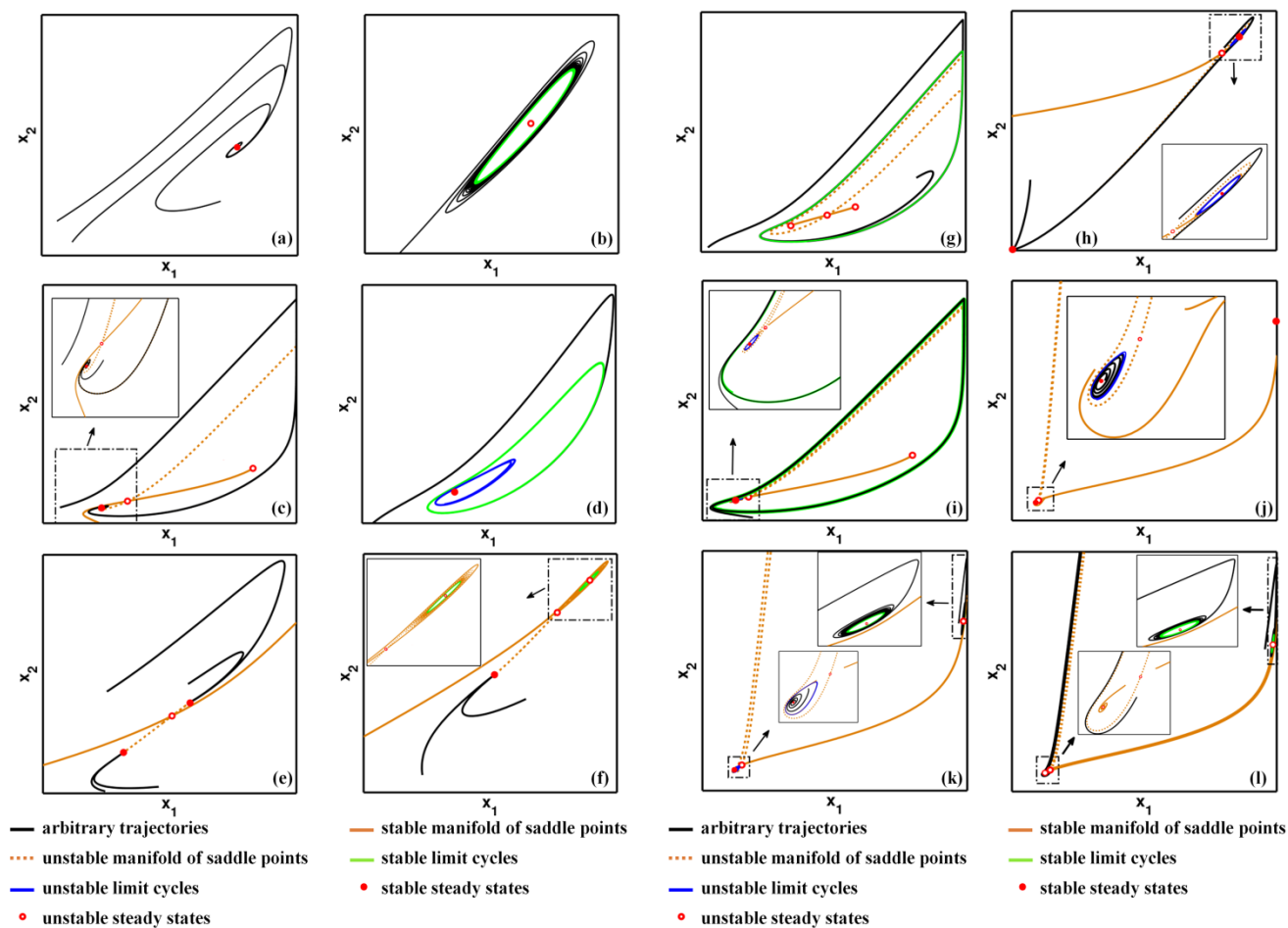
Figure 2.2. Typical phase plots (a) – (l) where x_1 represents the conversion of alkylpyridine $(\frac{[A]_f - [A]}{[A]_f})$ while x_2 the dimensionless reactor temperature $(\frac{T - T_f}{T_f}\gamma)$

38

Table 2.3. Summary of static and dynamic characteristics of region I-VI

Region	No. of steady states	Existence of limit cycles		Typical bifurcation diagrams (Figure 2.1)	Typical phase plots (Figure 2.2)
		Extinction branch	Ignition branch		
I	1	No	No	(i)	(a)
II	1-3-1	No	No	(ii)	(a) (e)
III	1-3-1	No	Yes	(iiia) – (iiic)	(a) (b) (c) (e) (f) (h)
IV	1-3-1	Yes	Yes	(iva) – (ivb)	(a) – (g), (i) – (l)
V	1	Yes[*]	Yes[*]	(va) (vb)	(a) (b) (d)
VI	1-3-1	No	Yes[**]	(via) – (vic)	(a) (b) (e) (f)

[*]For region V, there exist two critical points on the monotonic x vs. Da curve that give rise to limit cycles
[**]For region VI, there exist two critical points on the ignition branch that give rise to limit cycles
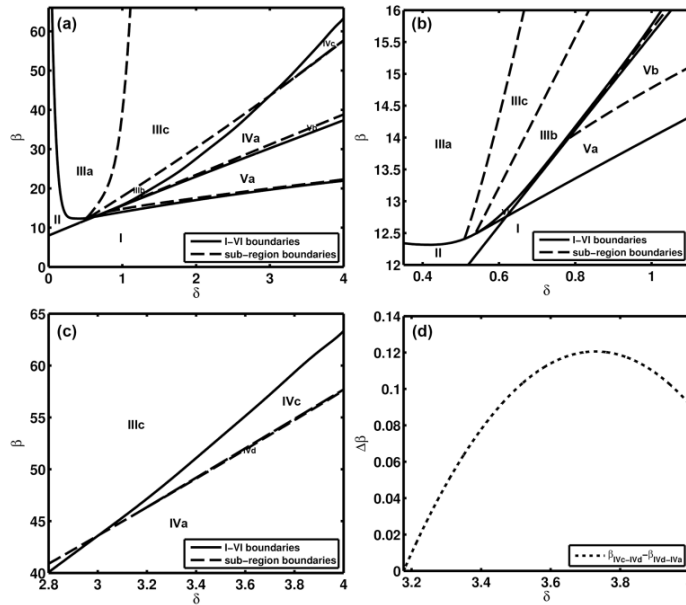
Figure 2.3. Region boundaries of the (δ, β) parameter space (a) Full parameter ranges of interest, (b) and (c) Magnified views of (a) for different ranges of δ, (d) Difference in β between IVc-IVd and IVd-IVa boundaries, i.e. $\Delta\beta = \beta_{\text{IVc-IVd}}(\delta) - \beta_{\text{IVd-IVa}}(\delta)$

2.3.2. Condition screening in the parameter space

The resulting (δ, β) design space is evaluated in terms of steady-state reactor performance. Nominal values for screening criteria are specified as follows. The lower bound of the temperature window is set at 110 °C since previous studies[68,73] suggest that above this temperature excess usage of hydrogen peroxide may be avoided, which consequently minimizes the competitive decomposition of hydrogen peroxide, as mentioned earlier. The upper bound of the temperature window is set at 125 °C, above which vaporization of the liquid mixture is significant. Meanwhile, the minimum conversion is tentatively set at 95%, which is in accordance with results in Pineda-Solano et al.[73]

For each point previously mapped in terms of steady-state and dynamic behavior in the (δ, β) parameter space, steady-state performance for the highest conversion point on the extinction branch and for the lowest conversion point on the ignition branch of the conversion-Da bifurcation diagram are calculated. If one and/or both of the two points satisfy all performance requirements, which were specified in the previous paragraph, the corresponding (δ, β) node may be a candidate design and Da can be further tuned in the neighborhood of the highest and/or the lowest point in order to achieve more stability and performance margin. For region II-VI, the highest/lowest point on the extinction/ignition branch is defined as the point with the highest/lowest conversion (or equivalently, temperature) among all extinction/ignition points that are the unique stable steady state at a given Da and are not encircled by a limit cycle. For region I, if the

40

maximum achievable temperature as *Da* varies is lower than the minimum acceptable temperature, this node does not need to be further screened against other requirements and should be discarded since the reactor is too cold for the reaction to initiate. If the maximum achievable temperature is higher than the minimum acceptable temperature but lower than the upper bound of the desired temperature window, the corresponding 'highest point on the extinction branch' would be set at the lower temperature bound and the corresponding 'lowest point on the ignition branch' the upper temperature bound. If the maximum achievable temperature exceeds the upper temperature bound, the corresponding 'lowest point on the ignition branch' would be set at the upper bound instead.
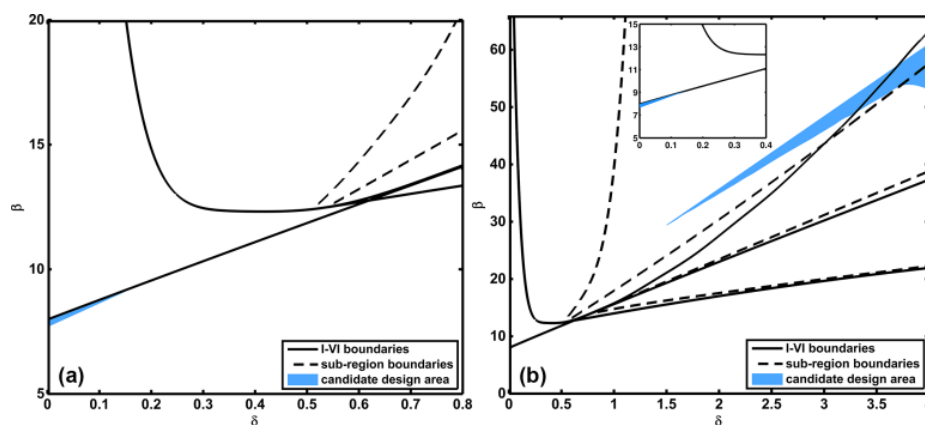
Figure 2.4. Screening results under nominal performance criteria values (a) When the highest extinction points are evaluated, (b) When the lowest ignition points are evaluated

Figure 2.4 presents screening results under the aforementioned nominal criteria values. It can be seen from Figure 2.4(a) that only a narrow band of δ and β belonging to region I satisfies all the requirements when the so-defined highest extinction points are adopted. Within the band, the maximum production rate among the highest extinction points is merely 0.1353 ton/L/yr, which is achieved at $\delta = 0.04$, $\beta = 8.268$ and $Da = 1.041$ with steady-state conversion being 95.38% and steady state temperature 110 °C. This substantiates the assertion that satisfactory conversion and overall throughput could hardly be achieved simultaneously in region I since relatively large Da number is often required to achieve high enough conversion, which results in low overall productivity. For those δ and β outside the band, the low conversion and/or temperature at the extinction points make(s) them unqualified, as suggested by Figure 2.5 (a) and (b). Figure 2.4 (b) shows that when the lowest ignition points are evaluated there is not only a narrow band in region I (upper inset), which is still of rather low productivity, but also a qualified zone in region III and IV. Within this zone, the production rate, which is calculated on a 300-day working year basis with left days for maintenance, cleaning, and start-up/shutdown, has a minimum of 2.562 ton/L/yr (at $\delta = 4$, $\beta = 53.62$, $Da = 0.5014$, conversion = 95.03% and temperature = 111.9 °C) and a maximum of 4.809 ton/L/yr (at $\delta = 3.95$, $\beta = 60.35$, $Da = 0.3043$, conversion = 96.61% and temperature = 124.8 °C). Figure 2.5 (c) and (d) reveal that for nodes that do not belong to the band or the zone, they are excluded due to low/high temperature and/or low conversion.
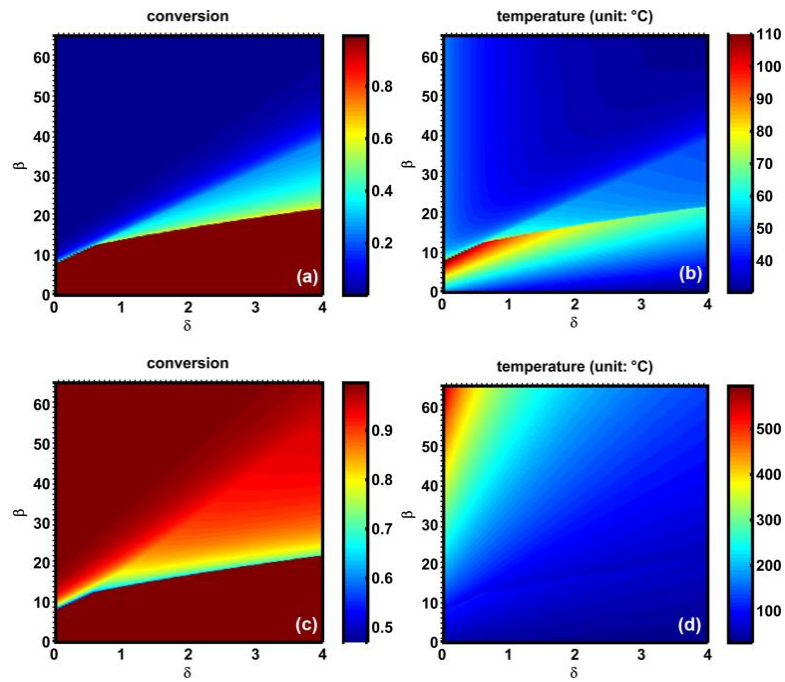
Figure 2.5. Performance of the highest extinction points (a, b) and the lowest ignition points (c, d)

2.3.2.1. *Effect of the maximum temperature limit*

It has been mentioned that as long as the maximum temperature limit is higher than 110 °C it does not influence screening results when the highest extinction points are evaluated since most of the nodes in the parameter space lead to low conversion or temperature. It is also the case for the narrow band in region I when the lowest ignition points are evaluated, as can be seen from the upper inset of Figure 2.6 that different maximum temperature limits share a common candidate design area in region I. However, the maximum temperature limit does affect the qualified zone in other regions. Indeed, it is found out that no other candidate conditions would be available until the

limit is above 111.9 °C while the minimum temperature and conversion limits are fixed at their nominal values. Candidate design area in regions other than region I for different maximum temperature limits higher than 111.9 °C is displayed in Figure 2.6. It can be seen that as the limit increases the candidate area expands and its upper boundary gets closer to the *β*-axis as well as the upper left corner of the space. It should be noted that as the targeting reactor temperature increases, the operating pressure should be raised accordingly so as to depress vaporization of the liquid mixture.
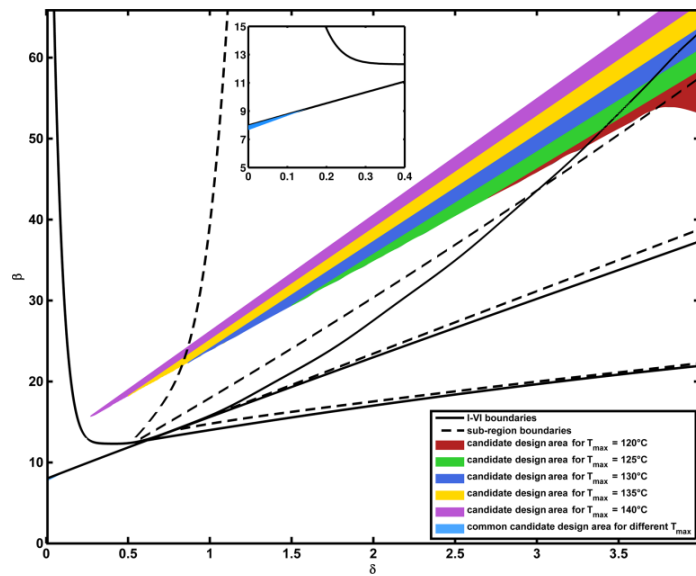
Figure 2.6. Effect of the maximum temperature limit on screening results when the lowest ignition points are evaluated while the minimum temperature and conversion limits are 110 °C and 95% respectively
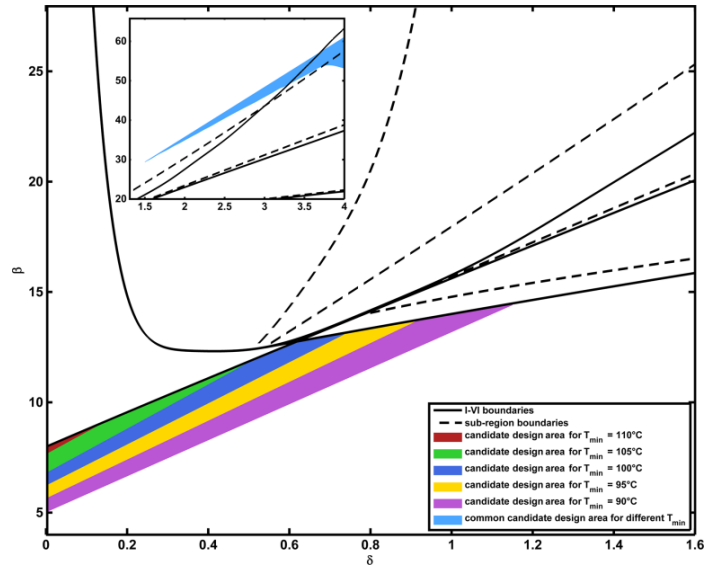
Figure 2.7. Effect of the minimum temperature limit on screening results when the lowest ignition points are evaluated while the maximum temperature and the minimum conversion limits are 125 °C and 95% respectively

2.3.2.2.   *Effect of the minimum temperature limit*

Figure 2.7 summarizes the effect of the minimum temperature limit on screening results when the lowest ignition points are evaluated with the maximum temperature and the minimum conversion limits being fixed at 125 °C and 95% respectively. Not surprisingly, different minimum temperature limits share the same candidate design area (presented in the upper inset of Figure 2.7) in region III and IV as the nominal case in Figure 2.4(b) because this area is exclusively determined by the maximum temperature limit on the top and the minimum conversion limit at the bottom. However, compared to the nominal case, the narrow band located in region I enlarges as the minimum temperature limit decreases. Simulation also indicates that the band will disappear if the

45

limit is raised above 112.9 °C. Similar results regarding the narrow band in region I are obtained when the highest extinction points are used for evaluation. It is worth mentioning that decomposition of hydrogen peroxide needs to be incorporated into the reactor model since it is very likely to be nontrivial when the reactor is operated at lower temperatures, which could lead to more exotic system behaviors.

2.3.2.3. *Effect of the minimum conversion limit*

When the highest extinction points are evaluated, the minimum conversion limit does not affect the narrow band in Figure 2.4(a) as long as it is lower than 95.38%. Otherwise, as the limit increases, the band keeps shrinking and completely disappears when the limit exceeds 99.86%. When the lowest ignition points are evaluated, nodes in the narrow band in the upper inset of Figure 2.8 lead to conversions that are almost 100%, which means the minimum conversion limit hardly has any effect on this band. However, the limit effectively influences the candidate area that lies above the band if it is higher than some critical value. In fact simulation results suggest that the candidate area looks the same as the one for $x_{\min} = 80\%$ presented in Figure 2.8 with the maximum and minimum temperature limits determining the upper and lower boundary respectively if the limit is lower than 80.37%. Once it is set above this critical value, the area shrinks and the lower boundary for low δ values is determined by the conversion limit instead while for high δ values it is still determined by the minimum temperature limit. If the conversion limit goes beyond 94.94%, the lower boundary would be entirely dependent on it and the area would disappear if it is raised above 96.61%.
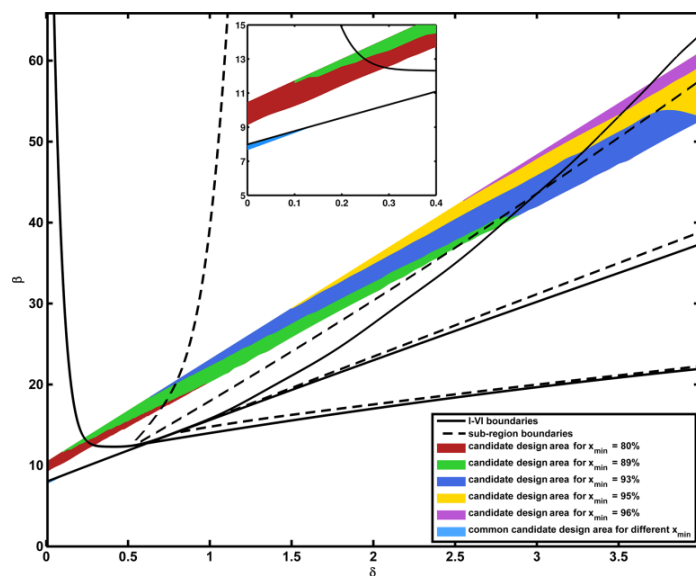
Figure 2.8. Effect of the minimum conversion limit on screening results when the lowest ignition points are evaluated while the maximum and minimum temperature limits are 125 °C and 110 °C respectively

2.3.3. Dynamic performance and start-up strategy

Conditions to be chosen include δ, β, steady-state conversion and temperature, and initial conditions. It is required that steady-state performance, determined by the choice of δ, β and Da, should be located within the desired steady-state temperature range and satisfy the minimum conversion limit, which was investigated in the previous section. On the dynamic side, proper initial conditions should be carefully selected to make sure that corresponding trajectory does not go beyond the maximum allowable temperature (set as 200 °C since Pineda-Solano[68] showed that significant decomposition of the product, i.e. alkylpyridine N-oxide, will be onset above this temperature) on its

journey towards the desired steady state and that the start-up time is reasonable. This point is substantiated by the following case study.
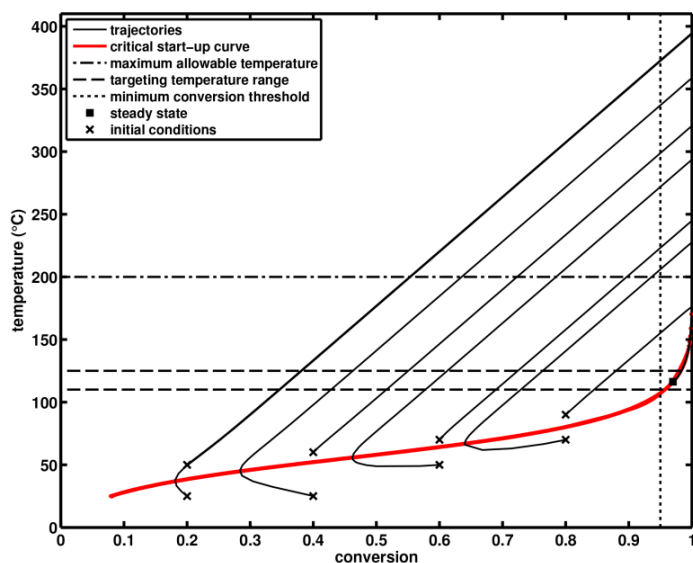
Figure 2.9. Phase plots for different initial conditions at $\delta = 3.9$, $\beta = 54.13$ and $Da = 0.7292$
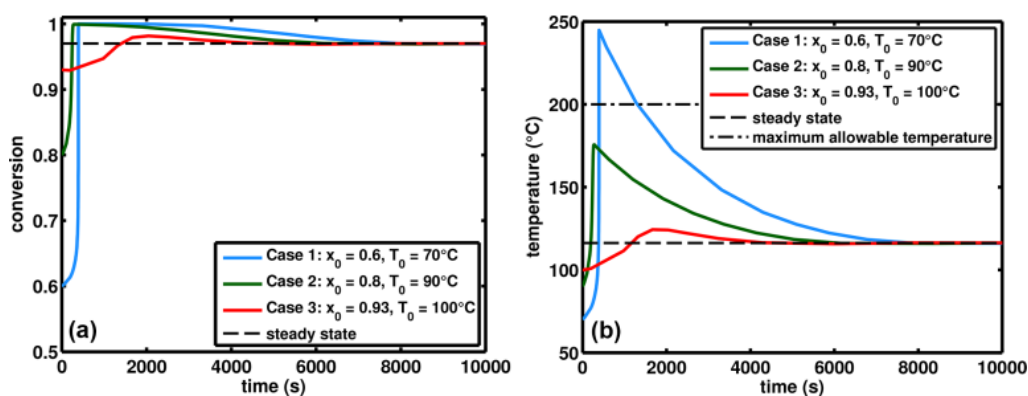
Figure 2.10. Comparison of (a) conversion and (b) temperature time profiles for different start-up scenarios at $\delta = 3.9$, $\beta = 54.13$ and $Da = 0.7292$

48

The point $(\delta, \beta) = (3.9, 54.13)$ belongs to region IVa. For *Da* greater than 0.4077, the system has a single stable steady state with no limit cycles. For instance, when *Da* = 0.7292, phase plots for different initial conditions are displayed in Figure 2.9. All trajectories converge to the same steady state (conversion = 97% and temperature = 116.3 °C) whose production rate is 1.815 ton/L/yr. Practically, say, if 3-picoline is used as the alkylpyridine, such steady state could be achieved by feeding 3-picoline at 3.83 mL/min and 55.9 wt% H_2O_2 (aq) at 2.06 mL/min to the reactor, which gives a concentration of 6.695 mol/L for 3-picoline and a concentration of 7.029 mol/L for hydrogen peroxide in the overall feed flow (5.89 mL/min). Given an initial concentration lower than the feed concentration, there may exist some critical temperature below which reactor concentration first increases to some point and then decreases to its steady-state value. And the lower the initial concentration, the higher the critical temperature. Figure 2.9 shows the critical temperature curve as a function of conversion. It can be seen that trajectories starting from points below the curve first proceed in the direction that both concentration and temperature increase and then turn to the direction that concentration decreases while temperature still increases after intersecting with the critical curve. This is because for low initial concentration and temperature, initial reactant consumption rate is relatively slow and the concentration of alkylpyridine in the reactor keeps rising due to compensation effect by the feed flow until the moment when the consumption rate is equal to the convection rate. Therefore in order to achieve reasonable start-up time, initial conditions should be located above the critical curve. It

49

can also be seen from Figure 2.9 that for current δ and β the critical curve does not exist when initial conversion is lower than 7.91%, which suggests that the consumption rate is always faster than the convection rate regardless of the choice of initial temperature when initial conversion is below 7.91%. However, low initial conversion, or equivalently, high initial concentration, often results in rather large temperature rise and thus should also be avoided. Figure 2.10 compares three start-up cases. Case 1 not only experiences the longest start-up time (about 8000s) but also leads to a temperature peak of 244.8 °C which exceeds the maximum allowable temperature. Case 2 shortens the start-up time to 6000s and the temperature peak is within the allowable limit, while Case 3 further saves one third of the start-up time compared to Case 2 and exhibits a much flatter temperature profile with a maximum temperature deviation of 6.99% from its steady-state value.

2.3.4. Evaluation of the worst-case scenarios

Transient response of a CSTR initially operating at a specific steady state to an immediate and complete loss of cooling capacity was investigated as a viable "worst-case" operating scenario. For each steady state, the time elapsed after cooling fails for the reactor to reach a "point-of-no-return" temperature of 200 °C was obtained ($t_{200°C}$). According to simulation results, the narrow band in region I for both Figure 2.4(a) and 2.4(b) does not lead to such a temperature rise within the simulation time span of 10^5 sec (~2.7 hrs). For the candidate zone in region III and IV for Figure 2.4(b), as shown in Figure 2.11(a) where $t_{200°C}$ for the two boundaries of the candidate zone is displayed in

50

the three dimensional δ-β-$t_{200°C}$ space, the 200 °C threshold is reached in 11.2-33.7 min, which may easily be deemed sufficient for a rapid purging of the current reaction volume of 1 L and provides an important upper limit on reactor scale-up. Figure 2.11(b) and 2.11(c), which are the projections of Figure 2.11(a) onto the δ-$t_{200°C}$ and the β-$t_{200°C}$ planes respectively, suggest that $t_{200°C}$ decreases as δ and β increase. This is because the larger the cooling capacity (δ) and the reaction heat (β), the more urgent the situation is when cooling fails and hence the less the time available for emergency response is. The turnaround of the curve for the lower boundary near $\delta = 4$ and $\beta = 55$ reveals that $t_{200°C}$ is more sensitive to β since β decreases while δ increases near the end of the lower boundary which can be more evidently seen in Figure 2.4(b).

2.3.5. Scale-up

The scalability of the present CSTR analysis is dictated by the ability to estimate both the resulting deviation from perfect mixing and the additional heat transfer capacity needed and to ensure that they are within acceptable and feasible ranges so as not to jeopardize safety, product quality or economics.

Standard practice for scaling up agitated CSTRs is to maintain a constant mean residence time, reactor geometric similarity, and a constant impeller power supply per unit volume (Evangelista et al.[101]; Nauman[102]; Norwood et al.[103]). Based upon this, the literatures[101-103] derived scale-up factors in terms of the volumetric throughput scale-up factor S for geometrically similar CSTRs under assumptions of large Reynolds numbers (larger than 10^4 or preferably 10^5 to achieve turbulent flow regime, which is the case for

most industrial CSTRs) and constant fluid properties, as shown in Table 2.4. Note that

the Reynold number for an agitated CSTR is defined as

$$N_{\mathrm{Re}} = \frac{\overline{\rho} D_I^2 N_I}{\overline{\mu}} \tag{2.6}$$

where D_I and N_I are the diameter and rotation speed of impellers while $\overline{\rho}$ and $\overline{\mu}$ are the

average density and viscosity of reaction mixture.
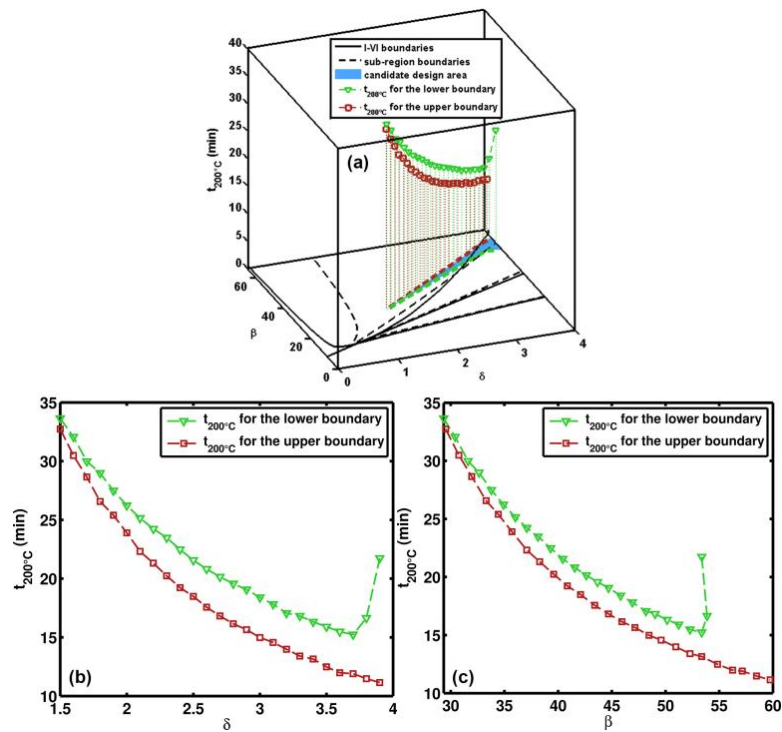
Figure 2.11. Time to 200 °C ($t_{200°C}$) for the candidate design area in Figure 2.4(b): (a) in the δ-β-$t_{200°C}$ space, (b) on the δ-$t_{200°C}$ plane, and (c) on the β-$t_{200°C}$ plane

Table 2.4. Scale-up factors for geometrically similar CSTRs of large Reynolds numbers

	Scale-up factors	Scale-up factors when $S = 1000$
Mean residence time	1	1
Volumetric throughput	S	1000
Tank volume	S	1000
Tank diameter	$S^{1/3}$	10
Impeller diameter	$S^{1/3}$	10
Power per volume	1	1
Power	S	1000
Mixing time	$S^{1/3}$	10
Heat transfer coefficient	$S^{-1/27}$	0.774
Heat transfer area	$S^{2/3}$	100
Impeller rotation speed	$S^{-2/9}$	0.215
Reynolds number	$S^{4/9}$	21.5

Nauman[102] states that the condition for perfect mixing in a CSTR is

$$t_{mix} \ll \bar{\tau} \tag{2.7}$$

i.e. the mean residence time is much longer than the mixing time. For the case in Section 2.3.3, whose Reynolds number is of the order of magnitude of 10^5 (assuming an impeller rotation speed of 500 rpm and an impeller diameter of 4.0 cm), its mixing time is less than 10s according to experimental investigation of flow patterns and mixing rates in agitated vessels reported in Norwood et al.[103] Since the mean residence time is more than two and a half hours, the perfect mixing condition in Eq. (2.7) is satisfied for the case in Section 3.3. If this case is scaled-up by 1000-fold ($S = 1000$) based upon the scale-up

guidelines in Table 2.4, the mixing time will increase by 10-fold and have a value less than 100s, which is still much less than the mean residence time and therefore renders the mixing effect negligible. The heat transfer capacity (heat transfer coefficient multiplied by heat transfer area) of the base case is 0.942 W/K. When the reactor is scaled-up by 1000-fold, it will increase by a factor of $1000^{17/27}$ and have a value of 72.9 W/K, which is achievable in lieu of current state-of-art reactor design and operation techniques as well as some reactor prototypes previously reported.[97,104]

However, it should be noted that although the above reasoning readily provides preliminary evidence of mixing homogeneity and evaluation of heat transfer coefficient for scale-up, more sophisticated tools such as Computational Fluid Dynamics (CFD) modeling are needed to fully understand and ensure mixing patterns within reactors since previous studies like Milewska and Molga[105,106] and Rudniak et al.[107,108] suggest that non-uniformity does exist in stirred tank reactors and it is more evident for industrial-scale ones.

It is also worth mentioning that although crystallization is neglected in the current model (for no such phenomenon was delineated in former experimental investigation,[65-68,73] the impact of crystallization may be significant for several pharmaceutical and fine chemical syntheses, as reviewed by Hartman,[29] and thus warrants mention. Suspended particles arising from undesired in situ crystallization of reaction products would induce more frequent particle-to-particle and particle-to-wall collisions, which at sufficient volume fractions may be expected to have a nontrivial

impact on the effective reaction volume and fluid behaviors via alteration of bulk-fluid viscosity. Likewise, a nonzero dynamic accumulation term in the mass balance and an effective thermal conductivity in the energy balance would be necessary if nucleation and deposition of the crystalline materials on the reactor and tubing surfaces is evident. Lastly, for systems with significant in situ crystallization, clogging of transfer tubing (Hartman[29]; Wyss et al.[109]) could also induce reaction runaway; the addition of statistical models to predict onset of clogging (reviewed by Hartman[29]) would also be required.

2.3.6. Uncertainty analysis

Certain degrees of uncertainty almost always exist in modeling and analysis of chemical processes, which must be taken into account considering that decisions of process design and operation are made therefrom. Although detailed quantification and propagation of uncertainties is not the primary subject of this paper, their sources and impacts will be briefly identified and illustrated here.
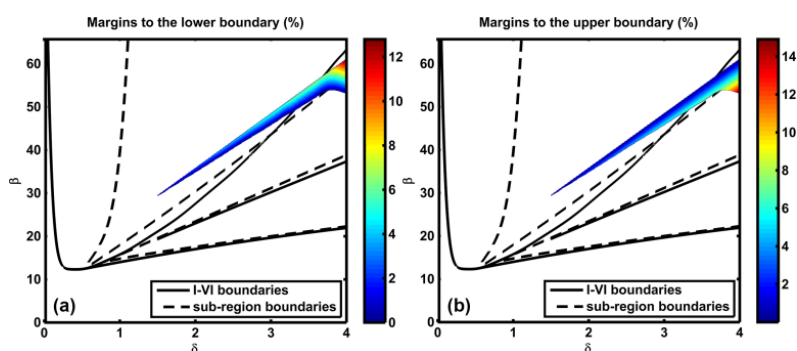
Figure 2.12. Percentage margins of the product of heat of reaction and activation energy for points in the candidate zone in Figure 2.4(b): (a) not to fall below the lower boundary, (b) not to go beyond the upper boundary

55

Heat of reaction and kinetic parameters cited from Papadaki et al.,[67] Pineda-Solano,[68] and Sempere et al.[66] were obtained based upon isothermal calorimetry which calculated concentrations of reactants and products from power profiles. As Hund et al.[110] mentioned, measurement results can deviate from their true values due to any one or a combination of the followings: method bias, time variability, repeatability effect, and reproducibility variance. For the N-oxidation of alkylpyridines, Papadaki et al.[67,111] showed that errors in the measurement of electric calibration power and various temperatures would affect concentrations and consequently heat of reaction and kinetic parameters evaluation. From the definition of δ and β, it can be seen that the product of heat of reaction and activation energy can move the points in the candidate zone vertically along the β-axis. The margins for each point to stay in the candidate zone identified in Figure 2.4(b) without falling below the lower boundary or rising above the upper boundary are displayed in Figure 2.12(a) and 2.12(b), the maximum of which are 12.9% and 14.9% respectively. To reduce the impact of the uncertainties, improved precision of equipment and measuring devices as technology evolves and investigation of correction methods of raw data could be resorted to. It should be also noted that in order to systematically quantify the influence of the uncertainties associated with model parameters on the parameter space demarcation as well as dynamic simulations reported in this paper, the parameters could be described by proper probability distributions instead of point values and the resulting stochastic model equations could be solved by *off-the-shelf* propagation methods such as the Monte-Carlo and the homogenous

polynomial chaos approaches with each having pros and cons against others with respect to applicable scenarios, derivation complexity, computational efforts, and convergence speed.[112] In this way, simulation results would also be given in terms of confidence intervals rather than deterministic single values.

2.4   Conclusions

In this chapter, we have discussed how classical steady-state multiplicity and stability analysis may be employed to generate reactor design and operation parameter-space maps for complex reaction kinetics typical of fine chemicals and pharmaceuticals processing, using the production of alkylpyridine N-oxides as the example. The first-principles CSTR model was established by applying conservation laws and reaction rate expressions from literature. Parameter space was first demarcated based upon steady-state multiplicity, oscillations, and other nonlinear phenomena. It was then evaluated against minimum required conversion as well as minimum and maximum temperatures criteria. Phase-plot analysis of specific operating points satisfying steady-state reactor performance criteria was also performed to guide selection of start-up procedures. In case of a cooling failure, simulation results for the candidate design and operation zone indicate sufficient time is available for emergency response before the reactor temperature exceeds the maximum allowable temperature. Perfect mixing conditions and additional heat transfer load when sizing up the reactor were proved to be applicable and achievable. Safety should be always of paramount concern for any chemical process and

therefore should be made second nature to chemical engineers (Kletz[113]). The study results show very promising performance of the aforementioned analysis tools for aiding in the screening and selection of CSTR designs and start-up protocols for transforming fine chemicals/pharmaceuticals production from batch- to continuous-wise processes without compromising safety or productivity.

CHAPTER III

TUBE-IN-TUBE MEMBRANE REACTOR DESIGN AND OPERATION[*]

3.1   Introduction

The tube-in-tube reactor configuration has received significant recent attention.[20,118-129] Specifically, segregated reactant feeds enter into the shell and the tube sides of an annular assembly comprised of a permeable inner tube and an impermeable outer tube, and contacting of the reactants is controlled by radial permeation through the porous inner tube wall. As summarized in the in-depth review by Mallia and Baxendale,[118] the tube-in-tube reactor concept has been identified as an effective and convenient method to enhance mass transfer, explore alternative reaction conditions, facilitate process scale-up via scale-out or numbering-up, and circumvent hazards associated with flammables and/or corrosives by avoiding direct contact of large volumes of concentrated materials. As evidenced by the numerous examples covered in Ref. (118), the vast majority of the syntheses that have been studied so far based upon the tube-in-tube platform are exclusively gas-liquid reactions (*e.g.*, carbonylation reactions,[123,124] ozonolysis,[125] C-N bond formation using ammonia as reagent,[126,127] and hydrogenation reactions[128,129]) via using the Teflon AF-2400 membrane as the inner tubing which is characteristic of high gas-permselectivity. Specifically, the small

channeled tube-in-tube systems notably facilitate pressurization of reaction mixture without the need for specialized equipment or additional facilities, which not only promotes establishing target gas-liquid stoichiometry and driving reactions to completion owing to increased gas solubility in the liquid media especially at elevated temperatures, but also renders significant economic and safety benefits given that popular reactive gases (*e.g.*, CO, H_2, O_2, O_3, NH_3, Cl_2, C_2H_4, etc.) are often toxic/flammable/corrosive and hence represent substantial hazards that are exacerbated by scale. Besides these gas-liquid cases, applications to liquid-liquid reactions do start to gain momentum (*e.g.*, Buba et al.[121]) owing to progress in "tailoring" transport properties of the Teflon AF-2400 membrane so as to allow selective permeation of certain liquid phase species.[130-132] However, it is noteworthy that since the Teflon AF-2400 membrane is not intended for lasting or harsh heating by design,[122] there lacks studies of permeation performance and material integrity under heating over 80 °C.

Inspired by the motives in switching to continuous processing of pharmaceuticals for process intensification and exploring tubular reactor design featuring radial addition of hydrogen peroxide as envisaged by Pineda-Solano et al.[76] for Scheme 1.1, this chapter demonstrates how appropriate reactor design could help promote inherent safety and improve efficiency for a particular synthetically important but potentially hazardous chemistry by applying the tube-in-tube approach to the liquid-liquid reaction in Scheme 1.1 and presenting an unprecedented detailed system-level analysis of its feasibility and promise. Considering the theoretically zero liquid-permeability of commercial Teflon

AF-2400 membrane without further specialized treatment in addition to the elevated target reaction temperature beyond the upper limit studied so far in literature for material stability over time, porous ceramic membranes such as Al, Si, and Ti oxides are adopted as the inner tube, which have been widely used for catalysis and reaction engineering applications for advantages such as sound pore size uniformity, excellent thermal and mechanical stability, and high resistance to corrosives.[133,134] The regulated slip of hydrogen peroxide into alkylpyridines flow could be implemented by adjusting the positive trans-membrane pressure difference between the peroxide side and the alkylpyridines side. The results provide valuable design criteria for parameters that influence transport, reaction, reactor performance, and scale-up capacity.

3.2   Theoretical – Reactor Model Equations

A one dimensional, steady-state model of a single tube-in-tube unit (Figure 3.1(a)) is developed, assuming hydrogen peroxide enters from the inlet of the tube side, permeates through the porous ceramic membrane, and reacts with the co-currently fed alkylpyridine flow in the annulus. Isothermal condition is assumed to prevail throughout the geometry, such that the present study may focus upon a fundamental understanding of how the performance of the single unit and the multi-unit bundle is manipulated solely via convection and reaction in the annulus as well as mass transport across the membrane which serves as the partitioning media to separate the reactants and allows controlled "titration" of hydrogen peroxide. Similarly, assume that pressure drops in

both the tube and the shell sides are negligible and that a constant cross membrane pressure difference between the two sides is valid given the relatively short single tube length commercially available (0.1 – 1.2 m) which will be employed in the final multi-tube bundle design partly aiming at lessening pressure drops as suggested by Yang and Jensen.[122] Velocity variation of the peroxide flow in the tube side due to localized permeation is assumed to be trivial as flow may be recycled at sufficiently high rates as to offset permeation losses. In addition, the catalyst is assumed to be premixed with the alkylpyridine feed flow whose concentration remains constant throughout the reactor as no evident crystallization involving reactants, catalyst, or product is observed in previous experimental works.[65-68,73]

The resulting "plug-flow" momentum balance for the overall flow and mass balance for peroxide, alkylpyridine, and water respectively in the annulus are described in Eqs. (3.1) – (3.4) by incorporating the rate expression in Eq. (1.4), and the corresponding boundary conditions are set by Eqs. (3.5) – (3.8). Specifically, the flow field is developed by applying Darcy's Law with the fluid permeability (κ^m) in the membrane given by Eq. (3.9) which depends on pore diameter (d^m), porosity (ε^m), and tortuosity (τ^m). The molar flow of peroxide in the annulus is consumed by reaction and supplied by permeation along axial direction while the alkylpyridine flow therein diminishes exclusively via reaction. Note that presence of water in the annulus could be related to alkylpyridine and peroxide flows through reaction and feed stoichiometries

(Eq. (3.4)) assuming that the shell side inflow is neat alkylpyridine with dissolved catalyst (Eq. (3.8)).
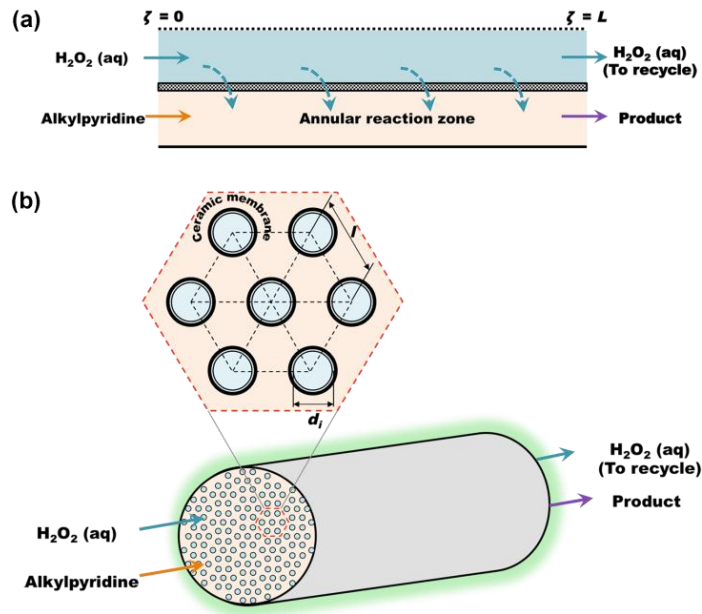
Figure 3.1. (a) Geometry and flow pattern of the single tube-in-tube unit design for the catalytic N-oxidation of alkylpyridines, highlighting controlled slip of hydrogen peroxide via permeation through the inner tube composed of porous ceramic membrane. (b) Tube-in-tube reactor bundle design concept, featuring capability of direct heating/cooling via bundle shell.

$$\frac{dv^s}{d\zeta} = \frac{\kappa^m}{\overline{\mu^t}} \frac{P^t - P^s}{\lambda^m} \alpha^m \qquad (3.1)$$

$$\frac{dF_p^s}{d\zeta} = -r\left(c_a^s, c_p^s, c_z^s, T_{iso}\right)A_c^s + \frac{\kappa^m}{\overline{\mu^t}}\frac{P^t - P^s}{\lambda^m}\alpha^m c_{p,0}^t A_c^s$$

$$= -\left[\frac{k_{1a}(T_{iso})K_b(T_{iso})c_a^s c_p^s c_z^s}{1 + K_b(T_{iso})c_p^s} + k_{1b}(T_{iso})c_a^s c_p^s\right]A_c^s + \frac{\kappa^m}{\overline{\mu^t}}\frac{P^t - P^s}{\lambda^m}\alpha^m c_{p,0}^t A_c^s \qquad (3.2)$$

$$= -\left[\frac{k_{1a}(T_{iso})K_b(T_{iso})\delta c_{a,0}^s}{1 + K_b(T_{iso})\dfrac{F_p^s}{v^s A_c^s}} + k_{1b}(T_{iso})\right]\frac{F_a^s}{v^s A_c^s}\frac{F_p^s}{v^s A_c^s}A_c^s + \frac{\kappa^m}{\overline{\mu^t}}\frac{P^t - P^s}{\lambda^m}\alpha^m c_{p,0}^t A_c^s$$

$$\frac{dF_a^s}{d\zeta} = -r\left(c_a^s, c_p^s, c_z^s, T_{iso}\right)A_c^s = -\left[\frac{k_{1a}(T_{iso})K_b(T_{iso})\delta c_{a,0}^s}{1 + K_b(T_{iso})\dfrac{F_p^s}{v^s A_c^s}} + k_{1b}(T_{iso})\right]\frac{F_a^s}{v^s A_c^s}\frac{F_p^s}{v^s A_c^s}A_c^s \qquad (3.3)$$

$$\frac{dF_w^s}{d\zeta} = r\left(c_a^s, c_p^s, c_z^s, T_{iso}\right)A_c^s + \frac{\kappa^m}{\overline{\mu^t}}\frac{P^t - P^s}{\lambda^m}\alpha^m c_{w,0}^t A_c^s = \varphi\left(\frac{dF_p^s}{d\zeta} - \frac{dF_a^s}{d\zeta}\right) - \frac{dF_a^s}{d\zeta} \qquad (3.4)$$

$$v^s\left(\zeta = 0\right) = v_0^s \qquad (3.5)$$

$$F_p^s\left(\zeta = 0\right) = 0 \qquad (3.6)$$

$$F_a^s\left(\zeta = 0\right) = F_{a,0}^s \qquad (3.7)$$

$$F_w^s\left(\zeta = 0\right) = 0 \qquad (3.8)$$

$$\kappa^m = \frac{\left(d^m\right)^2 \varepsilon^m}{32\tau^m} \qquad (3.9)$$

Table 3.1. Constants in Eqs. (3.10) – (3.13)

Symbols	Units	Values
T_{iso}	K	393.15
$c_{a,0}^{s}$	$mol \cdot L^{-1}$	10.29
$c_{z,0}^{s}$	$mol \cdot L^{-1}$	2.1×10^{-3}
$c_{p,0}^{t}$	$mol \cdot L^{-1}$	17.61
δ	dimensionless	2.04×10^{-4}
θ	dimensionless	1.71

In order to facilitate exploration of parametric design rules dictating performance of the proposed reactor concept, the above dimensional model can be rendered dimensionless (Eqs. (3.10) – (3.16)) by normalizing the dependent variables with respect to inlet conditions of alkylpyridine. Relevant dimensionless variables are summarized in the Nomenclature section and some constants are assigned in Table 3.1. As shown, the isothermal temperature is set at 120 °C in accordance with the temperature window Pineda-Solano et al.[73] identified as being capable of effectively suppressing the competing peroxide decomposition. For illustration purpose, 3-picoline is chosen as an example of the alkylpyridine family, the density of which is $957 \ g \cdot L^{-1}$ (equivalent to a concentration of $10.29 \ mol \cdot L^{-1}$).[114] Catalyst concentration ($c_{z,0}^{s}$) is assumed to be $2.1 \times 10^{-3} \ mol \cdot L^{-1}$ based upon Pineda-Solano et al.[18] which indicated that the amount of catalyst loaded, in the range of $1.7 \times 10^{-3} \ mol \cdot L^{-1}$ to $5.2 \times 10^{-3} \ mol \cdot L^{-1}$ towards the end of dosing period, did not significantly affect reaction progress or performance for

semi-batch operation. Consequently the inlet concentration ratio of catalyst to alkylpyridine (δ) is calculated as 2.04×10^{-4}. 35 wt% H_2O_2 (aq) is used in the current work, the concentration of which is estimated as $17.61 \text{ mol} \cdot \text{L}^{-1}$ based upon a 9th order polynomial correlation[135] between weight fraction and density of peroxide aqueous solution fitted from experimental data provided elsewhere,[114] such that the inlet concentration ratio of peroxide to alkylpyridine (θ) is fixed at 1.71.

$$\frac{d\overline{v^s}}{d\overline{\zeta}} = \frac{H \cdot Da}{\theta} \tag{3.10}$$

$$\frac{d\overline{F_p^s}}{d\overline{\zeta}} = -Da \frac{\text{RXN}\left(v^s, F_a^s, F_p^s\right)}{\text{RXN}\left(v^s, F_{a,0}^s, F_{p,0}^t\right)} + H \cdot Da \tag{3.11}$$

$$\frac{d\overline{F_a^s}}{d\overline{\zeta}} = -Da \frac{\text{RXN}\left(v^s, F_a^s, F_p^s\right)}{\text{RXN}\left(v^s, F_{a,0}^s, F_{p,0}^t\right)} \tag{3.12}$$

where

$$\frac{\text{RXN}\left(v^s, F_a^s, F_p^s\right)}{\text{RXN}\left(v^s, F_{a,0}^s, F_{p,0}^t\right)} = \frac{\dfrac{k_{1a}(T_{iso})K_b(T_{iso})\delta c_{a,0}^s}{1+K_b(T_{iso})c_{a,0}^s \overline{F_p^s}/\overline{v^s}} + k_{1b}(T_{iso})}{\dfrac{k_{1a}(T_{iso})K_b(T_{iso})\delta c_{a,0}^s}{1+K_b(T_{iso})\theta c_{a,0}^s} + k_{1b}(T_{iso})} \frac{1}{\theta}\frac{\overline{F_a^s}}{\overline{v^s}}\frac{\overline{F_p^s}}{\overline{v^s}} \tag{3.13}$$

$$\overline{v^s}\left(\overline{\zeta}=0\right)=1 \tag{3.14}$$

$$\overline{F_p^s}\left(\overline{\zeta}=0\right)=0 \tag{3.15}$$

$$\overline{F_a^s}\left(\overline{\zeta}=0\right)=1 \tag{3.16}$$

The resulting model equations for the single tube-in-tube unit are complete and recast in a form that is ready to evaluate single unit performance and bundle packing strategy for parallelization in terms of two design parameters, namely H and Da, by numerical integration of the differential equations using a pre-packaged marching technique (ode45) encapsulated in the MATLAB$^{\circledR}$ programming environment. As defined in Eq. (3.17), the permeation number (H) is the ratio of permeation to reaction rates and is proportional to the pressure differential driving force for peroxide permeation applied across the membrane. Damköhler number (Da), which is defined in Eq. (3.18) as the ratio of reaction to inlet flow rates, represents a gauge of extent of reaction. Performance metrics are delineated by both alkylpyridine conversion (Eq. (3.19)) and peroxide exit mole fraction ($\overline{F_p^s}(\bar{\zeta} = 1)$) for assessing economics and downstream separation load.

$$H = \frac{\text{Permeation rate}}{\text{Reaction rate}} = \frac{\dfrac{\kappa^m}{\overline{\mu^t}} \dfrac{P^t - P^s}{\lambda^m} \alpha^m c_{p,0}^t}{r_0\left(c_{a,0}^s, c_{p,0}^t, c_{z,0}^s, T_{iso}\right)} \tag{3.17}$$

$$Da = \frac{\text{Reaction rate}}{\text{Flow rate}} = \frac{r_0\left(c_{a,0}^s, c_{p,0}^t, c_{z,0}^s, T_{iso}\right)L}{c_{a,0}^s v_0^s} \tag{3.18}$$

$$x = 1 - \overline{F_a^s}\left(\bar{\zeta} = 1\right) \tag{3.19}$$

3.3   Results and Discussion

3.3.1. Single tube-in-tube unit design

The isothermal membrane reactor model described by Eqs. (3.10) – (3.16) was employed to predict influence of Da and H upon performance of the single tube-in-tube unit. Specifically, Da was varied from 10^{-3} to 10^{5} at values of H across the range (10^{-5}, 10^{-4}, 10^{-3}, 10^{-2}, 10^{-1}, 1, 10, 20). Performance is shown in Figure 3.2(a) and 3.2(b) respectively. In general, increasing Da at constant H leads to higher conversion but greater peroxide content in the alkylpyridine N-oxide production stream as the time for both reaction and H_2O_2 addition increases. For $H < 1$, which represents the permeation-limited scenario, conversion increases with H at fixed Da owing to an increase in H_2O_2 supply to the annulus, which is instantaneously reacted with alkylpyridine. Conversely, for $H > 1$ (reaction-limited case), conversion increases with decreasing H at constant Da as relative rate of reaction increases. Figure 3.2 indicates that operation under reaction-limited conditions ($H > 1$) is unfavorable as residence times (Da) required to achieve high conversion also correspond to substantial accumulation of H_2O_2 in the product stream. Operation under permeation-limited conditions ($H < 1$) is capable of achieving significant per-pass conversions while keeping H_2O_2 in the product stream at a minimum, albeit at the cost of larger reactor volumes. Hence, $H < 1$ is considered as the favorable design basis wherein increasing H improves productivity. However, more H_2O_2 may be present both locally and at the annulus exit for larger H, as evidenced by Figure 3.2(b), which not only poses safety concerns of peroxide accumulation but also

exerts heavier downstream separation load. Therefore, there exists a trade-off between efficiency and purity dictated by an appropriate combination of *Da* and *H*.
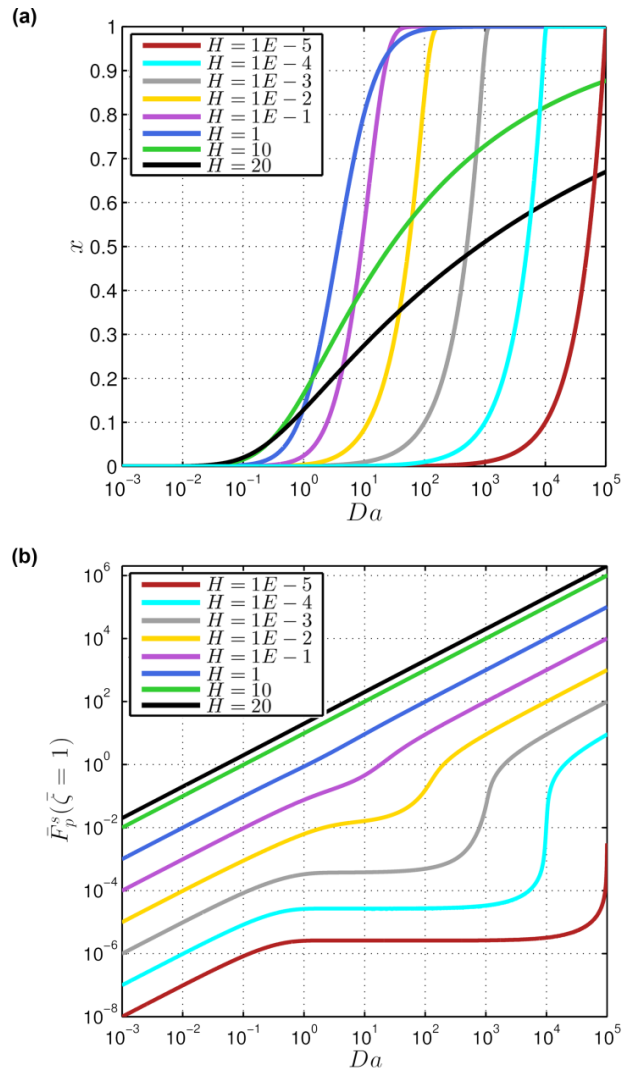
Figure 3.2. Dependence of (a) alkylpyridine conversion and (b) peroxide exit molar flow rate on Damköhler number (*Da*) and permeation number (*H*).
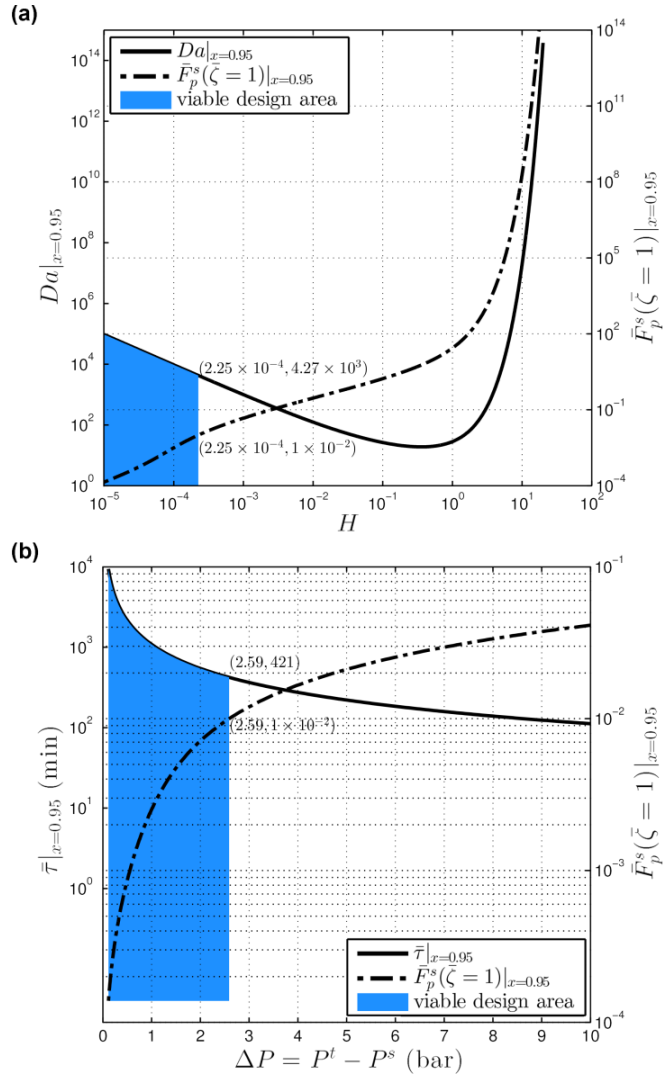
Figure 3.3. (a) Dependence of *Da* required to achieve 95% conversion as well as corresponding peroxide exit flow rate on *H*. (b) Re-scale of (a) in terms of mean residence time and trans-membrane pressure difference by employing model constants in Table 3.1 and material properties in Table 3.2 according to Eqs. (3.17) and (3.20).

This tradeoff is illustrated in Figure 3.3 which presents the *Da* corresponding to

95% outlet conversion with resulting peroxide outlet flowrate as a function of *H* (Figure

3.3(a)). This information is translated into mean residence time and cross-membrane

pressure difference assuming an α-Al$_2$O$_3$ tube (inopor® GmbH) with properties and dimensions summarized in Table 3.2. Note that the pressure difference is calculated from Eq. (3.17), the scale of which is truncated at 10 bar in Figure 3.3(b), consistent with feasible operation limits for porous ceramic membrane; the mean residence time is obtained from the integral of the velocity profile in the shell side as shown in Eq. (3.20). Given the significant product purity and safety concerns associated with H$_2$O$_2$ in alkylpyridine N-oxide product, a viable design area is identified based upon a maximum tolerable peroxide outlet composition ($\overline{F_p^s}(\bar{\zeta} = 1)$) of 10^{-2} (i.e., < 1 mol% H$_2$O$_2$).[68,73,76] This criterion defines a maximum H of 2.25×10^{-4}, or equivalently a maximum pressure differential of 2.59 bar, at which the corresponding mean residence time is 421 min.

$$\bar{\tau}\big|_{x=0.95} = \frac{Da\big|_{x=0.95} \, c_{a,0}^s}{r_0\left(c_{a,0}^s, c_{p,0}^t, c_{z,0}^s, T_{iso}\right)\int_0^1 \overline{v^s} d\bar{\zeta}} \tag{3.20}$$

3.3.2. Bundle design for scale-up

The above design rules are extended to studying module development strategy for scale-up purpose. As discussed in the Introduction section, one of the primary advantages of the ceramic tube-in-tube reactor concept is ease of scale-up by incorporating multiple parallel tubes into a single shell. We assume a hexagonally-packed bundle of tubes with hydrogen peroxide supplied to the bore-side, while a single alkylpyridine flow is supplied through the annular tube (Figure 3.1(b)). If thermal effects and radial mass transfer resistance within each unit are sufficiently small, then interaction between single units may be neglected and performance of these units may be

71

assumed to be identical. With these assumptions, the designs identified in Figure 3.2 and 3.3 may be employed to study the total number of tubes in the bundle and bundle dimensions as determined by target production rate, individual tube dimensions, and packing distance.

Table 3.2. Typical material properties and tube dimensions for commercially available porous ceramic membrane tubes

Symbols	Units	Values
d^m	nm	$800^†$
τ^m	dimensionless	3
ε^m	dimensionless	$0.55^†$
κ^m	m^2	$\dfrac{(d^m)^2 \varepsilon^m}{32\tau^m} = 3.67 \times 10^{-15}$
α^m	m	$0.024^†$
Tube I.D. (d_i)	mm	$7^†$
Tube O.D. (d_o)	mm	$10^†$
λ^m	mm	$\dfrac{d_o - d_i}{2} = 1.5$
L	m	$0.1 - 1.2^†$

†Values cited from Ref. (136)

This is illustrated by the following case study using the point $H = 2.25 \times 10^{-4}$ and $Da|_{x\,=\,0.95} = 4.27 \times 10^3$ labeled in Figure 3.3(a). The dependence of the number of tubes

and bundle diameter on productivity requirement, single unit dimensions, and packing distance are derived in Eqs. (3.21) and (3.22). Since commercial information such as trading volume and price for alkylpyridine N-oxides is normally proprietary, production rate specification in this study is presumed to claim a value of 1, 5, 10 ton/yr as alkylpyridine N-oxides are classified as specialty compounds whose consumption is lower than commodity chemicals.[10,11] As presented in Figure 3.4(a) and 3.4(b), where the single tube inner and outer diameters are set as 7 mm and 10 mm respectively and the tube length 1.0 m or 0.7 m according to Table 3.2, increasing the ratio of center-to-center packing distance (l) to single tube inner diameter (d_i) generally facilitates implementation of fewer tubes and smaller bundle size for a given combination of production rate and tube length since larger l/d_i provides more reaction volume. However, this does not necessarily mean that l/d_i should be raised until the threshold value resulting in unity for the number of tubes is reached because negligibility of radial mass transfer resistance and assumption of radial mixing homogeneity within the unit would be disputable for large annulus gaps. In fact, Figure 3.4(c) reveals that the single unit aspect ratio, which is defined by Eq. (3.23), experiences a drastic drop with increasing l/d_i especially around the value of 2. Hence the aspect ratio, which is normally above 30 for homogenously operated tubular reactors,[137] must be considered in addition to the number of tubes and bundle diameter in selection of appropriate l/d_i. Figure 3.4(c) reads that the threshold values of the packing distance to ensure a single unit aspect ratio greater than 30 for the cases of $L = 1.0$ m and $L = 0.7$ m are $6.2d_i$ and $4.7d_i$ respectively.

73

The results for $l/d_i = 3$ and $l/d_i = 2$, both leading to a single unit aspect ratio exceeding 30 for either reactor length, are summarized and compared in Table 3.3. In comparison with bundle diameter, the number of tubes is far more sensitive to the change of l/d_i at fixed reactor length and production rate, which is also evident from the consistently steeper declining slope for curves in Figure 3.4(a) than those in Figure 3.4(b) throughout the entire spectrum of l/d_i. In other words, when l/d_i is raised, the benefit achieved for lowering the number of tubes needed vastly outruns that for bundle diameter reduction. For instance, increasing l/d_i from 2 to 3 at constant reactor length of 1.0 m and production rate of 10 ton/yr induces a prominent reduction in the number of tubes from 128 to 38 (70.3%), which is nearly three-fold more significant in terms of percentage change than the reduction in the bundle diameter from 0.166 m to 0.137 m (17.4%).

$$\text{Number of tubes} = \frac{1}{2} \frac{\text{Production rate}}{\text{Reaction area} \times MW_N v_0^s c_{a,0}^s \overline{F_a^s}(\zeta = 1)}$$

$$\text{where } v_0^s = \frac{r_0\left(c_{a,0}^s, c_{p,0}^t, c_{z,0}^s, T_{iso}\right)L}{Da|_{x=0.95}\, c_{a,0}^s} \text{ and Reaction area} = \frac{\sqrt{3}}{4}l^2 - \frac{\pi}{8}d_o^2 \tag{3.21}$$

$$\text{Bundle diameter } D = \frac{\text{Number of tubes} \times 2\sqrt{3}l^2}{\pi} \tag{3.22}$$

$$\text{Single unit aspect ratio} = \frac{L}{l - d_o} \tag{3.23}$$
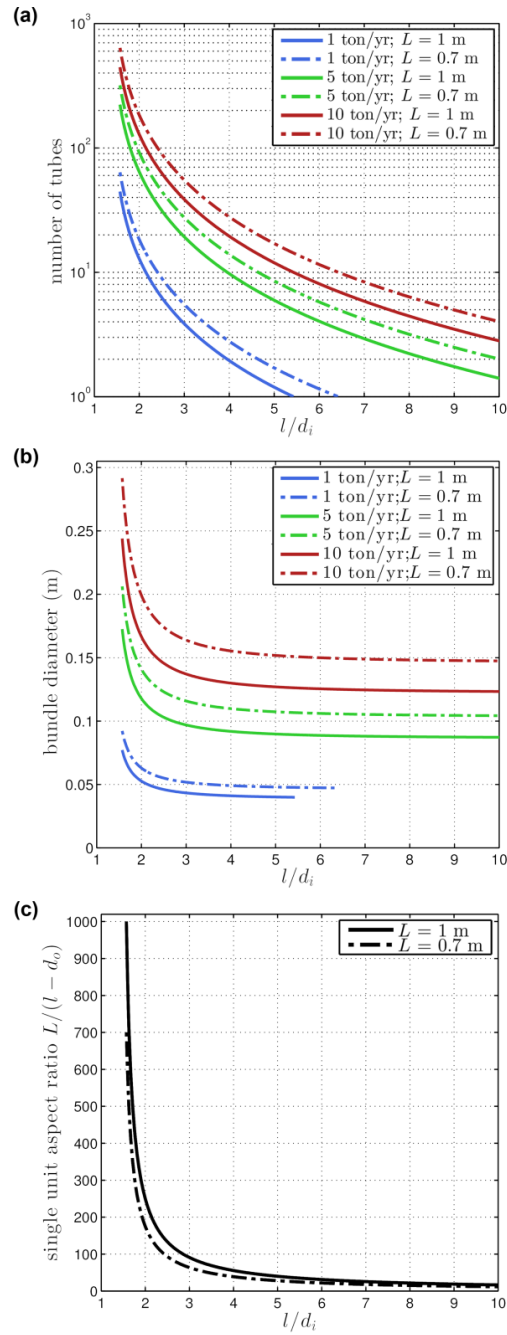
Figure 3.4. Predicted influence of varying the ratio (l/d_i) of center-to-center distance between adjacent tubes to tube inner diameter on (a) the number of tubes, (b) bundle diameter, and (c) single unit aspect ratio based upon the point $H = 2.25 \times 10^{-4}$ and $Da|_{x = 0.95} = 4.27 \times 10^{3}$ labeled in Figure 3.3(a) and identified as viable in the single unit design analysis.

Table 3.3. Evaluation of module design parameters for $l/d_i = 2$ and $l/d_i = 3$ as well as for specific reactor length (1.0 and 0.7 m) and production rate (1, 5, and 10 ton/yr) based on $H = 2.25 \times 10^{-4}$ and $Da|_{x=0.95} = 4.27 \times 10^3$

Packing distance[†] l/d_i	Reactor length L (m)	Single unit aspect ratio[†] $L/(l - d_o)$	Production rate (ton/yr)	Number of tubes	Bundle diameter (m)
2	1.0	250.0	1	12	0.053
			5	64	0.118
			10	128	0.166
	0.7	175.0	1	18	0.063
			5	91	0.141
			10	183	0.199
3	1.0	90.9	1	4	0.043
			5	19	0.097
			10	38	0.137
	0.7	63.6	1	6	0.052
			5	27	0.115
			10	55	0.163

[†]d_i and d_o claim a value of 7 mm and 10 mm respectively according to Table 3.2

3.3.2.1.   *Evaluation of thermal duty*

Thermal duty is analyzed to justify the validity of the isothermal assumption. Since the tube-in-tube bundle prototype allows direct cooling via the external shell, heat flux ($\dot{q}$) from the reaction volume to the shell is estimated based upon the axially-varying reaction heat generation rate (Eq. (3.24), assuming a constant heat of reaction of $160 \ kJ \cdot mol^{-1}$ based upon previous experimental investigation[65-68,73]). A reference heat

transfer coefficient (h_{ref}) is obtained by dividing the heat flux by temperature difference between the reaction mixture and the heat transfer fluid employed (Eq. (3.25)). The underlying assumptions for Eqs. (3.24) and (3.25) are that (i) heat removal is attained solely via dissipation to the shell without thermal interaction with inner ceramic tubes or hydrogen peroxide feed flows therein, and that (ii) infinite heat conductivities for the reaction mixture and the solid shell as well as instantaneous thermal equilibrium between the shell and the heat transfer fluid are valid. Actual heat transfer coefficient (h), which depends on fluid properties, module dimensions, and operation conditions, is calculated from a correlation[138] (Eq. (3.26)) of three dimensionless groups, namely Nusselt number (N_{Nu}), Reynolds number (N_{Re}), and Prandtl number (N_{Pr}). Since Geankoplis[138] comments that the correlation holds for $\left(N_{\mathrm{Re}}N_{\mathrm{Pr}}\frac{D}{L}\right) > 100$ and that it still does to $\pm 20\%$ for $\left(N_{\mathrm{Re}}N_{\mathrm{Pr}}\frac{D}{L}\right) > 10$, the heat transfer coefficient obtained from Eq. (3.26) is further multiplied by a factor of 0.8 to account for such uncertainty as the quantity $\left(N_{\mathrm{Re}}N_{\mathrm{Pr}}\frac{D}{L}\right)$ is estimated to range from 12 to 20 for those scenarios considered in Figure 3.4.

$$\dot{q} = \frac{\left(-\Delta H_{rxn}\right)A_c^s \int_0^L r\left(c_a^s, c_p^s, c_z^s, T_{iso}\right)d\zeta \times \text{Number of tubes}}{\pi D} \tag{3.24}$$

$$h_{ref} = \frac{\dot{q}}{T_{iso} - T_c} \tag{3.25}$$
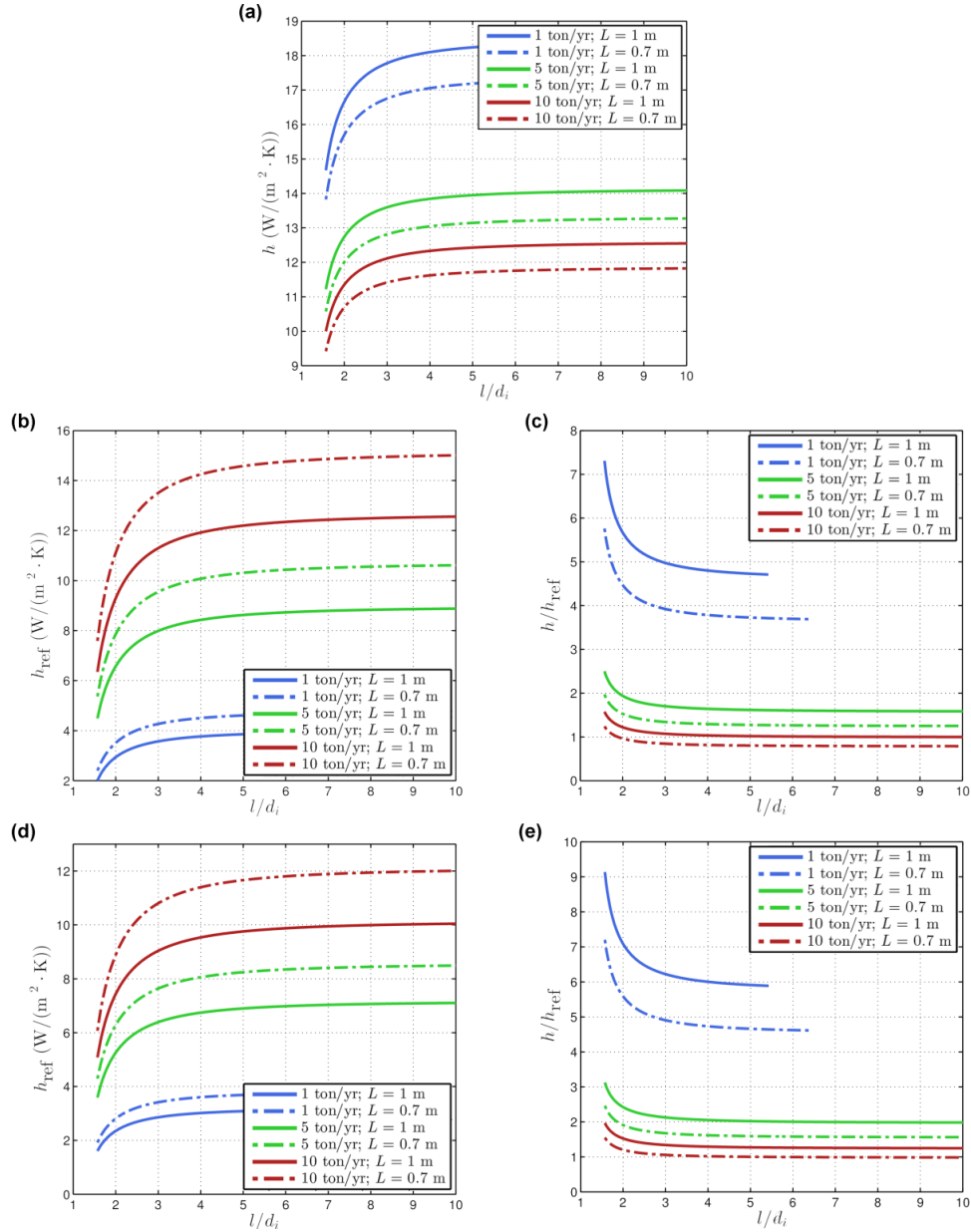
Figure 3.5. Thermal evaluation corresponding to Figure 3.4. (a) Actual heat transfer coefficient calculated from Eq. (3.26), assuming $\overline{C_p^s} = 4184\,\mathrm{J \cdot kg^{-1} \cdot K^{-1}}$, $\overline{k^s} = 0.68\,\mathrm{W \cdot m^{-1} \cdot K^{-1}}$, $\overline{\rho^s} = 1000\,\mathrm{kg \cdot m^{-3}}$, and $\overline{\mu^s} = 0.001\,\mathrm{Pa \cdot s}$. (b) and (d) The lower bound of heat transfer coefficient required to justify feasibility of implementing the isothermal assumption at $T_c = 4\,°C$ and $T_c = -25\,°C$ respectively. (c) and (e) The ratio of the actual heat transfer coefficient in (a) to the lower bound in (b) and (d) respectively.

78

$$N_{\text{Nu}} = \frac{hD}{k^s} = 1.86\left(N_{\text{Re}}N_{\text{Pr}}\frac{D}{L}\right)^{1/3}$$

$$\text{where } N_{\text{Re}} = \frac{Dv^s\overline{\rho^s}}{\overline{\mu^s}} \text{ and } N_{\text{Pr}} = \frac{\overline{C_p^s\,\mu^s}}{\overline{k^s}} \tag{3.26}$$

Inspection of Eq. (3.26) suggests that the actual heat transfer coefficient is inversely proportional to the product of bundle diameter and reactor length (DL) and is more sensitive to D, as also evidenced in Figure 3.5(a) where curves located relatively higher feature smaller bundle diameter (cf. Figure 3.4(b)), though the "superiority" has been offset to some extent by greater length. On the other hand, the reference heat transfer coefficient, which essentially sets the lower bound that the actual heat transfer coefficient needs to achieve in order to provide preliminary justification of feasibility for practically realizing the isothermal assumption, should be lower from intuition for larger bundle diameter cases due to more heat transfer area available. However, Figure 3.5(b) and 3.5(d) show that the significantly rising number of tubes needed in accordance with larger bundle diameter (Figure 3.4(a) and 3.4(b)) increases the heat flux and consequently leads to higher reference heat transfer coefficients. Apart from the heat flux, the coolant temperature also influences the reference heat transfer coefficient. The colder the coolant, or equivalently, the greater the driving force resulting from larger temperature difference, the lower the coefficient, referring to the comparison between Figure 3.5(b) and 3.5(d) where $T_c = 4\ ^\circ\text{C}$ and $T_c = -25\ ^\circ\text{C}$ respectively. Furthermore, as compared in Figure 3.5(c) and 3.5(e), the lower coolant temperature also helps promote the ratio of the actual heat transfer coefficient to the corresponding reference one, which

should be greater than unity in order to advocate viability of the isothermal condition. For the case of productivity = 10 ton/yr and L = 0.7 m (dashed red curves in Figure 3.5(c) and 3.5(e)), the ratio h/h_{ref} falls below one once l/d_i exceeds 1.9 with the cooling temperature set as 4 °C, whereas it keeps staying above unity for l/d_i at least up to 10 with the cooling temperature switching to -25 °C which could be accomplished by using ethylene or propylene glycol-based fluids commercially available.

3.3.2.2.   *Evaluation of mass transfer across unit boundary*

Besides feasibility of achieving isothermal operation, the other assumption claimed in bundle design, i.e. negligible radial mass interaction among single units, needs to be validated. The radial Peclet number for single unit is evaluated, which, as shown by Eq. (3.27), represents the ratio of characteristic time for radial diffusion to that for convective transport in the annulus. According to Wilke and Chang[139], the diffusivity of alkylpyridine in water ($D_{a,w}^s$) appearing in Eq. (3.27) is calculated from a correlation given by Eq. (3.28), which depends on solvent association parameter (2.6 for water), solution viscosity ($\overline{\mu^s}$), and solute molecular volume at normal boiling point (V_a) as well as solute molecular weight (MW_a) with V_a estimated based upon atomic contributions (15 for pyridine ring, 14.8 for carbon, and 3.7 for hydrogen). Inspection of Eqs. (3.27) and (3.21) reveals that the radial Peclet number is linearly proportional to the packing distance at constant tube length as it fixes the convection velocity and that increasing tube length leads to larger Peclet number as convection is expedited. This is backed by Figure 3.6 in accordance with those bundle design cases in Figure 3.4, which indicates

that the minimum packing distance for achieving sufficiently large Peclet number ($N_{\text{Pe}_r} >$ 100) is $4.3d_i$ and $5.6d_i$ respectively for the two tube lengths evaluated.

$$N_{\text{Pe}_r} = \frac{v_0^s \int_0^1 \overline{v^s} d\overline{\zeta} \left(\frac{\sqrt{3}}{3} l - \frac{1}{2} d_o \right)}{D_{a,w}^s} \tag{3.27}$$

$$D_{a,w}^s = 7.4 \times 10^{-12} \frac{(\text{Association parameter} \times MW_a)^{0.5} T_{iso}}{\overline{\mu^s} V_a^{0.6}} = 7.4 \times 10^{-12} \frac{(2.6 MW_a)^{0.5} T_{iso}}{\overline{\mu^s} V_a^{0.6}}$$

$$= 4.88 \times 10^{-5} \text{ cm}^2/\text{s} \tag{3.28}$$

where $V_a = 15 + 14.8 + 3.7 \times 3 = 33.5$
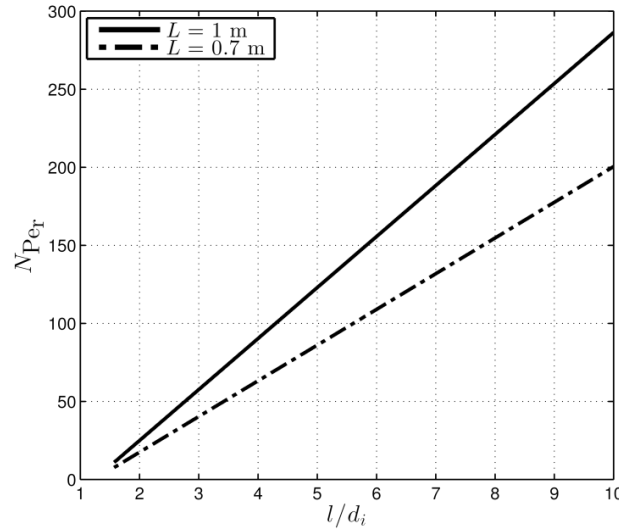
Figure 3.6. Radial Peclet number calculated from Eqs. (3.27) and (3.28) for cases in Figure 3.4, assuming $MW_a = 93.13 \text{ g} \cdot \text{mol}^{-1}$ and $\overline{\mu^s} = 0.001 \text{ Pa} \cdot \text{s}$.

It is also worth mentioning that although phase separation within reaction mixture is not considered in the present study, such phenomenon may be nontrivial for

N-oxidation of other compounds in the pyridine family such as dimethylpyridines and trimethylpyridines, which would ultimately impact process efficiency and environmental footprint of the continuous reactor configuration. For such cases, more fundamental understanding of mass transport limitation associated with the thin film between aqueous and organic bulks is warranted, particularly in relation to the resulting Environmental factor (E-factor, defined as mass of waste per mass of product formed[140]) and mitigation strategies as studied by Hu et al.[141] and Sabio et al.[142]

3.3.2.3. Final design scheme

Combining the findings in the previous sections, a reactor bundle design based upon single tubes of 7 mm (I.D.) and 10 mm (O.D.) is finalized in Table 3.4. It's impossible to select an appropriate packing distance when reactor length is 0.7 m as radial mixing homogeneity within individual unit requires the packing distance be less than $4.7d_i$ while circumvention of mass interaction among units mandates a minimum packing distance of $5.6d_i$. For this reason, the reactor length is set as 1.0 m, under which circumstance the packing distance should be within the range of $4.3d_i$ and $6.2d_i$. As evident from Table 3.4, larger packing distance favors validity of mass isolation among units (i.e. larger N_{Pe_r}) and reduction in the number of tubes and associated tube costs for the same production rate target. However, the homogeneous radial mixing condition within each unit shows some degree of deterioration (i.e. smaller single unit aspect ratio) with increasing packing distance, while the bundle diameter and the heat removal efficiency are relatively insensitive to it.

Table 3.4. Final module design based upon $H = 2.25 \times 10^{-4}$ and $Da|_{x=0.95} = 4.27 \times 10^{3}$ (reactor length $L = 1.0$ m)

Packing distance[†] l/d_i	Single unit aspect ratio[†] $L/(l - d_o)$	N_{Pe_r}	Production rate (ton/yr)	Number of tubes	Bundle diameter (m)	Total reaction volume (L)	h / h_{ref}		CapEX for membrane tubes (USD)[‡]
							$T_c = 4\ °C$	$T_c = -25\ °C$	
5	40	122.9	1	2	0.0402	1.17	4.73	5.91	268
			5	6	0.0898	5.86	1.62	2.02	804
			10	12	0.127	11.7	1.02	1.27	1,608
6	31.3	155.6	1[*]	n/a	n/a	n/a	n/a	n/a	n/a
			5	4	0.0887	5.86	1.60	2.01	536
			10	8	0.126	11.7	1.01	1.26	1,072

[†]d_i and d_o claim a value of 7 mm and 10 mm respectively according to Table 3.2
[‡]CapEX (capital expenditure) is calculated based upon a single tube price of 121 EUR[136]
[*]Design scheme for a production rate of 1 ton/yr at a packing distance of $6d_i$ is not applicable according to Figure 3.4 and 3.5

3.4 Conclusions

This chapter proves the viability and promise of tube-in-tube non-catalytic membrane reactors, previously applied with success to gas-liquid reactions, to promote continuous handling of the liquid-liquid catalytic N-oxidation of alkylpyridines. Simulation results demonstrate that porous ceramic membranes of outstanding thermal, mechanical, and corrosive resistances can be employed to isolate concentrated hazardous reactants and regulate addition of hydrogen peroxide into alkylpyridines via permeation. The permeation-limited condition ($H < 1$) offer the feasibility to achieve both satisfactory alkylpyridine conversion and peroxide residue upon appropriate selection of Damköhler number, and therefore is preferable over the reaction-limited condition ($H > 1$). To implement scale-up of capacity by parallelizing multiple membrane tubes of fixed length, bundle dimensions and mass/heat transfer efficiency depend on packing distance between adjacent tubes. Increasing the packing distance has a more significant effect on reducing the number of tubes in the bundle than the bundle diameter. The lower limit of the packing distance is determined by validity of mass isolation among tube units, while the upper limit is dictated by mixing homogeneity within tube units and feasibility to maintain isothermal operation. Case studies reveal that a packing distance of $4.3d_i - 6.2d_i$ is capable of achieving an annual production rate of $1 - 10$ ton alkylpyridine N-oxide given a reactor length of 1.0 m.

CHAPTER IV

SUMMARY AND RECOMMENDATIONS

Two continuous reactor designs, both a jacketed continuous-stirred tank reactor (CSTR) and a segregated-feed membrane reactor design, were investigated to overcome inherent challenges with synthetically important yet potentially hazardous chemistry using the liquid phase, homogeneous catalytic exothermic N-oxidation of alkylpyridines as an illustrating example, whose substantial safety concerns render scale-up of capacity cumbersome for current semi-batch practice.

For the CSTR design (Chapter II), a first-principles dynamic model was established by applying conservation laws and reaction kinetics. Practically tunable reactor parameters were subsequently defined and design rules in terms of these parameters were determined by manipulating the reactor model according to bifurcation theory which dictates nonlinear phenomena such as steady-state multiplicity, oscillation, and stability. The design rules also took account of performance criteria, including conversion and desired temperature window, so as to avoid compromising productivity while preventing runaway. In addition to aiding screening and selection of design parameters, the dynamic model readily allows addressing practical concerns for reactor operation. For instance, phase-plot analysis was performed to illustrate significance of appropriate start-up protocols for the sake of safety and efficiency. Step response testing was conducted to evaluate potential consequences and system reliability when nominal

conditions were interrupted, which could lend valuable reference to emergency response and risk management protocols. Lastly, scale-up feasibility was proved based upon empirical scaling laws in literature to ensure adequate mixing and heat transfer.

For the membrane reactor design (Chapter III), a tube-in-tube configuration was adopted, which features use of an inner non-catalytic membrane tube to isolate concentrated reactant flows and regulate addition of one reactant into the other via permeation so that accumulation of the permeating species or dangerous concentration ratio between the reactants in the reaction channel (the annulus in the current study) is avoided and that the transformation is steered towards desired product. A one-dimensional, isothermal model of the tube-in-tube reactor accounting for mass and momentum conservation laws and reaction kinetics was first established. Then design rules in terms of permeation and reaction intensities were given in order to achieve desired alkylpyridine conversion while minimizing exit peroxide molar fraction. Based upon the design rules obtained from the single tube-in-tube reactor unit along with typical material properties for commercially available porous ceramic membranes, multi-tube bundle design was explored for scale-up with a focus upon the influence of packing distance between adjacent tubes on bundle dimensions as well as validity of the isothermal and the mass isolation assumptions.

Future development of the present work could be elaborated in the following aspects.

For the CSTR design, we are interested in exploring experimental validation of forecast steady-state and transient behaviors. New experimental phenomena may in turn contribute to theoretical developments. In the meantime, since dynamic simulation allows effective investigation of potential consequences when nominal conditions are interrupted and rapid evaluation of possible measures to mitigate the consequences, it could be integrated with conventional risk assessment methods such as HAZOP, FMEA, and LOPA to help identify major risk factors in the process and therefore to facilitate inherently safer design of it.

For the membrane reactor design, establishing a non-isothermal model could be pursued to gain deeper insight into the effect of transport-reaction interaction on reactor performance. The non-isothermal model would also allow exploration of adiabatic operation possibilities for the sake of energy saving. Meanwhile, detailed two-dimensional CFD simulation could be performed to serve as *in silico* validation of the one-dimensional model which is more appropriate for on-line control and optimization purposes.

REFERENCES

(1)   Daemmrich, A.A. US healthcare reform and the pharmaceutical industry. *Harvard Business School Working Paper*. **2011**.

        http://www.hbs.edu/faculty/Publication%20Files/12-015.pdf (accessed July 27, 2016)

(2)   Cohen, R.A.; Martinez, M.E.; Zammitti, E.P. Early release of selected estimates based on data from the 2015 National Health Interview Survey. *National Center for Health Statistics*. **2015**.

        http://www.cdc.gov/nchs/nhis/releases/released201605.htm (accessed July 27, 2016)

(3)   Deloitte. 2015 Global life sciences outlook: adapting in an era of transformation. **2015**.

        https://www2.deloitte.com/content/dam/Deloitte/global/Documents/Life-Sciences-Health-Care/gx-lshc-2015-life-sciences-report.pdf (accessed July 27, 2016)

(4)   U.S. Food and Drug Administration. *Pharmaceutical CGMPs for the 21st Century – A Risk-Based Approach*. Rockville, MD, **2004**.

        https://www.fda.gov/downloads/drugs/developmentapprovalprocess/manufacturing/questionsandanswersoncurrentgoodmanufacturingpracticescgmpfordrugs/ucm176374.pdf (accessed July 27, 2016)

(5) U.S. Food and Drug Administration. *Guidance for Industry PAT – A Framework for Innovative Pharmaceutical Development, Manufacturing, and Quality Assurance*. Rockville, MD, **2004**. https://www.fda.gov/downloads/drugs/guidances/ucm070305.pdf (accessed July 27, 2016)

(6) Adamo, A.; Beingessner, R.L.; Behnam, M.; Chen, J.; Jamison, T.F.; Jensen, K.F.; Monbaliu, J.C.M.; Myerson, A.S.; Revalor, E.M.; Snead, D.R.; Stelzer, T. On-demand continuous-flow production of pharmaceuticals in a compact, reconfigurable system. *Sci*. **2016**, *352(6281)*, 61-67.

(7) Anderson, N.G. Practical use of continuous processing in developing and scaling up laboratory processes. *Org. Process Res. Dev.* **2001**, *5(6)*, 613-621.

(8) Badman, C.; Trout, B.L. Achieving continuous manufacturing. *J. Pharm. Sci.* **2015**, *104(3)*, 779-780.

(9) Baxendale, I.R.; Braatz, R.D.; Hodnett, B.K.; Jensen, K.F.; Johnson, M.D.; Sharratt, P.; Sherlock, J.P.; Florence, A.J. Achieving continuous manufacturing: technologies and approaches for synthesis, workup, and isolation of drug substance. May 20 – 21, 2014 Continuous Manufacturing Symposium. *J. Pharm. Sci.* **2015**, *104(3)*, 781-791.

(10) Calabrese, G.S.; Pissavini, S. From batch to continuous flow processing in chemicals manufacturing. *AIChE J.* **2011**, *57(4)*, 828-834.

(11)   Hartman, R.L.; McMullen, J.P.; Jensen, K.F. Deciding whether to go with the flow: Evaluating the merits of flow reactors for synthesis. *Angew. Chemie - Int. Ed.* **2011**, *50(33)*, 7502-7519.

(12)   Mascia, S.; Heider, P.L.; Zhang, H.; Lakerveld, R.; Benyahia, B.; Barton, P.I.; Braatz, R.D.; Cooney, C.L.; Evans, J.M.B.; Jamison, T.F.; Jensen, K.F.; Myerson, A.S.; Trout, B.L. End-to-end continuous manufacturing of pharmaceuticals: integrated synthesis, purification, and final dosage formation. *Angew. Chemie - Int. Ed.* **2013**, *52(47)*, 12359-12363.

(13)   Poechlauer, P.; Colberg, J.; Fisher, E.; Jansen, M.; Johnson, M.D.; Koenig, S.G.; Lawler, M.; Laporte, T.; Manley, J.; Martin, B.; O'Kearney-McMullan, A. Pharmaceutical roundtable study demonstrates the value of continuous manufacturing in the design of greener processes. *Org. Process Res. Dev.* **2013**, *17(12)*, 1472-1478.

(14)   Valera, F.E.; Quaranta, M.; Moran, A.; Blacker, J.; Armstrong, A.; Cabral, J.T.; Blackmond, D.G. The flow's the thing…or is it? Assessing the merits of homogeneous reactions in flask and flow. *Angew. Chemie - Int. Ed.* **2010**, *49(14)*, 2478-2485.

(15)   Mollan Jr, M.J.; Lodaya, M. Continuous processing in pharmaceutical manufacturing. *Pharm. Manuf. Magn.* **2004**, 1-9.

(16)   Lakerveld, R.; Benyahia, B.; Braatz, R.D.; Barton, P.I. Model‑based design of a plant‑wide control strategy for a continuous pharmaceutical plant. *AIChE J.* **2013**, *59(10)*, 3671-3685.

(17)   Baumann, M.; Baxendale, I.R. The synthesis of active pharmaceutical ingredients (APIs) using continuous flow chemistry. *Beilstein J. Org. Chem.* **2015**, *11*, 1194-1219.

(18)   O'Brien, M.K. Portable, continuous, miniature, & modular (PCM&M) development and manufacturing: the foundation for a transformational development, manufacturing, and mistribution model. *2015 PDA Annual Meeting*, Las Vegas, NV, **2015**. http://cureconnect.org/wp-content/uploads/2015/05/CURE-Final_noVideo.pdf (accessed July 27, 2016)

(19)   Wiles, C.; Watts, P. *Micro reaction technology in organic synthesis*. CRC Press: Boca Raton, FL, **2016**.

(20)   Brzozowski, M.; O'Brien, M.; Ley, S.V.; Polyzos, A. Flow chemistry: intelligent processing of gas-liquid transformations using a tube-in-tube reactor. *Acc. Chem. Res.* **2015**, *48(2)*, 349-362.

(21)   Hessel, V.; Vural Gürsel, I.; Wang, Q.; Noel, T.; Lang, J. Potential analysis of smart flow processing and micro process technology for fastening process development: use of chemistry and process design as intensification fields. *Chem. Eng. Technol.* **2012**, *35(7)*, 1184-1204.

(22)   Hartman, R.; Jensen, K.F. Microchemical systems for continuous-flow synthesis. *Lab Chip* **2009**, *9(17)*, 2495-2507.

(23)   Mason, B.P.; Price, K.E.; Steinbacher, J.L.; Bogdan, A.R.; McQuade, D.T. Greener approaches to organic synthesis using microreactor technology. *Chem. Rev.* **2007**, *107(6)*, 2300-2318.

(24)   Jensen, K.F. Microreaction engineering-is small better?. *Chem. Eng. Sci.* **2001**, *56(2)*, 293-303.

(25)   Moore, J.S.; Smith, C.D.; Jensen, K.F. Kinetic analysis and automated screening of aminocarbonylation of aryl halides in flow. *React. Chem. Eng.* **2016**, *1(3)*, 272-279.

(26)   Mills, P.L.; Quiram, D.J.; Ryley, J.F. Microreactor technology and process miniaturization for catalytic reactions – A perspective on recent developments and emerging technologies. *Chem. Eng. Sci.* **2007**, *62(24)*, 6992-7010.

(27)   Zaborenko, N.; Murphy, E.R.; Kralj, J.G.; Jensen K.F. Synthesis and kinetics of highly energetic intermediates by micromixers: direct multistep synthesis of sodium nitrotetrazolate. *Ind. Eng. Chem. Res.* **2010**, *49(9)*, 4132-4139.

(28)   Liu, X.; Jensen, K.F. Multistep synthesis of amides from alcohols and amines in continuous flow microreactor systems using oxygen and urea hydrogen peroxide as oxidants. *Green Chem.* **2013**, *15(6)*, 1538-1541.

(29)   Hartman, R.L. Managing solids in microreactors for the upstream continuous processing of fine chemicals. *Org. Process Res. Dev.* **2012**, *16(5)*, 870-887.

(30)   Hartman, R.L.; Naber, J.R.; Zaborenko, N.; Buchwald, S.L.; Jensen, K.F. Overcoming the challenges of solid bridging and constriction during Pd-Catalyzed C-N bond formation in microreactors. *Org. Process Res. Dev.* **2010**, *14(6)*, 1347-1357.

(31)   McMullen, J.P.; Stone, M.T.; Buchwald, S.L.; Jensen, K.F. An integrated microreactor system for self-optimization of a Heck reaction: From micro-to mesoscale flow systems. *Angew. Chemie - Int. Ed.* **2010**, *49(39)*, 7076-7080.

(32)   Zhang, Y.; Born, S.C.; Jensen, K.F. Scale-up investigation of the continuous phase-transfer-catalyzed hypochlorite oxidation of alcohols and aldehydes. *Org. Process Res. Dev.* **2014**, *18(11)*, 1476-1481.

(33)   Cole, K.P.; Campbell, B.M.; Forst, M.B.; McClary Groh, J.; Hess, M.; Johnson, M.D.; Miller, R.D.; Mitchell, D.; Polster, C.S.; Reizman, B.J.; Rosemeyer, M. An automated intermittent flow approach to continuous Suzuki coupling. *Org. Process Res. Dev.* **2016**, *20(4)*, 820-830.

(34)   Tsukanov, S.V.; Johnson, M.D.; May, S.A.; Rosemeyer, M.; Watkins, M.A.; Kolis, S.P.; Yates, M.H.; Johnston, J.N. Development of an intermittent-flow enantioselective aza-Henry reaction using an arylnitromethane and homogeneous Brønsted acid-base catalyst with recycle. *Org. Process Res. Dev.* **2016**, *20(2)*, 215-226.

(35)   White, T.D.; Alt, C.A.; Cole, K.P.; Groh, J.M.; Johnson, M.D.; Miller, R.D. How to convert a walk-in hood into a manufacturing facility: demonstration of a

continuous, high-temperature cyclization to process solids in flow. *Org. Process Res. Dev.* **2014**, *18(11)*, 1482-1491.

(36)   Wong, S.W.; Changi, S.M.; Shields, R.; Bell, W.; McGarvey, B.; Johnson, M.D.; Sun, W.M.; Braden, T.M.; Kopach, M.E.; Spencer, R.D.; Flanagan, G. Operation strategy development for Grignard reaction in a continuous stirred tank reactor. *Org. Process Res. Dev.* **2016**, *20(2)*, 540-550.

(37)   Johnson, M.D.; May, S.A.; Calvin, J.R.; Remacle, J.; Stout, J.R.; Diseroad, W.D.; Zaborenko, N.; Haeberle, B.D.; Sun, W.M.; Miller, M.T.; Brennan, J. Development and scale-up of a continuous, high-pressure, asymmetric hydrogenation reaction, workup, and isolation. *Org. Process Res. Dev.* **2012**, *16(5)*, 1017-1038.

(38)   Zaborenko, N.; Linder, R.J.; Braden, T.M.; Campbell, B.M.; Hansen, M.M.; Johnson, M.D. Development of pilot-scale continuous production of an LY2886721 starting material by packed-bed hydrogenolysis. *Org. Process Res. Dev.* **2015**, *19(9)*, 1231-1243.

(39)   May, S.A.; Johnson, M.D.; Braden, T.M.; Calvin, J.R.; Haeberle, B.D.; Jines, A.R.; Miller, R.D.; Plocharczyk, E.F.; Rener, G.A.; Richey, R.N.; Schmid, C.R. Rapid development and scale-up of a 1 H-4-substituted imidazole intermediate enabled by chemistry in continuous plug flow reactors. *Org. Process Res. Dev.* **2012**, *16(5)*, 982-1002.

(40)   Abrams, M.L.; Buser, J.Y.; Calvin, J.R.; Johnson, M.D.; Jones, B.R.; Lambertus, G.; Landis, C.R.; Martinelli, J.R.; May, S.A.; McFarland, A.D.; Stout, J.R. Continuous liquid vapor reactions part 2: Asymmetric hydroformylation with rhodium-bisdiazaphos catalysts in a vertical pipes-in-series reactor. *Org. Process Res. Dev.* **2016**, *20(5)*, 901-910.

(41)   Johnson, M.D.; May, S.A.; Calvin, J.R.; Lambertus, G.R.; Kokitkar, P.B.; Landis, C.R.; Jones, B.R.; Abrams, M.L.; Stout, J.R. Continuous liquid vapor reactions part 1: Design and characterization of a reactor for asymmetric hydroformylation. *Org. Process Res. Dev.* **2016**, *20(5)*, 888-900.

(42)   Johnson, M.D.; May, S.A.; Haeberle, B.D.; Lambertus, G.R.; Pulley, S.R.; Stout, J.R. Design and comparison of tubular and pipes-in-series continuous reactors for direct asymmetric reductive amination. *Org. Process Res. Dev.* **2016**, *20(7)*, 1305-1320.

(43)   Lundin, M. D.; Danby, A. M.; Akien, G. R.; Venkitasubramanian, P.; Martin, K. J.; Busch, D. H.; Subramaniam, B. Intensified and safe ozonolysis of fatty acid methyl esters in liquid CO2 in a continuous reactor. *AIChE J.* **2017**, *63(7)*, 2819-2826.

(44)   CSB. *Improving reactive hazard management.* U.S. Chemical Safety and Hazard Investigation Board, Washington, DC, **2002**. http://www.csb.gov/improving-reactive-hazard-management/ (accessed July 27, 2016)

(45)   Crowl, D.A.; Louvar, J.F. *Chemical process safety: fundamentals with applications*, 3rd ed. Prentice Hall: Upper Saddle River, NJ, **2011**.

(46)   Allian, A.D.; Richter, S.M.; Kallemeyn, J.M.; Robbins, T.A.; Kishore, V. The development of continuous process for alkene ozonolysis based on combined in situ FTIR, calorimetry, and computational chemistry. *Org. Process Res. Dev.* **2010**, *15(1)*, 91-97.

(47)   González-Bobes, F.; Kopp, N.; Li, L.; Deerberg, J.; Sharma, P.; Leung, S.; Davies, M.; Bush, J.; Hamm, J.; Hrytsak, M. Scale-up of azide chemistry: a case study. *Org. Process Res. Dev.* **2012**, *16(12)*, 2051-2057.

(48)   Likhite, N.; Lakshminarasimhan, T.; Rao, M.H.R.; Shekarappa, V.; Sidar, S.; Subramanian, V.; Fraunhoffer, K.J.; Leung, S.; Vaidyanathan, R. A scalable synthesis of 2-(1, 2, 4-Oxadiazol-3-yl) propan-2-amine hydrobromide using a process safety-driven protecting group strategy. *Org. Process Res. Dev.* **2016**, *20(7)*, 1328-1335.

(49)   Wang, Z.; Richter, S.M.; Gates, B.D.; Grieme, T.A. Safety concerns in a pharmaceutical manufacturing process using dimethyl sulfoxide (DMSO) as a solvent. *Org. Process Res. Dev.* **2012**, *16(12)*, 1994-2000.

(50)   Wang, Z.; Richter, S.M.; Gandarilla, J.; Kruger, A.W.; Rozema, M.J. Safe scale-up of a hydrazine condensation by the addition of a base. *Org. Process Res. Dev.* **2013**, *17(12)*, 1603-1610.

(51)   Wang, Z.; Richter, S.M.; Bellettini, J.R.; Pu, Y.M.; Hill, D.R. Safe scale-up of pharmaceutical manufacturing processes with dimethyl sulfoxide as the solvent and a reactant or a byproduct. *Org. Process Res. Dev.* **2014**, *18(12)*, 1836-1842.

(52)   Bollinger, R.E.; Crowl, D.A. *Inherently safer chemical processes: A life cycle approach*. American Institue of Chemical Engineers, New York, NY, **1997**.

(53)   Hendershot, D.C. Inherently safer chemical process design. *J. Loss Prev. Process Ind.* **1997**, *10(3)*, 151-157.

(54)   Kletz, T. A. Inherently safer plants. *Plant/Oper. Prog.* **1985**, *4(3)*, 164-167.

(55)   Kletz, T. A. Inherently safer plants: An update. *Plant/Oper. Prog.* **1991**, *10(2)*, 81-84.

(56)   Kletz, T. A. Inherently safer design – Its scope and future. *Process Saf. Environ. Prot.* **2003**, *81(6)*, 401-405.

(57)   Khan, F.I.; Amyotte, P.R. How to make inherent safety practice a reality. *Can. J. Chem. Eng.* **2003**, *81(1)*, 2-16.

(58)   Bissantz, C.; Grether, U.; Hebeisen, P.; Kimbara, A.; Liu, Q.; Nettekoven, M.; Prunotto, M.; Roever, S.; Rogers-Evans, M.; SchulzGasch, T.; Ullmer, C.; Wang, Z.; Yang, W. Novel pyridine derivatives. U.S. Patent, US 20120316147 A1, **2012**.

(59)   Scriven, E.F.V.; Murugan, R. Pyridine and pyridine derivatives. *Kirk-Othmer Encyclopedia of Chemical Technology*; Wiley-Interscience: Hoboken, NJ, **2004**.

(60)   Shimizu, S.; Watanabe, N.; Kataoka, T.; Shoji, T.; Abe, N.; Morishita, S.; Ichimura, H. Pyridine and pyridine derivatives. *Ullmann's Encyclopedia of Industrial Chemistry*; Wiley-VCH: Weinheim, Germany, **2000**.

(61)   Joule, J.A.; Mills, K. *Heterocyclic chemistry*. John Wiley & Sons: Chichester, United Kingdom, **2008**.

(62)   Liu, X.; Jensen, K.F. Direct oxidative amidation of aromatic aldehydes using aqueous hydrogen peroxide in continuous flow microreactor systems. *Green Chem.* **2012**, *14(5)*, 1471-1474.

(63)   Misono, M.; Ono, I.; Koyano, G.; Aoshima, A. Heteropolyacids. Versatile green catalysts usable in a variety of reaction media. *Pure Appl. Chem.* **2000**, *72(7)*, 1305-1311.

(64)   Misono, M. Recent progress in the practical applications of heteropolyacid and perovskite catalysts: Catalytic technology for the sustainable society. *Catal. Today* **2009**, *144(3)*, 285-291.

(65)   Papadaki, M.; Gao, J. Kinetic models of complex reaction systems. *Comput. Chem. Eng.* **2005**, *29(11)*, 2449-2460.

(66)   Sempere, J.; Nomen, R.; Rodriguez, J. L.; Papadaki, M. Modelling of the reaction of N-Oxidation of 2-Methylpyridine using hydrogen peroxide and a complex metal catalyst. *Chem. Eng. Process.: Process Intensif.* **1998**, *37(1)*, 33-46.

(67) Papadaki, M.; Emery, R. J.; Serra, E.; Nomen, R.; Sempere, J. Sensitivity analysis of the 2-Methylpyridine N-oxidation kinetic model. *Green Chem.* **2002**, *4(3)*, 199-205.

(68) Pineda-Solano, A. Design of inherently safer complex reactive processes: Application on the N-oxidation of alkylpyridines. PhD Thesis, Texas A&M University, College Station, TX, **2014**.

(69) Kozhevnikov, I.V.E. Advances in catalysis by heteropolyacids. *Russ. Chem. Rev.* **1987**, *56(9)*, 811-825.

(70) Keggin, J.F. The structure and formula of 12-phosphotungstic acid. *Proc. Roy. Soc. London A: Math., Phy., Eng. Sci.* **1934**, *144(851)*, 75-100.

(71) Saenz-Noval, L. Evaluation of alternatives for safer and more efficient reactions: a study of the N-oxidation of alkylpyridines. PhD Dissertation, Texas A&M University, College Station, TX, **2011**.

(72) Stoessel, F. *Thermal safety of chemical processes: risk assessment and process design*. Wiley-VCH Verlag GmbH & Co. KGaA: Weinheim, Germany, **2008**.

(73) Pineda-Solano, A.; Saenz-Noval, L.; Nayak, S.; Waldram, S.; Papadaki, M.; Mannan, M. S. Inherently safer reactors: Improved efficiency of 3-Picoline N-oxidation in the temperature range 110 – 125°C. *Process Saf. Environ. Prot.* **2012**, *90(5)*, 404-410.

(74) Saenz-Noval, L.; Vazquez, V.C.; Liu, L.; Rogers, W.J.; Mannan, M.S.; Papadaki, M. 2-Methylpyridine-N-oxidation runaway studies. *J. Loss. Prevent. Proc.* **2009**, *22(6)*, 839-843.

(75) Saenz-Noval, L.; Vazquez, V.C.; Rogers, W.J.; Papadaki, M.; Mannan, M.S. Thermal decomposition of 2-methylpyridine N-oxide: effect of temperature and influence of phosphotungstic acid as the catalyst. *Catal. Commun.* **2011**, *12(14)*, 1370-1373.

(76) Pineda-Solano, A.; Saenz, L.R.; Carreto, V.; Papadaki, M.; Mannan, M.S. Toward an inherently safer design and operation of batch and semi-batch processes: the N-oxidation of alkylpyridines. *J. Loss. Prevent. Proc.* **2012**, *25(5)*, 797-802.

(77) Liljenroth, F.G. Starting and stability phenomena of ammonia-oxidation and similar reactions. *Chem. Metall. Eng.* **1918**, *19(6)*, 287-293.

(78) Bilous, O.; Amundson, N.R. Chemical reactor stability and sensitivity. *AIChE J.* **1955**, *1(4)*, 513-521.

(79) Farr, W.W.; Aris, R. "Yet who would have thought the old man to have had so much blood in him?" – Reflections on the multiplicity of steady states of the stirred tank reactor. *Chem. Eng. Sci.* **1986**, *41(6)*, 1385-1402.

(80) Van Den Bosch, B.; Luss, D. Uniqueness and multiplicity criteria for an nth order chemical reaction. *Chem. Eng. Sci.* **1977**, *32(2)*, 203-212.

(81) Tsotsis, T.T.; Schmitz, R.A. Exact uniqueness and multiplicity criteria for a positive-order Arrhenius reaction in a lumped system. *Chem. Eng. Sci.* **1979**, *34(1)*, 135-137.

(82) Leib, T.M.; Luss, D. Exact uniqueness and multiplicity criteria for an nth order reaction in a CSTR. *Chem. Eng. Sci.* **1981**, *36(1)*, 210-212.

(83) Golubitsky, M.; Keyfitz, B. A qualitative study of the steady-state solutions for a continuous flow stirred tank reactor. *SIAM J. Math. Anal.* **1980**, *11(2)*, 316-339.

(84) Golubitsky, M.; Schaeffer, D.G. A theory for imperfect bifurcation via singularity theory. Commun. *Pure Appl. Math.* **1979**, *32(1)*, 21-98.

(85) Balakotaiah, V.; Luss, D. Global analysis of the multiplicity features of multi-reaction lumped-parameter systems. *Chem. Eng. Sci.* **1984**, *39(5)*, 865-881.

(86) Balakotaiah, V.; Luss, D. Multiplicity features of reacting systems: Dependence of the steady-states of a CSTR on the residence time. *Chem. Eng. Sci.* **1983**, *38(10)*, 1709-1729.

(87) Balakotaiah, V.; Luss, D. Exact steady-state multiplicity criteria for two consecutive or parallel reactions in lumped-parameter-systems. *Chem. Eng. Sci.* **1982**, *37(3)*, 433-445.

(88) Aris, R.; Amundson, N.R. An analysis of chemical reactor stability and control-I: The possibility of local control, with perfect or imperfect control mechanisms. *Chem. Eng. Sci.* **1958**, *7(3)*, 121-131.

(89)   Aris, R.; Amundson, N.R. An analysis of chemical reactor stability and control-II: The evolution of proportional control. *Chem. Eng. Sci.* **1958**, *7(3)*, 132-147.

(90)   Aris, R.; Amundson, N.R. An analysis of chemical reactor stability and control-III: The principles of programming reactor calculations. Some extensions. *Chem. Eng. Sci.* **1958**, *7(3)*, 148-155.

(91)   Uppal, A.; Ray, W.H.; Poore, A.B. On the dynamic behavior of continuous stirred tank reactors. *Chem. Eng. Sci.* **1974**, *29(4)*, 967-985.

(92)   Williams, D.C.; Calo, J.M. "Fine structure" of the CSTR parameter space. *AIChE J.* **1981**, *27(3)*, 514-516.

(93)   Kwong, V.K.; Tsotsis, T.T. Fine structure of the CSTR parameter space. *AIChE J.* **1983**, *29(2)*, 343-347.

(94)   Razón, L.F.; Schmitz, R.A. Multiplicities and instabilities in chemically reacting systems – a review. *Chem. Eng. Sci.* **1987**, *42(5)*, 1005-1047.

(95)   Morbidelli, M.; Varma, A.; Aris, R. Reactor steady-state multiplicity and stability. *Chemical Reaction and Reactor Engineering.* Marcel Dekker Inc.: New York, NY, **1987**.

(96)   Harmon Ray, W.; Villa, C.M. Nonlinear dynamics found in polymerization processes – a review. *Chem. Eng. Sci.* **2000**, *55(2)*, 275-290.

(97)   Chang, M.; Schmitz, R.A. An experimental study of oscillatory states in a stirred reactor. *Chem. Eng. Sci.* **1975**, *30(1)*, 21-34.

(98)   Westerterp, K.R.; Lewak, M.; Molga, E.J. Boundary diagrams safety criterion for liquid phase homogeneous semibatch reactors. *Ind. Eng. Chem. Res.* **2014**, *53(14)*, 5778-5791.

(99)   Poore, A.B. On the theory and application of the Hopf-Friedrichs bifurcation theory. *Arch. Ration. Mech. Anal.* **1976**, *60(4)*, 371-393.

(100) Poore, A.B. A model equation arising from chemical reactor theory. *Arch. Ration. Mech. Anal.* **1973**, *52(4)*, 358-388.

(101) Evangelista, J.J.; Katz, S.; Shinnar, R. Scale-up criteria for stirred tank reactors. *AIChE J.* **1969**, *15(6)*, 843-853.

(102) Nauman, E.B. *Chemical reactor design, optimization, and scaleup*, second ed. John Wiley & Sons: Hoboken, NJ, **2008**.

(103) Norwood, K.W.; Metzner, A.B. Flow patterns and mixing rates in agitated vessels. *AIChE J.* **1960**, *6(3)*, 432-437.

(104) Devia, N.; Luyben, W.L. Reactors-size versus stability. *Hydrocarb. Process.* **1978**, *57(6)*, 119-122.

(105) Milewska, A.; Molga, E.J. Safety aspects in modelling and operating of batch and semibatch stirred tank chemical reactors. *Chem. Eng. Res. Des.* **2010**, *88(3)*, 304-319.

(106) Milewska, A.; Molga, E.J. CFD simulation of accidents in industrial batch stirred tank reactors. *Chem. Eng. Sci.* **2007**, *62(18)*, 4920-4925.

(107) Rudniak, L.; Machniewski, P.M.; Milewska, A.; Molga, E.J. CFD modelling of stirred tank chemical reactors: homogeneous and heterogeneous reaction systems. *Chem. Eng. Sci.* **2004**, *59(22)*, 5233-5239.

(108) Rudniak, L.; Milewska, A.; Molga, E.J. CFD simulations for safety of chemical reactors and storage tanks. *Chem. Eng. Technol.* **2011**, *34(11)*, 1781-1789.

(109) Wyss, H.M.; Blair, D.L.; Morris, J.F.; Stone, H.A.; Weitz, D.A. Mechanism for clogging of microchannels. *Phys. Rev. E: Stat. Nonlin. Soft Matter Phys.* **2006**, *74(6)*, 061402.

(110) Hund, E.; Massart, D.L.; Smeyers-Verbeke, J. Operational definitions of uncertainty. *TrAC - Trends Anal. Chem.* **2001**, *20(8)*, 394-406.

(111) Papadaki, M.; Nawada, H.P.; Gao, J.; Fergusson-Rees, A.; Smith, M. Isothermal calorimetry: Impact of measurements error on heat of reaction and kinetic calculations. *J. Hazard. Mater.* **2007**, *142(3)*, 705-712.

(112) Hauptmanns, U. Comparative assessment of the dynamic behaviour of an exothermal chemical reaction including data uncertainties. *Chem. Eng. J.* **2008**, *140(1)*, 278-286.

(113) Kletz, T.A. Making safety second nature. *Process Saf. Prog.* **1998**, *17(3)*, 196-199.

(114) Doherty, M.F.; Fidkowski, Z.T.; Malone, M.F.; Taylor, R.; Green, D.W. *Perry's Chemical Engineers' Handbook*, eight ed. McGraw-Hill Professional, **2007**, pp. 2-44, 2-106.

(115) NIST Chemistry WebBook. Pyridine, 3-methyl-: Condensed phase thermochemistry data. http://webbook.nist.gov/cgi/cbook.cgi?ID=C108996&Units=SI&Mask=2#Thermo-Condensed (accessed July 1, 2014)

(116) Giguére, P.A.; Carmichael, J.L. Heat Capacities for Water-Hydrogen Peroxide Systems between 25 °C and 60 °C. *J. Chem. Eng. Data* **1962**, *7(4)*, 526-527.

(117) Strogatz, S. *Nonlinear dynamics and chaos: with applications to physics, biology, chemistry and engineering*. Westview Press: Boulder, CO, **2000**.

(118) Mallia, C.J.; Baxendale, I.R. The use of gases in flow synthesis. *Org. Process Res. Dev.* **2015**, *20(2)*, 327-360.

(119) Polyzos, A.; O'Brien, M.; Petersen, T.P.; Baxendale, I.R.; Ley, S.V. The continuous-flow synthesis of carboxylic acids using CO_2 in a tube-in-tube gas permeable membrane reactor. *Angew. Chemie - Int. Ed.* **2011**, *50(5)*, 1190-1193.

(120) Petersen, T.P.; Polyzos, A.; O' Brien, M.; Ulven, T.; Baxendale, I.R.; Ley, S.V. The oxygen-mediated synthesis of 1, 3-Butadiynes in continuous flow: Using Teflon AF-2400 to effect gas/liquid contact. *ChemSusChem.* **2012**, *5(2)*, 274-277.

(121) Buba, A.E.; Koch, S.; Kunz, H.; Löwe, H. Fluorenylmethoxycarbonyl-N-Methylamino acids synthesized in a flow tube-in-tube reactor with a liquid-liquid semipermeable membrane. *Eur. J. Org. Chem.* **2013**, *2013(21)*, 4509-4513.

(122) Yang, L.; Jensen, K.F. Mass transport and reactions in the tube-in-tube reactor. *Org. Process Res. Dev.* **2013**, *17(6)*, 927-933.

(123) Koos, P.; Gross, U.; Polyzos, A.; O'Brien, M.; Baxendale, I.; Ley, S.V. Teflon AF-2400 mediated gas-liquid contact in continuous flow methoxycarbonylations and in-line FTIR measurement of CO concentration. *Org. Biomol. Chem.* **2011**, *9(20)*, 6903-6908.

(124) Gross, U.; Koos, P.; O'Brien, M.; Polyzos, A.; Ley, S.V. A general continuous flow method for palladium catalysed carbonylation reactions using single and multiple tube-in-tube gas-liquid microreactors. *Eur. J. Org. Chem.* **2014**, *2014(29)*, 6418-6430.

(125) O'Brien, M.; Baxendale, I.R.; Ley, S.V. Flow ozonolysis using a semipermeable Teflon AF-2400 membrane to effect gas-liquid contact. *Org. Lett.* **2010**, *12(7)*, 1596-1598.

(126) Cranwell, P.B.; O'Brien, M.; Browne, D.L.; Koos, P.; Polyzos, A.; Peña-López, M.; Ley, S.V. Flow synthesis using gaseous ammonia in a Teflon AF-2400 tube-in-tube reactor: Paal–Knorr pyrrole formation and gas concentration measurement by inline flow titration. *Org. Biomol. Chem.* **2012**, *10(30)*, 5774-5779.

(127) Browne, D.L.; O'Brien, M.; Koos, P.; Cranwell, P.B.; Polyzos, A.; Ley, S.V. Continuous-flow processing of gaseous ammonia using a Teflon AF-2400 tube-

in-tube reactor: Synthesis of thioureas and in-line titrations. *Synlett* **2012**, *23(09)*, 1402-1406.

(128) O'Brien, M.; Taylor, N.; Polyzos, A.; Baxendale, I.R.; Ley, S.V. Hydrogenation in flow: Homogeneous and heterogeneous catalysis using Teflon AF-2400 to effect gas-liquid contact at elevated pressure. *Chem. Sci.* **2011**, *2(7)*, 1250-1257.

(129) Newton, S.; Ley, S.V.; Arcé, E.C.; Grainger, D.M. Asymmetric homogeneous hydrogenation in flow using a tube-in-tube reactor. *Adv. Synth. Catal.* **2012**, *354(9)*, 1805-1812.

(130) Zhang, H.; Wang, S.; Weber, S.G. Morphology and free volume of nanocomposite Teflon AF 2400 films and their relationship to transport behavior. *J. Membr. Sci.* **2013**, *443*, 115-123.

(131) Zhang, H.; Wang, S.; Weber, S.G. Nanocomposite Teflon AF 2400 films as tunable platforms for selective transport. *Anal. Chem.* **2012**, *84(22)*, 9920-9927.

(132) Zhang, H.; Hussam, A.; Weber, S.G. Properties and transport behavior of Perfluorotripentylamine (FC-70)-doped amorphous Teflon AF 2400 films. *J. Am. Chem. Soc.* **2010**, *132(50)*, 17867-17879.

(133) Zaman, J.; Chakma, A. Inorganic membrane reactors. *J. Membr. Sci*. **1994**, *92*, 1-28.

(134) Marcano, J.G.S.; Tsotsis, T.T. *Catalytic membranes and membrane reactors*; Wiley-VCH: Weinheim, Germany, **2002**.
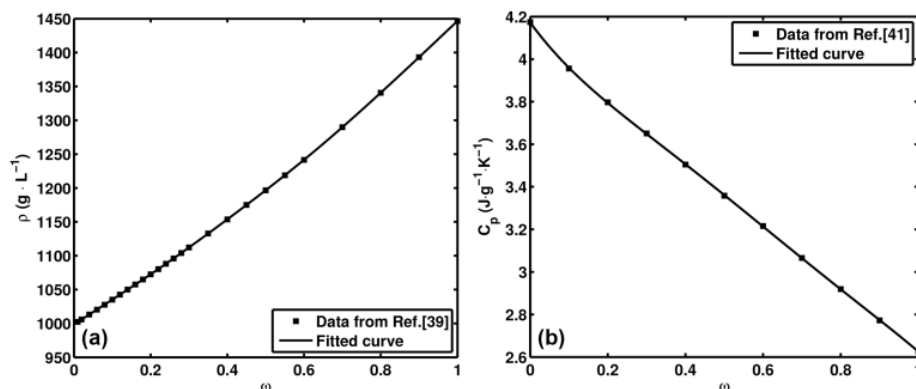
(135)   Cui, X.; Mannan, M.S.; Wilhite, B.A. Towards efficient and inherently safer continuous reactor alternatives to batch-wise processing of fine chemicals: CSTR nonlinear dynamics analysis of alkylpyridines N-oxidation. *Chem. Eng. Sci.* **2015**, *137*, 487-503.

(136)   Inopor® GmbH. *Geometries, Materials, and Pore Sizes.* http://www.inopor.com/en/products/membranes.html (accessed March 1, 2016)

(137)   Froment, G.F.; Bischoff, K.B.; De Wilde, J. *Chemical reactor analysis and design*, 3rd ed.; Wiley: Hoboken, NJ, **2011**.

(138)   Geankoplis, C.J. *Transport processes and unit operations*, 3rd ed.; Prentice-Hall: Engelwood Cliffs, NJ, **1993**.

(139)   Wilke, C.R.; Chang, P. Correlation of diffusion coefficients in dilute solutions. *AIChE J.* **1955**, *1(2)*, 264-270.

(140)   Sheldon, R.A. E factors, green chemistry and catalysis: An odyssey. *Chem. Commun.* **2008**, *29*, 3352-3365.

(141)   Hu, C; Shaughnessy, K.H.; Hartman, R.L. Influence of water on the deprotonation and the ionic mechanisms of a Heck alkynylation and its resultant E-factors. *React. Chem. Eng.* **2016**, *1(1)*, 65-72.

(142)   Sabio, J.C.; Domier, R.C.; Moore, J.N.; Shaughnessy, K.H.; Hartman, R.L. Palladium theory of aqueous-phase Heck alkynylations for intensification of discovery and manufacture. *Chem. Eng. Technol.* **2015**, *38(10)*, 1717-1725.

DERIVE CORRELATION BETWEEN β AND THE WEIGHT FRACTION OF

HYDROGEN PEROXIDE AQUEOUS SOLUTION[*]

Here, 3-picoline is used as an example to illustrate how the weight fraction of hydrogen peroxide aqueous solution ω directly influences the overall feed concentration of alkylpyridine $[A]_f$, the average density $\bar{\rho}$ and heat capacity $\overline{C_P}$ of the overall inflow, and thus β.

Figure A1. Cited data and fitted curve for (a) density and (b) heat capacity of $H_2O_2(aq)$ as a function of hydrogen peroxide weight fraction ω

According to Doherty et al.,[114] pure 3-picoline has a density of $957 \text{ g} \cdot \text{L}^{-1}$, or equivalently, a concentration of $10.29 \text{ mol} \cdot \text{L}^{-1}$. And its heat capacity is $1.706 \text{ J} \cdot \text{g}^{-1} \cdot \text{K}^{-1}$, as shown in NIST Chemistry WebBook[115]. Doherty et al.[114] also tabulates the density of hydrogen peroxide aqueous solution as the weight fraction of hydrogen peroxide ω varies. The data sets in the table are employed here to fit a 9th order polynomial correlation between the weight fraction ω and the density ρ $(\text{g} \cdot \text{L}^{-1})$ of the solution, as shown in Eq. (A1) and Figure A1(a). Values of those coefficients in Eq. (A1) as well as their 95% confidence interval and goodness of fitting are given in Table A1 and A2 respectively.

$$\rho(\omega) = p_1\omega^9 + p_2\omega^8 + p_3\omega^7 + p_4\omega^6 + p_5\omega^5 + p_6\omega^4 + p_7\omega^3 + p_8\omega^2 + p_9\omega + p_{10} \qquad \text{(A1)}$$

Likewise, the heat capacity of hydrogen peroxide aqueous solution is fitted here to a 5th order polynomial correlation with ω based upon experimental data reported elsewhere.[116] The correlation is given in Eq. (A2) and Figure A1(b) while relevant coefficients as well as their 95% confidence interval and goodness of fitting are also given in Table A1 and A2 respectively.

$$C_P(\omega) = m_1\omega^5 + m_2\omega^4 + m_3\omega^3 + m_4\omega^2 + m_5\omega + m_6 \qquad \text{(A2)}$$

Assume the average molecular weight of hydrogen peroxide aqueous solution is correlated with its weight fraction by Eq. (A3). Then the molar concentration of hydrogen peroxide in the solution could be expressed as Eq. (A4), where ρ is calculated from Eq. (A1).

$$\overline{MW} = \cfrac{1}{\cfrac{\omega}{34} + \cfrac{1-\omega}{18}} \tag{A3}$$

$$c_{H_2O_2} = \frac{\rho}{\overline{MW}} \times \text{mol\%} = \rho\left(\frac{\omega}{34} + \frac{1-\omega}{18}\right)\cfrac{\cfrac{\omega}{34}}{\cfrac{\omega}{34} + \cfrac{1-\omega}{18}} = \frac{\rho\omega}{34} \tag{A4}$$

According to the definition of α, which is the feed concentration ratio of hydrogen peroxide to alkylpyridine in the overall feed flow,

$$\alpha = \frac{[B]_f}{[A]_f} = \frac{c_{H_2O_2} \times q_{H_2O_2\,(aq)}\big/q}{c_{3\text{-picoline}} \times q_{3\text{-picoline}}\big/q} = \frac{\rho\omega/34}{10.29}\frac{q_{H_2O_2\,(aq)}}{q_{3\text{-picoline}}} \tag{A5}$$

$$q = q_{3\text{-picoline}} + q_{H_2O_2\,(aq)} \tag{A6}$$

the feed flow rate of 3-picoline depends on the feed flow rate of the hydrogen peroxide aqueous solution given a constant α, as shown in Eq. (A7).

$$q_{3\text{-picoline}} = \frac{\rho\omega/34}{10.29} q_{H_2O_2\,(aq)} \tag{A7}$$

Therefore the overall feed concentration of 3-picoline and the average density and heat capacity of the overall inflow could be calculated from Eqs. (A8) – (A10) along with Eqs. (A1) and (A2). Practically, since other parameters involved in the definition of β have been claimed to be constant and specified in Table 1.1 and 2.1, β could be easily translated into ω by substituting Eqs. (A8) – (A10) into Eq. (A11) and solving the resulting algebraic equation.

Table A1. Coefficients in Eqs. (A1) and (A2)

Correlation	Coefficients	Values	95% confidence bounds
Eq. (A1)	p_1	-1.244×10^4	$(-1.83 \times 10^4, -6586)$
	p_2	5.779×10^4	$(3.247 \times 10^4, 8.311 \times 10^4)$
	p_3	-1.108×10^5	$(-1.565 \times 10^5, -6.511 \times 10^4)$
	p_4	1.129×10^5	$(6.811 \times 10^4, 1.576 \times 10^5)$
	p_5	-6.533×10^4	$(-9.114 \times 10^4, -3.952 \times 10^4)$
	p_6	2.131×10^4	$(1.239 \times 10^4, 3.023 \times 10^4)$
	p_7	-3594	$(-5392, -1796)$
	p_8	327.3	$(131.6, 523)$
	p_9	351.9	$(342.2, 361.6)$
	p_{10}	998.7	$(998.5, 998.8)$
Eq. (A2)	m_1	-2.547	$(-4.213, -0.88)$
	m_2	7.658	$(3.471, 11.85)$
	m_3	-8.628	$(-12.36, -4.896)$
	m_4	4.465	$(3.066, 5.864)$
	m_5	-2.496	$(-2.695, -2.297)$
	m_6	4.173	$(4.164, 4.181)$

$$[A]_f = \frac{c_{\text{3-picoline}} \times q_{\text{3-picoline}}}{q} = \frac{10.29 q_{\text{3-picoline}}}{q_{\text{3-picoline}} + q_{\text{H}_2\text{O}_2\text{(aq)}}} = \frac{10.29 \dfrac{\rho\omega/34}{10.29\alpha} q_{\text{H}_2\text{O}_2\text{(aq)}}}{\dfrac{\rho\omega/34}{10.29\alpha} q_{\text{H}_2\text{O}_2\text{(aq)}} + q_{\text{H}_2\text{O}_2\text{(aq)}}} = \frac{\dfrac{\rho\omega}{34\alpha}}{\dfrac{\rho\omega/34}{10.29\alpha} + 1}$$

(A8)

$$\bar{\rho} = \frac{\rho_{\text{3-picoline}} q_{\text{3-picoline}} + \rho q_{\text{H}_2\text{O}_2\text{(aq)}}}{q} = \frac{957 \dfrac{\rho\omega/34}{10.29\alpha} q_{\text{H}_2\text{O}_2\text{(aq)}} + \rho q_{\text{H}_2\text{O}_2\text{(aq)}}}{\dfrac{\rho\omega/34}{10.29\alpha} q_{\text{H}_2\text{O}_2\text{(aq)}} + q_{\text{H}_2\text{O}_2\text{(aq)}}} = \frac{957 \dfrac{\rho\omega/34}{10.29\alpha} + \rho}{\dfrac{\rho\omega/34}{10.29\alpha} + 1}$$

(A9)

$$\overline{C_P} = \frac{\rho_{3\text{-picoline}}q_{3\text{-picoline}}C_{P(3\text{-picoline})} + \rho q_{H_2O_2(aq)}C_P}{\rho_{3\text{-picoline}}q_{3\text{-picoline}} + \rho q_{H_2O_2(aq)}} = \frac{957\dfrac{\rho\omega/34}{10.29\alpha}\times 1.706 + \rho C_P}{957\dfrac{\rho\omega/34}{10.29\alpha} + \rho} \qquad (A10)$$

$$\beta = \frac{(-\Delta H_{ox})[A]_f}{\rho\overline{C_P}T_f} \quad \gamma = \frac{(-\Delta H_{ox})[A]_f}{\rho\overline{C_P}T_f}\frac{E_{1b}}{RT_f} \qquad (A11)$$

Table A2. Goodness of fitting for Eqs. (A1) and (A2)

Correlation	SSE	R-square	Adjusted R-square	RMSE
Eq. (A1)	0.03214	1.0000	1.0000	0.04482
Eq. (A2)	5.2467×10^{-5}	1.0000	1.0000	0.0032

Note that the general form of Eqs. (A8) − (A10) keeps the same when other alkylpyridines are used with the density, concentration and heat capacity of alkylpyridines (*e.g.*, 957 g · L^{-1}, 10.29 mol · L^{-1} and 1.706 J · g^{-1} · K^{-1} for 3-picoline) being the case-by-case terms to be adjusted accordingly.

APPENDIX B

DETERMINE EXISTENCE OF MULTIPLE STEADY STATES AND LIMIT

CYCLES AS WELL AS THEIR STABILITY[*]

A change in the number of steady states is predicted by the existence of a saddle-node bifurcation, defined as a point within space where two unique steady states coincide and subsequently disappear.[117] Mathematically, this bifurcation point exists when the number of real positive eigenvalues of the Jacobian matrix $\mathbf{J}$ of Eqs. (2.4) and (2.5), linearized in the neighborhood of steady states, changes. The existence of a saddle node is equivalent to the condition:

$$\det \mathbf{J}\big|_{\mathbf{x}^s} = 0 \tag{B1}$$

According to the first method of Liapunov, local stability of steady states is determined by the sign of the real part of eigenvalues of $\mathbf{J}$. A steady state is locally stable if and only if all of the eigenvalues are negative real numbers or complex numbers with negative real part. Since for the current two-dimensional case eigenvalues of the linearized system are given by roots of the quadratic characteristic equation,

$$\lambda^2 - \left(\operatorname{tr}\mathbf{J}\big|_{\mathbf{x}^s}\right)\lambda + \det \mathbf{J}\big|_{\mathbf{x}^s} = 0 \tag{B2}$$

the sufficient and necessary conditions for local asymptotic stability of steady states are readily derived as

$$\det \mathbf{J}\,|_{\mathbf{x}^s} > 0 \tag{B3}$$

$$\operatorname{tr} \mathbf{J}\,|_{\mathbf{x}^s} < 0 \tag{B4}$$

It can be concluded from Eqs. (B1) and (B3) that at the critical point where the determinant of the Jacobian matrix turns to zero, both the stability and the number of steady states will change. However, the sign change of the trace of the Jacobian matrix alone will not bring about the creation or destruction of the steady state but rather a change in stability, i.e. Hopf bifurcation. The presence of a Hopf bifurcation point induces limit cycles in the neighborhood of some steady states. A limit cycle is stable if all neighboring trajectories, starting from either the inside or outside of it, move towards the limit cycle, while the opposite is true for an unstable limit cycle. Once the onset of a limit cycle is established, its stability and direction can be determined via perturbation method detailed in Poore[99,100] and summarized for the current system below.

Eqs. (2.4) and (2.5) may be recast in a more compact form, as shown in Eqs. (B5) and (B6), where $\mathbf{x}$ is a vector of state variables and $\mathbf{p}$ is a vector of system parameters that are kept constant while the effect of bifurcation variable D is studied:

$$\frac{dx_1}{dt} = f_1(\mathbf{x}, \mathbf{p}, D) \tag{B5}$$

$$\frac{dx_2}{dt} = f_2(\mathbf{x}, \mathbf{p}, D) \tag{B6}$$

Given knowledge of a critical point $\mathbf{x}_0^S$ at which a limit cycle surrounding the steady state arises, i.e.

$$\operatorname{tr} \mathbf{J}\big|_{\mathbf{x}_0^S} = 0 \tag{B7}$$

$$\det \mathbf{J}\big|_{\mathbf{x}_0^S} > 0 \tag{B8}$$

and the bifurcation variable claims a value of D_0, variable transformation shown in Eq. (B9) is adopted in Poore[99,100] to facilitate perturbation analysis with μ as an independent small deviation from D_0 to determine the stability and direction of the limit cycle:

$$
\begin{aligned}
D &= D_0 + \xi \\
\xi &= \mu \xi(\mu) \\
T &= T_0\big(1 + \mu\eta(\mu)\big) \\
s &= \big(T_0/T\big)t \\
\mathbf{x} &= \mathbf{x}^S(\mu) + \mu\mathbf{y}(s,\mu)
\end{aligned}
\tag{B9}
$$

With the above variable transformation, Eqs. (B5) and (B6) become

$$\frac{d\mathbf{y}}{dt} = \mathbf{g}(\mathbf{y},\mathbf{p},\mu) \tag{B10}$$

The sign of the quantity $\int_0^{T^0} \nabla \cdot \mathbf{g}(\mathbf{y},\mathbf{p},\mu)\,ds$ determines the stability of the limit cycle according to Poincaré's criterion[117] with a negative value implying asymptotic stability and a positive one indicating instability. Expansion of the quantity in powers of μ gives

$$\int_0^{T^0} \nabla \cdot \mathbf{g}(\mathbf{y},\mathbf{p},\mu)\,ds = -\left[\operatorname{tr}\left(\frac{d\mathbf{J}}{dD}\right)_{D_0}\right]\xi'(0)\mu^2 + O\big(\mu^3\big) \tag{B11}$$

Therefore the stability of the limit cycle depends on the sign of the coefficient of the 2nd order term of μ in Eq. (B11) as follows:

$$\left[\mathrm{tr}\left(\frac{d\mathbf{J}}{dD} \right)_{D_0} \right] \xi'(0) \begin{cases} > 0, \text{asymptotic stability} \\ \\ \\ < 0, \text{instability} \end{cases} \tag{B12}$$

Since the sign of $\xi'(0)$ also determines the direction of the limit cycle as Eq. (B9) suggests, it is essential to obtain an expression for it as well as for $\mathrm{tr}\left(\frac{d\mathbf{J}}{dD} \right)_{D_0}$. Based upon implicit function theory and the chain rule for multivariable functions derivatives, the derivative of the Jacobian matrix with respect to the bifurcation variable evaluated at the critical point is calculated by Eq. (B13), where $\mathbf{IF}_1$ and $\mathbf{IF}_2$ are defined in Eqs. (B14) and (B15). The trace of Eq. (B13) is obtained by taking the real part of the product of the row eigenvector of the pure imaginary eigenvalue at the critical point, $\left(\frac{d\mathbf{J}}{dD} \right)_{D_0}$, and the corresponding column eigenvector as shown in Eq. (B16), where $\mathbf{u}$ and $\mathbf{v}$ satisfy Eq. (B17).

$$\left(\frac{d\mathbf{J}}{dD} \right)_{D_0} = \begin{bmatrix} \sum_{j=1}^{2} \frac{\partial^2 f_1}{\partial x_1 \partial x_j} \frac{-\det\left(\mathbf{IF}_j \right)}{\det \mathbf{J}} & \sum_{j=1}^{2} \frac{\partial^2 f_1}{\partial x_2 \partial x_j} \frac{-\det\left(\mathbf{IF}_j \right)}{\det \mathbf{J}} \\ \sum_{j=1}^{2} \frac{\partial^2 f_2}{\partial x_1 \partial x_j} \frac{-\det\left(\mathbf{IF}_j \right)}{\det \mathbf{J}} & \sum_{j=1}^{2} \frac{\partial^2 f_2}{\partial x_2 \partial x_j} \frac{-\det\left(\mathbf{IF}_j \right)}{\det \mathbf{J}} \end{bmatrix}_{D_0} + \begin{bmatrix} \frac{\partial^2 f_1}{\partial x_1 \partial D} & \frac{\partial^2 f_1}{\partial x_2 \partial D} \\ \frac{\partial^2 f_2}{\partial x_1 \partial D} & \frac{\partial^2 f_2}{\partial x_2 \partial D} \end{bmatrix}_{D_0} \tag{B13}$$

$$\mathbf{IF}_1 = \begin{bmatrix} \dfrac{\partial f_1}{\partial D} & \dfrac{\partial f_1}{\partial x_2} \\[2mm] \dfrac{\partial f_2}{\partial D} & \dfrac{\partial f_2}{\partial x_2} \end{bmatrix}_{D_0} \tag{B14}$$

$$\mathbf{IF}_2 = \begin{bmatrix} \dfrac{\partial f_1}{\partial x_1} & \dfrac{\partial f_1}{\partial D} \\[2mm] \dfrac{\partial f_2}{\partial x_1} & \dfrac{\partial f_2}{\partial D} \end{bmatrix}_{D_0} \tag{B15}$$

$$\mathrm{tr}\left(\frac{d\mathbf{J}}{dD}\right)_{D_0} = \mathrm{Re}\left[\mathbf{u}\left(\frac{d\mathbf{J}}{dD}\right)_{D_0}\mathbf{v}\right] \tag{B16}$$

$$\mathbf{u}\mathbf{J}_0 = i\sqrt{\det(\mathbf{J}_0)}$$
$$\mathbf{J}_0\mathbf{v} = i\sqrt{\det(\mathbf{J}_0)} \tag{B17}$$
$$\mathbf{u}\mathbf{v} = 1$$

It follows from Poore[99] that $\left[\mathrm{tr}\left(\frac{d\mathbf{J}}{dD}\right)_{D_0}\right]\xi'(0)$ is calculated as

$$\left[\mathrm{tr}\left(\frac{d\mathbf{J}}{dD}\right)_{D_0}\right]\xi'(0) = \mathrm{Re}\left\{\frac{1}{8}\left[-\mathbf{u}\,\mathbf{f}_{\mathbf{xxx}}\mathbf{v}\mathbf{v}\,\overline{\mathbf{v}} + 2\mathbf{u}\,\mathbf{f}_{\mathbf{xx}}\mathbf{v}\mathbf{J}_0^{-1}\mathbf{f}_{\mathbf{xx}}\mathbf{v}\,\overline{\mathbf{v}} + \mathbf{u}\,\mathbf{f}_{\mathbf{xx}}\mathbf{v}\left(\mathbf{J}_0 - 2i\sqrt{\det(\mathbf{J}_0)}\mathbf{I}\right)^{-1}\mathbf{f}_{\mathbf{xx}}\mathbf{v}\mathbf{v}\right]_{D_0}\right\} \tag{B18}$$

where

$$\mathbf{f}_{\mathbf{xxx}}\mathbf{v}\mathbf{v}\,\overline{\mathbf{v}} = \begin{bmatrix} \displaystyle\sum_{m=1}^{2}\sum_{k=1}^{2}\sum_{l=1}^{2}\frac{\partial^3 f_1}{\partial x_l \partial x_k \partial x_m} v_m v_k \overline{v_l} \\[3mm] \displaystyle\sum_{m=1}^{2}\sum_{k=1}^{2}\sum_{l=1}^{2}\frac{\partial^3 f_2}{\partial x_l \partial x_k \partial x_m} v_m v_k \overline{v_l} \end{bmatrix} \tag{B19}$$

Thus the sign of $\xi'(0)$ can be readily derived from a combination of Eqs. (B16) and (B19).

APPENDIX C

LIST OF MATLAB$^{\circledR}$ FILES

This appendix is intended to cover the MATLAB$^{\circledR}$ codes developed to generate results presented in Chapter II and III.

Table C1. List of MATLAB® codes for Chapter II

MATLAB® file name	Description	Results obtained	Sub-functions called
beta_delta_demarcation.m	Performs exhaustive node screening for pre-defined discretized (δ, β) plane. See Algorithm C following this table for pseudo codes.	• Figure 2.3 • Table 2.3	• MSDA.m • regionI.m • regionII.m • regionIII.m • regionIV.m • regionV.m • regionVI.m • orbit_direction_stability.m • Get_x1s_fsolve.m • jacobianest.m • r1_update.m • dAdD.m • hessian.m • gradest.m • hessdiag.m • derivest.m • FFFxxx1.m • FFFxxx2.m • global_variable_init.m • density_H2O2_aq.m

MATLAB® file name	Description	Results obtained	Sub-functions called
		• capacity_H2O2_aq.m	
MSDA.m	Obtains steady-state multiplicity and oscillation characteristics for a given set of (δ, β)	• Figure 2.1 • Figure 2.3 • Table 2.3	• jacobianest.m • r1_update.m
regionI.m	• Calculates steady-state conversion and temperature as a function of Da • Captures the lower and the upper Da corresponding to the desired conversion and temperature operation windows	• Figure 2.1 • Figure 2.3 • Figure 2.4 • Figure 2.5 • Figure 2.6 • Figure 2.7 • Figure 2.8 • Table 2.3	N/A
regionII.m	• Calculates steady-state conversion and temperature as a function of Da • Captures the critical Da corresponding to the two saddle nodes on the bifurcation diagram • Captures the lower and the upper	• Figure 2.1 • Figure 2.3 • Figure 2.4 • Figure 2.5 • Figure 2.6 • Figure 2.7 • Figure 2.8	Get_x1s_fsolve.m

MATLAB® file name	Description	Results obtained	Sub-functions called
	Da corresponding to the desired conversion and temperature operation windows	• Table 2.3	
regionIII.m regionIV.m regionV.m regionVI.m	• Calculates steady-state conversion and temperature as a function of *Da* • Captures the critical *Da* corresponding to the two saddle nodes on the bifurcation diagram • Captures the critical *Da* corresponding to onset and disappearance of limit cycles • Captures the lower and the upper *Da* corresponding to the desired conversion and temperature operation	• Figure 2.1 • Figure 2.3 • Figure 2.4 • Figure 2.5 • Figure 2.6 • Figure 2.7 • Figure 2.8 • Table 2.3	• orbit_direction_stability.m • Get_x1s_fsolve.m • jacobianest.m • dAdD.m • hessian.m • gradest.m • hessdiag.m • derivest.m • FFFxxx1.m • FFFxxx2.m

MATLAB® file name	Description	Results obtained	Sub-functions called
orbit_direction_stability.m	Captures the critical *Da* corresponding to onset and disappearance of limit cycles	• Figure 2.1 • Figure 2.3 • Table 2.3	• jacobianest.m • dAdD.m • hessian.m • gradest.m • hessdiag.m • derivest.m • FFFxxx1.m • FFFxxx2.m
jacobianest.m	Estimates the Jacobian matrix of a vector valued function of *n* variables	• Figure 2.1 • Figure 2.3 • Table 2.3	N/A
dAdD.m	Estimates Eq. (B13) for some *Da* and the corresponding steady state	• Figure 2.1 • Figure 2.3 • Table 2.3	• hessian.m • gradest.m • hessdiag.m • derivest.m
hessian.m	Estimates elements of the Hessian matrix	• Figure 2.1 • Figure 2.3 • Table 2.3	• gradest.m • hessdiag.m • derivest.m

MATLAB$^®$ file name	Description	Results obtained	Sub-functions called
gradest.m	Estimates the gradient vector of an analytical function of n variables	• Figure 2.1 • Figure 2.3 • Table 2.3	derivest.m
hessdiag.m	Estimates diagonal elements of the Hessian matrix	• Figure 2.1 • Figure 2.3 • Table 2.3	derivest.m
derivest.m	Estimates the nth derivative of a function at some point and provides an error estimate	• Figure 2.1 • Figure 2.3 • Table 2.3	N/A
FFFxxx1.m FFFxxx2.m	Estimates Eq. (B19) for some Da and the corresponding steady state	• Figure 2.1 • Figure 2.3 • Table 2.3	N/A
Get_x1s_fsolve.m	Solves corresponding steady state for a given set of (δ, β, Da)	N/A	N/A
r1_update.m	Calculates the overall reaction rate for given temperature and species concentrations according to Eq. (1.4)	N/A	N/A

MATLAB® file name	Description	Results obtained	Sub-functions called
Global_variable_init.m	Contains model constants presented in Table 1.5 and Table 2.1	N/A	N/A
phaseplot.m	Generates phase plots for a given set of (δ, β, Da) as well as multiple sets of initial conditions	• Figure 2.2 • Figure 2.9 • Table 2.3	N/A
Figure10.m	Generates conversion and temperature time profiles for a given set of (δ, β, Da) as well as multiple sets of initial conditions	Figure 2.10	N/A
worstcase_scenario.m	Plots time to 200 °C from target steady state for identified viable design area	Figure 2.11	main_read_mat.m draw_finer_demarcation.m worstcase_t200.m
main_read_mat.m	Reads viable design conditions (δ, β, Da, conversion, temperature, throughput) from spreadsheet data_pot.xlsx	Figure 2.11	N/A

MATLAB$^®$ file name	Description	Results obtained	Sub-functions called
draw_finer_demarcation.m	Plots demarcation of the selected (δ, β) plane	• Figure 2.3 • Figure 2.11	N/A
worstcase_t200.m	Simulates time to 200 ℃ from target steady state	Figure 2.11	N/A
Figure_uncertainties.m	Estimates the impact of parameter (heat of reaction and activation energy) uncertainties on viable design area	Figure 2.12	main_read_mat.m draw_finer_demarcation.m

Algorithm C. Pseudo codes for dividing (δ, β) plane in Chapter II based upon steady-state multiplicity and dynamic characteristics

---

Input: constant parameters α and T_c; grid search region $N: (\delta_L, \delta_U) \times (\beta_L, \beta_U)$;

Damköhler number range (Da_L, Da_U);

Output: region matrix **RM**, extinction structures **EX**, and ignition structures **IGN**

Initialize region matrix **RM**, extinction structures **EX**, and ignition structures **IGN**;

for each node $n_{ij}(\delta_i, \beta_j) \in N$, **do**

    Get multiplicity and oscillation characteristics;

    if unique steady state for all Da #s **then**

        if no bifurcation to limit cycles for some Da #s **then**

            Label $\mathbf{RM}_{ij}$ as region I;

        else if bifurcation to limit cycles occurs at two critical points s_1 and $s_2 (s_1 < s_2)$ **then**

            Get the characteristics of limit cycles at s_1;

            Save s_2 information to the $i \times j^{th}$ extinction structure $\mathbf{IGN}_{ij}$;

            if bifurcation to limit cycles at s_1 is to the left of s_1 **then**

                Label $\mathbf{RM}_{ij}$ as region Va;

                Calculate the critical point s_1^* where oscillation ceases;

                Save s_1^* information to the $i \times j^{th}$ extinction structure $\mathbf{EX}_{ij}$;

            else if bifurcation to limit cycles at s_1 is to the right of s_1 **then**

                Label $\mathbf{RM}_{ij}$ as region Vb;

                Save s_1 information to the $i \times j^{th}$ extinction structure $\mathbf{EX}_{ij}$;

            else

                New type of bifurcation diagram discovered;

            end if {complete determining bifurcation to limit cycles}

else

    New type of bifurcation diagram discovered;

end if {the case of unique steady state is completed}

else if S shape steady-state multiplicity with m_1 and m_2 $(m_1 < m_2)$ as saddle nodes **then**

    if no bifurcation to limit cycles for some Da #s **then**

        Label $\mathbf{RM}_{ij}$ as region II;

        Calculate the extinction point m_1^* and ignition point m_2^*;

        Save m_1^* information to the $i \times j^{th}$ extinction structure $\mathbf{EX}_{ij}$;

        Save m_2^* information to the $i \times j^{th}$ extinction structure $\mathbf{IGN}_{ij}$;

    else if bifurcation to limit cycles occurs at two critical points s_1 and $s_2(s_1 < s_2)$ **then**

        Calculate the extinction point m_1^*;

        Save m_1^* information to the $i \times j^{th}$ extinction structure $\mathbf{EX}_{ij}$;

        Save s_2 information to the $i \times j^{th}$ extinction structure $\mathbf{IGN}_{ij}$;

        if $s_1 > m_2$ **then**

            if $Da(s_1) > Da(m_1)$ **then**

                Label $\mathbf{RM}_{ij}$ as region VIa;

            else if $Da(s_2) > Da(m_1)$ **then**

                Label $\mathbf{RM}_{ij}$ as region VIb;

            else

                Label $\mathbf{RM}_{ij}$ as region VIc;

            end if

        else if $s_1 < m_1$ and $s_2 > m_2$ **then**

            if $Da(s_2) > Da(m_1)$ **then**

                if $Da(s_1) > Da(m_2)$ **then**

                    Label $\mathbf{RM}_{ij}$ as region IVa;

else

> Label $\mathbf{RM}_{ij}$ as region IVb;

else if

else

> **if** $Da(s_1) > Da(s_2)$ **then**

>> Label $\mathbf{RM}_{ij}$ as region IVc;

> **else**

>> Label $\mathbf{RM}_{ij}$ as region IVd;

> **end if**

end if

else

> New type of bifurcation diagram discovered;

end if {complete determining bifurcation to limit cycles}

else if bifurcation to limit cycles occurs at one critical points s_2
$(m_2 < s_2)$ **then**

> Calculate the extinction point m_1^*;

> Save m_1^* information to the $i \times j^{th}$ extinction structure $\mathbf{EX}_{ij}$;

> **if** $Da(s_2) > Da(m_1)$ **then**

>> Label $\mathbf{RM}_{ij}$ as region IIIb;

>> Save s_2 information to the $i \times j^{th}$ extinction structure $\mathbf{IGN}_{ij}$;

> **else**

>> Get the characteristics of limit cycles at s_2;

>> Calculate the extinction point m_2^*;

>> Save m_2^* information to the $i \times j^{th}$ extinction structure $\mathbf{IGN}_{ij}$;

>> **if** bifurcation to limit cycles at s_2 is to the left of s_2 **then**

129

                    Label $\mathbf{RM}_{ij}$ as region IIIc;

                else if bifurcation to limit cycles at s_2 is to the right of s_2

                then

                    Label $\mathbf{RM}_{ij}$ as region IIIa;

                else

                    New type of bifurcation diagram discovered;

                end if

            end if {complete determining bifurcation to limit cycles}

        else

            New type of bifurcation diagram discovered;

        end if {the case of steady-state multiplicity is completed}

    end if

end for {the grid search for all nodes within N is completed}

<div align="center">**Table C2.** List of MATLAB$^®$ codes for Chapter III</div>

MATLAB$^®$ file name	Description	Results obtained	Sub-functions called
sweepDa_forH.m plot_sweepDa_forH_Da1E5.m	Sweeps Da (up to 10^5) to obtain conversion and peroxide exit molar flow rate profiles at specific H values	Figure 3.2	• global_variable_init_membrane.m • ODE_membrane_1D_update.m • r1_update.m
sweepH.m plot_H_Da095_Fpe.m plot_H_Da095_Fpe_res_deltaP.m	Sweeps H to obtain the critical Da for 95% conversion and the corresponding % peroxide exit molar flow rate	Figure 3.3	• global_variable_init_membrane.m • ODE_membrane_1D_update.m • r1_update.m
hexagon.m	• Estimates bundle dimensions as a function of center-to-center distance between adjacent tubes • Evaluates feasibility of maintaining isothermal operation by comparing heat generation rate with heat removal rate	• Figure 3.4 • Figure 3.5 • Figure 3.6 • Table 3.3 • Table 3.4	• global_variable_init_membrane.m • ODE_membrane_1D_update.m • hexagon_bundle_calculation.m • r1_update.m

MATLAB® file name	Description	Results obtained	Sub-functions called
hexagon_bundle_calculation.m	Estimates heat generation by integrating reaction heat down reactor length	• Figure 3.4 • Figure 3.5 • Table 3.3 • Table 3.4	r1_update.m
hexagon_tube_aspectratio.m	Estimates single unit aspect ratio as a function of center-to-center distance between adjacent tubes	• Figure 3.4 • Table 3.3 • Table 3.4	global_variable_init_membrane.m
r1_update.m	Calculates the overall reaction rate for given temperature and species concentrations according to Eq. (1.4)	N/A	N/A
global_variable_init_membrane.m	Contains model constants presented in Table 1.5, 3.1, and 3.2	N/A	N/A
ODE_membrane_1D_update.m	Contains dimensionless model equations presented in Eqs. (3.10) – (3.13)	N/A	N/A

APPENDIX D

CONSTRUCTION OF A PILOT-SCALE CSTR SYSTEM

D.1   Purpose

Theoretical study of chemical reactor stability generally embraces the subjects of multiplicity, stability, and occurrence of self-sustained oscillations. In Chapter II, we reported *in silico* predictions of steady-state multiplicity and oscillation phenomena for a jacketed continuous stirred tank reactor (CSTR) accommodating the homogenous catalytic exothermic N-oxidation of alkylpyridines. The present study aims to provide experimental validation of the theoretically predicted behaviors derived from first-principles modeling and system analysis.

Specifically, a pilot-scale stainless steel CSTR will be constructed with external copper cooling/heating coil in contact with the reactor wall. The two liquid-phase reactants will be fed to the reactor by pressure difference between the reservoir tank and the reactor. A tube-in-tube feed design will be implemented to prevent premixing of the two reactants and backpressure regulators will be employed to maintain the driving force. Inlet flow rates of the reactants will be manipulated by two rotameters in the feed lines. By varying the feed flow rates, reactor state, which is primarily represented by temperature and measured by a thermocouple assembly comprising three K-type probes located at different positions within the reactor, is expected to be shifted and will be quantitatively compared with theoretical predictions for corresponding scenarios. Mixing

will be provided by a polytetrafluoroethylene (PTFE) magnetic bar driven by a magnetic plate and homogeneity will be checked according to variation among readings from the three thermocouples. Composition of the reaction mixture will be continuously measured by FTIR. For safety purpose, several check valves will be installed to prevent back flow and relief valves rupture of the tanks.

D.2   Description of the Setup

D.2.1. Overview

The reaction system is shown in Figure D1. The reactor (Figure D2) is cylindrical in shape and is constructed of type 316 stainless steel (¼" thickness). The bottom and the top plates are welded to the body, and sealing of the top lid is provided by a PTFE O-ring in addition to six bolts screwed through the lid and the top plate. The two ¼" MNPT holes on the reactor wall are intended to install a piece of semi-clear rigid PTFE tubing for level indication. The five holes on the top lid are designed for reactant inlet (¼" MNPT), product outlet (¼" MNPT), thermocouple feedthrough (½" MNPT), pressure control (¼" MNPT), and FTIR probe (½" MNPT) respectively. A ⅜" copper coil is wrapped around the reactor for flushing heating/cooling fluid which is delivered by a circulator. Mixing is accomplished by a PTFE magnetic bar.

The two feed streams come from two nitrogen-pressurized tanks and premixing is prevented by using a tube-in-tube configuration (inner tubing: 1/16" for hydrogen

134

peroxide solution; outer tubing: ¼" for alkylpyridines). Flow rates are controlled by

rotameter, before which check valves are installed to prevent back flow.

Details of the major apparatuses in Figure D1 are given as follows.
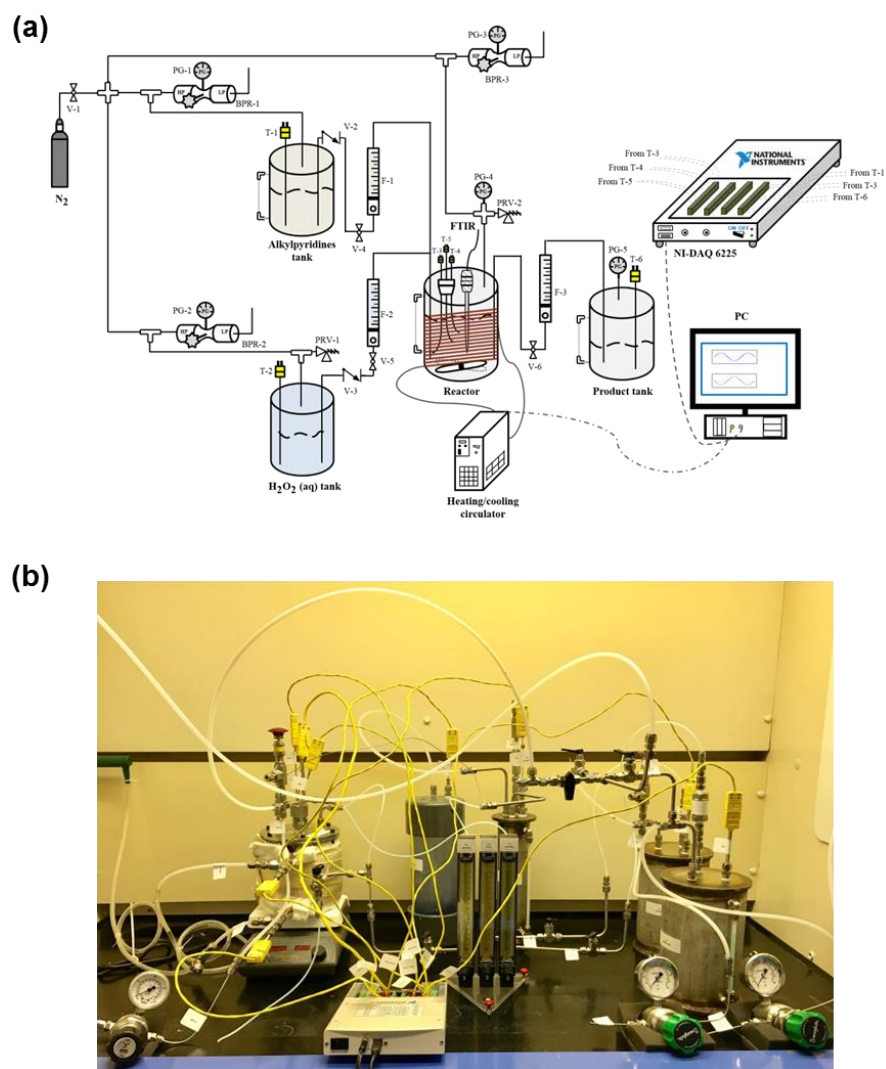
Figure D1. (a) Schematic diagram and (b) actual picture of the CSTR system
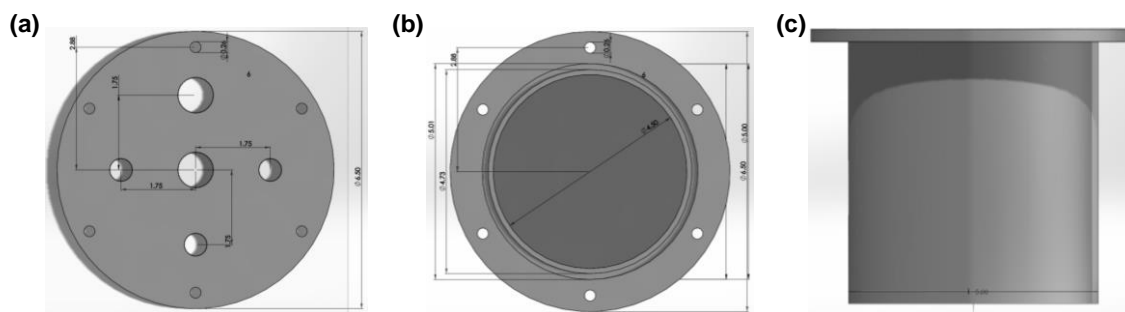
Figure D2. Schematic illustration of the CSTR (a) Top lid (b) Top view without the top lid (c) Front view

D.2.1.1.   Backpressure regulator

Table D1. List of backpressure regulators used in the CSTR system shown in Figure D1

	BPR-1	BPR-2	BPR-3
Manufacturer	Swagelok	Swagelok	Parker Veriflo
Model	KBP1F0D4A5A60000	KBP1F0D4A5A20000	ABP1ST33BP24
Materials of construction	• Body: 316 SS • Seal: Fluorocarbon FKM PCTFE	• Body: 316 SS • Seal: Fluorocarbon FKM PCTFE	• Body: 316 SS • Seal: PTFE
Pressure control range	0 – 100 psig	0 – 100 psig	3 – 100 psig
Flow coefficient	0.20	0.20	0.3
Max. inlet pressure	100 psig	100 psig	100 psig
Max. operating temperature	176 °F (80 °C)	176 °F (80 °C)	400 °F (204 °C)

Table D2. List of pressure relief valves used in the CSTR system shown in Figure D1

	PRV-1 and PRV-2
Manufacturer	Swagelok
Model	SS-RL3S4-EP
Materials of construction	• Body: 316 SS • Seal: Ethylene Propylene (EP)
Set pressure range	10 – 225 psig
Working pressure at 70 °F (20 °C)	300 psig

Table D3. List of check valves used in the CSTR system shown in Figure D1

	V-2	V-3
Manufacturer	McMaster Carr	Swagelok
Model	47885K71	SS-4C-1
Materials of construction	• Body: 316 SS • Seal: PTFE	• Body: 316 SS • Seal: FKM
Max. pressure	• 400 psi @ 70 °F for water & air • 125 psi @ 350 °F for steam	3000 psig @ 100 °F
Cracking pressure	0.5 psi	1 psi
Temperature range	-4 °F (-20 °C) to +350 °F (176 °C)	375 °F @ 2185 psig

Table D4. List of toggle valves used in the CSTR system shown in Figure D1

	V-4	V-5 and V-6
Manufacturer	Swagelok	Swagelok
Model	SS-1GS4-KZ	SS-1GS4
Materials of construction	• Body: 316 SS • Seal: Kalrez	• Body: 316 SS • Seal: FKM
Max. pressure	200 psig	200 psig
Cracking pressure	0.5 psi	0.5 psi
Temperature range	-20 °F (-28 °C) to +200 °F (93 °C)	-20 °F (-28 °C) to +200 °F (93 °C)

D.2.1.3.   Rotameter

Table D5. List of rotameters in the CSTR system shown in Figure D1

	F-1, F-2, and F-3
Manufacturer	Cole-Parmer
Model	EA-03217-72
Materials of construction	• Body: Borosilicate Glass • Seal: PTFE • Float: Sapphire
Flow rate range	2.6 mL/min – 26.L ml/min (water)
Max. pressure	100 psi
Max. temperature	150 °F (65 °C)

Table D6. List of thermocouples in the CSTR system shown in Figure D1

	T-1 and T-2	T-3, T-4, and T-5	T-6
Manufacturer	OMEGA	OMEGA	OMEGA
Model	KQXL-14G-12	KQXL-18G-12	KQXL-16G-18
Materials of construction for sheath	Ni-Cr Based Super OMEGACLAD®	Ni-Cr Based Super OMEGACLAD®	Ni-Cr Based Super OMEGACLAD®
Response time	2.25 sec	0.55 sec	0.3 sec
Max. operating temperature	• 1832 °F (1000 °C) for 2 months • 1500 °F (815 °C) for 3 years	• 1832 °F (1000 °C) for 2 months • 1500 °F (815 °C) for 3 years	• 1832 °F (1000 °C) for 2 months • 1500 °F (815 °C) for 3 years

Table D7. Thermocouple feedthrough used in the CSTR system shown in Figure D1

Manufacturer	OMEGA
Model	MFT-18-3
Materials of construction	• Body and cap: 316 SS • Seal: 316 SS
# of probes allowed	3

D.2.1.5.   FTIR (to be installed)

ReactIR 15, detailed in Table D8, is connected to a PC through a USB cable, which collects, visualizes, and analyzes real time infrared data by running the iC IR 4.3 software. Note that the detector must be kept cool with liquid nitrogen in order to be functional.

Table D8. FTIR used in the CSTR system shown in Figure D1

Manufacturer	Mettler Toledo
Model	ReactIR 15
Detector	Mercury Cadmium Telluride
Resolution	4 /cm max.
Optical window	2500 – 650 /cm max.
Purge	No purge required
Max. probe pressure	69 barg
Max. pobe temperature	356 °F (180 °C)
Probe pH range	1 – 9

D.2.1.6.   Heating/cooling circulator (to be installed)

Table D9. Heating/cooling circulator used in the CSTR system shown in Figure D1

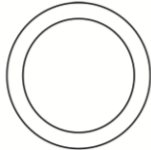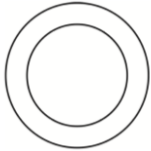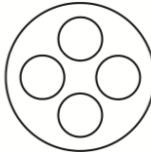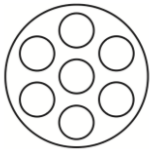|	
Manufacturer	JULABO
Model	Presto LH45
Operating temperature	5 to 250 °C
Power requirement	230 V, 3 phases
Heating capacity	1800 W
Cooling capacity	1200 W @ 20 °C
Flow rate	24 LPM

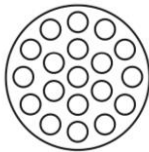# APPENDIX E

INFORMATION OF POROUS CERAMIC MEMBRANE TUBES FROM INOPOR[®]
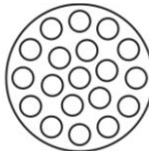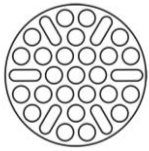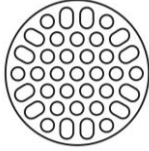
GMBH
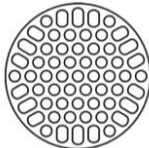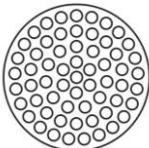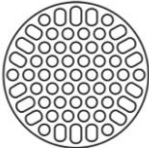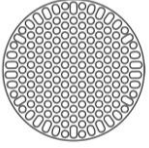
Table E1. Available membrane materials and pore sizes

Membrane material	Pore diameter d^m (nm)	Porosity ε^m (%)
α-Al$_2$O$_3$	800	40 – 55
	600	40 – 55
	400	40 – 55
	200	40 – 55
	100	40 – 55
	70	40 – 55
TiO$_2$	800	40 – 55
	400	40 – 55
	250	40 – 55
	200	40 – 55
	100	40 – 55
ZrO$_2$	110	40 – 55

Table E2. Available membrane tube geometries for each material type presented in Table E1

Geometry	Tube outer diameter d_o (mm)	Channel diameter d_i (mm)	Number of channels	Specific membrane area (m^2/m)
	10	7.0	1	0.024
	20.3	15.5	1	0.049
	20.6	6.1	4	0.077
	25.0	6.0	7	0.132

Geometry	Tube outer diameter d_o (mm)	Channel diameter d_i (mm)	Number of channels	Specific membrane area (m^2/m)
	25.0	3.5	19	0.209
	41.4	6.0	19	0.358
	25.0	3.0	31	0.315
	41.0	3.8	37	0.490

Geometry	Tube outer diameter d_o (mm)	Channel diameter d_i (mm)	Number of channels	Specific membrane area (m^2/m)
	26.4	2.0	61	0.426
	25.0	2.0	61	0.383
	41.0	3.4	61	0.722
	41.0	2.0	163	1.098

APPENDIX F

NOMENCLATURE

Acronyms

ARC	Accelerating Rate Calorimeter
API	Active Pharmaceutical Ingredient
CAS	Chemical Abstracts Service
CBER	Center for Biologics Evaluation and Research
CFD	Computational Fluid Dynamics
CGMP	Current Good Manufacturing Practice
CHETAH	Chemical Thermodynamics and Energy Release Evaluation
CRW	Chemical Reactivity Worksheet
CSB	U.S. Chemical Safety and Hazard Investigation Board
DoE	Design of Experiment
DSC	Differential Scanning Calorimeter
FDA	U.S. Food and Drug Administration
FMEA	Failure Mode Effects Analysis
FTIR	Fourier-Transform Infrared Spectroscopy
HAZOP	Hazard and Operability Study
LOPA	Layer of Protection Analysis

MSDS	Material Safety Data Sheet
NFPA	National Fire Protection Association
ORA	Office of Regulatory Affairs
PAT	Process Analytical Technology
PEEK	Polyether ether ketone
PFA	Perfluoroalkoxy alkane
PTFE	Polytetrafluoroethylene
RSST	Reactive System Screening Tool
VSP	Vent Sizing Package

Letters

a	Heat transfer area, m^2
A	Alkylpyridine
A_c	Cross-sectional area, m^2
B	Hydrogen peroxide
BZ	Hydrogen peroxide-catalyst intermediate
c	Concentration, $mol \cdot m^{-3}$
$\overline{C_p}$	Averaged specific heat capacity, $J \cdot g^{-1} \cdot K^{-1}$ (in Chapter II) or $J \cdot kg^{-1} \cdot K^{-1}$ (in Chapter III)
d	Membrane diameter, m
D	Bundle diameter, m
Da	Damköhler number, dimensionless

147

F	Molar flow rate, $\text{mol} \cdot \text{s}^{-1}$
$\overline{F_i^S}$	Dimensionless molar flow rate, $\frac{F_i^S}{F_{a,0}^S}$ $(i : p, a)$
h	Heat transfer coefficient, $\text{W} \cdot \text{m}^{-2} \cdot \text{K}^{-1}$
H	Permeation number, defined in Eq. (3.17), dimensionless
ΔH_{rxn}	Heat of reaction for N-oxdiation of alkylpyridines, $\text{kJ} \cdot \text{mol}^{-1}$
$\bar{k}$	Averaged heat conductivity, $\text{W} \cdot \text{m}^{-1} \cdot \text{K}^{-1}$
k_{1a}	Rate coefficient of Eq. (1.1), $\text{L} \cdot \text{mol}^{-1} \cdot \text{s}^{-1}$
k_{1b}	Rate coefficient of Eq. (1.2), $\text{L} \cdot \text{mol}^{-1} \cdot \text{s}^{-1}$
K_b	Chemical equilibrium coefficient of Eq. (1.3), $\text{L} \cdot \text{mol}^{-1}$
l	Center-to-center distance between adjacent tubes, m
L	Reactor length, m
$\overline{mC_{pm}}$	Thermal capacity of solid equipment parts (reactor wall, bottom plate, stirrer and impeller), $\text{J} \cdot \text{K}^{-1}$
MW	Molecular weight, $\text{g} \cdot \text{mol}^{-1}$
N	Alkylpyridine N-oxide
N_{Nu}	Nusselt number, defined in Eq. (3.26), dimensionless
N_{Pe_r}	Radial Peclet number, defined in Eq. (3.27), dimensionless
N_{Pr}	Prandtl number, defined in Eq. (3.26), dimensionless
N_{Re}	Reynolds number, defined in Eq. (3.26), dimensionless
P	Pressure, Pa

q	Overall volumetric flow rate, $L \cdot s^{-1}$
$\dot{q}$	Heat flux, $W \cdot m^{-2}$
r	Reaction rate, $mol \cdot L^{-1} \cdot s^{-1}$
R	Gas constant, $J \cdot mol^{-1} \cdot K^{-1}$
$t^{'}$	Time, s
T	Temperature, K
U	Heat transfer coefficient, $W \cdot m^{-2} \cdot K^{-1}$
v	Velocity, $m \cdot s^{-1}$
$\overline{v^s}$	Dimensionless velocity, $\frac{v^s}{v_0^s}$
V	Reaction volume, L
W	Water
x	Conversion of alkylpyridine, dimensionless
Z	Catalyst ($H_3PW_{12}O_{40}$)
$[\ ]$	Concentrations of species, $mol \cdot L^{-1}$
Greek symbols in Chapter II	
α	Ratio of feed concentration, $\frac{[B]_f}{[A]_f}$, dimensionless
β	Adiabatic temperature rise, $\frac{(-\Delta H_{ox})[A]_f}{\bar{\rho}\bar{C_p}T_f}\gamma$, dimensionless
δ	Cooling number, $\frac{Ua}{\bar{\rho}\bar{C_p}q}$, dimensionless

ε	Thermal capacity ratio of solid equipment parts to reaction mixture, $\dfrac{\overline{m C_{pm}}}{\overline{\rho C_p} V}$, dimensionless
γ	Activation energy, $\dfrac{E_{1b}}{R T_f}$, dimensionless
ω	Weight fraction of H_2O_2 (aq)

Greek symbols in Chapter III

α	Surface area, m^2/m^3
δ	Inlet concentration ratio of catalyst to alkylpyridine, $\dfrac{c_{z,0}^s}{c_{a,0}^s} \approx \dfrac{c_z^s}{c_{a,0}^s}$
ε	Porosity, dimensionless
ζ	Axial coordinate, m
$\bar{\zeta}$	Dimensionless axial coordinate, $\dfrac{\zeta}{L}$
θ	Inlet concentration ratio of hydrogen peroxide to alkylpyridine, $\dfrac{c_{p,0}^t}{c_{a,0}^s}$
κ	Permeability, m^2
λ	Thickness, m
$\bar{\mu}$	Averaged viscosity, $\overline{\mu^t} = \mu_{p,0}\omega_{p,0} + \mu_{w,0}(1 - \omega_{p,0})$, $Pa \cdot s$
$\bar{\rho}$	Averaged density, $kg \cdot m^{-3}$
τ	Tortuosity, dimensionless
φ	Inlet concentration ratio of water to hydrogen peroxide, $\dfrac{c_{w,0}^t}{c_{p,0}^t}$
ω	Weight fraction of hydrogen peroxide aqueous solution

Subscripts

a	Alkylpyridine
c	Cooling
f	Feed
i	Inner
iso	Isothermal
o	Outer
ox	N-oxidation
p	Hydrogen peroxide
w	Water
0	Inlet condition

Superscripts in Chapter II

s	Steady-state

Superscripts in Chapter III

m	Membrane
s	Shell side (annulus)
t	Tube side